Tomographic measurements and analyses on solitary oscillations and findings of nonlinear effects of background asymmetry in a cylindrical plasma

小林, 大輝

出版情報：Kyushu University, 2024, 博士（工学）, 課程博士
バージョン：
権利関係：

Tomographic measurements and analyses on solitary oscillations and findings of nonlinear effects of background asymmetry in a cylindrical plasma

Taiki Kobayashi

Interdisciplinary Graduate School of Engineering Sciences,
Kyushu University

2024

Contents

Chapter 1
Introduction

1.1 Nuclear Fusion Reactor

In recent years, the Sustainable Development Goals (SDGs) proposed at the United Nations Summit have become a global goal. The SDGs include 17 targets for poverty, education, economy, environment and more. Especially, energy is one of the targets that must be achieved in light of the recent acceleration of population growth. This is because the United Nations has reported that the world population will exceed 8 billion by 2023. If population growth accelerates at this pace, it is expected to surpass 10 billion by around 2070, as shown in Fig. 1.1 [1]. Such an enormous increase in population should be accompanied by an increase in energy demand. To increase energy production, thermal power generation is being actively used, but there are concerns about global warming due to the generation of greenhouse gases. Nuclear power generation is also being used as a method of power generation that does not generate greenhouse gases, but since the Great East Japan Earthquake in March 2011, there have been concerns about safety, including the release of radioactive materials. In addition, there is a limit to the amount of extractable energy resources needed for thermal and nuclear power generation, and there is concern that the cost of power generation will increase in the future. Other renewable energy sources, such as hydro, wind, and solar power, are also being used to generate electricity, but it is difficult to spread them around the world in terms of generating efficiency, cost, and location. Thus, power generation methods with high generation

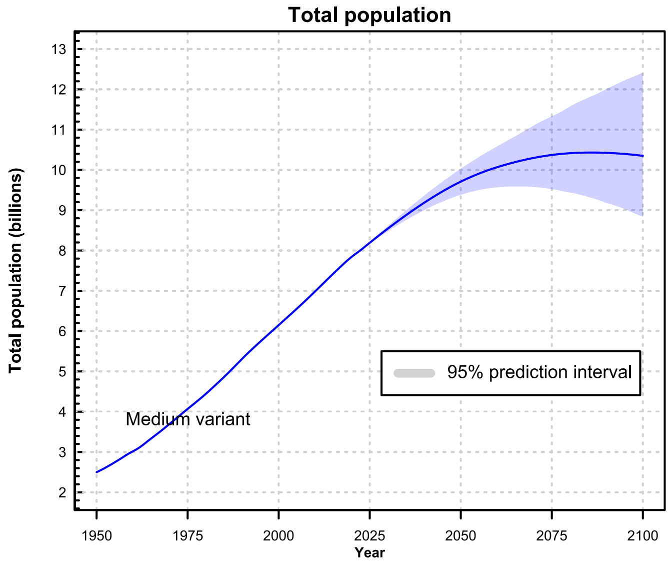

Fig. 1.1. Predicted value of world population growth. The masking region is the interval of the 95% prediction [1].

efficiency, inexhaustible energy resources, and excellent safety will be needed to support future energy problems.

Thermonuclear fusion reactors have attracted attention as an excellent power generation system because of their high power generation efficiency, inexhaustible energy resources, and high environmental adaptability. There are three main types of fusion reactions: the Deuterium-Deuterium (D-D) reaction, the Deuterium-Tritium (D-T) reaction, and the Deuterium-Helium-3 (D-He^3) reaction as followings.

$$ {}^{2}_{1}\mathrm{H}+{}^{2}_{1}\mathrm{H} \rightarrow {}^{3}_{2}\mathrm{He}+{}^{1}_{0}n+3.27\mathrm{MeV}, $$
$$ {}^{2}_{1}\mathrm{H}+{}^{3}_{1}\mathrm{H} \rightarrow {}^{4}_{2}\mathrm{He}+{}^{1}_{0}n+17.59\mathrm{MeV}, $$
$$ {}^{2}_{1}\mathrm{H}+{}^{3}_{2}\mathrm{He} \rightarrow {}^{4}_{2}\mathrm{He}+{}^{1}_{1}\mathrm{H}+18.3\mathrm{MeV}. \tag{1.1} $$

Deuterium, which is required for each of these reactions, can be obtained from seawater, which is a practically inexhaustible energy resource. Currently, the D-T reaction is considered advantageous because it requires low energy and has a large reaction cross section, but the tritium required for the reaction cannot be obtained in nature. Hence, a

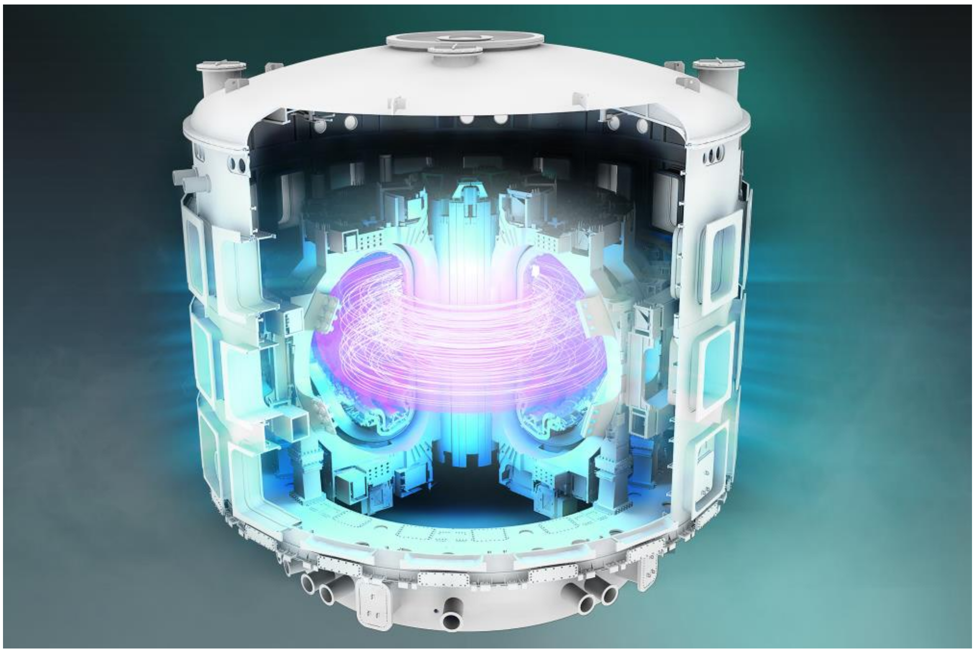

Fig. 1.2. The schematic of ITER [2].

method has been devised to breed tritium by reacting lithium with neutrons produced in the D-T reaction as shown below.

$$
\begin{aligned}
{}^{6}_{3}\mathrm{Li}+{}^{1}_{0}n(\mathrm{slow}) &\rightarrow {}^{4}_{2}\mathrm{He}+{}^{3}_{1}\mathrm{H}+4.8\mathrm{MeV}, \\
{}^{7}_{3}\mathrm{Li}+{}^{1}_{0}n(\mathrm{fast}) &\rightarrow {}^{4}_{2}\mathrm{He}+{}^{3}_{1}\mathrm{H}+{}^{1}_{0}n(\mathrm{slow})\text{-}2.82\mathrm{MeV}.
\end{aligned} \tag{1.2}
$$

Where, ${}^{1}_{0}n(\mathrm{slow})$ and ${}^{1}_{0}n(\mathrm{fast})$ represent low energy thermal neutrons and high energy fast neutrons. In addition, to obtain energy from fusion reactions, it is necessary to increase the reaction rate by confining high-temperature, high-density plasma for a long time. The magnetic field confinement method, which confines the plasma by utilizing the property of charged particles to move around magnetic field lines, has been studied since the early 1950s. Currently, two types of magnetic field confinement methods, tokamak and helical, are being actively studied. In particular, the tokamak method has succeeded in producing a first plasma in JT-60SA in October 2023, and is starting operation to obtain the data required for a fusion DEMO reactor. In addition, the construction of ITER (International Thermonuclear Experimental Reactor: Fig. 1.2 [2]) is underway in France to demonstrate fusion energy. To achieve economic viability of a fusion reactor, the fusion energy gain factor $Q = P_{\mathrm{fusion}}/P_{\mathrm{in}}$, which is the ratio of fusion power to input power, must be high. Currently, the critical plasma condition Q=1 has been achieved in the Joint European Torus (JET) and JT-60 [3,4], and ITER aims to reach Q=10, which is close to the self-ignition condition. To generate a plasma close to the self-ignition condition, the plasma must be heated to maintain a high temperature. This requires auxiliary heating of the plasma by high external heating power such as neutral beam injection (NBI) [5,6], ion cyclotron resonance heating (ICRH) [7], and electron cyclotron resonance heating (ECRH) [8] and so on. However, simply increasing the heating power is not the only way to obtain a high-performance plasma. A long-standing problem in plasma fusion is a phenomenon called power degradation, in which the plasma confinement performance deteriorates with increasing heating power, and the detailed physical mechanism has not yet been clarified. This is expected to drive turbulence by steepening the temperature and density gradients during auxiliary heating of the plasma, and the resulting transport would degrade confinement performance. Therefore, it is necessary to simultaneously investigate changes in plasma structure and transport caused by auxiliary heating in order to realize an economical fusion reactor.

1.2 Structure Formation of Plasma Turbulence

Various instabilities exist in magnetic confined plasmas. This is due to the inevitable existence of steep pressure gradients. The pressure gradient excites microscopic instabilities called drift waves, which develop into turbulence of various scales through nonlinear processes. Therefore, fluctuations and structures of disparate scales (micro-, meso- and macro-) coexist in a magnetic confinement plasma, and these fluctuations and structures further interact to excite instabilities and suppress turbulence, thereby sustaining the structure of the plasma [9-18]. The zonal flow is a typical example of the excitation of various instabilities and structures through the nonlinear process of the drift wave. The zonal flow is a universal phenomenon in nature as well as in magnetic confinement plasmas, since a structure similar to zonal flows is observed in planetary atmospheres with atmospheric structures in which the east-west wind speed is dominant compared to the north-south wind speed (such as the Great Red Spot in Jupiter's atmosphere [19]). In a magnetic confinement plasma, the zonal flow is a structure that is uniform in the toroidal and poloidal directions ($n = m = 0$, n: toroidal number, m: poloidal number), has finite wavenumber in the radial direction, and alternately reverses positive and negative flows in the radial direction. It is known that such flows effectively break up large vortices and waves in the plasma, thereby suppressing turbulence, and theory and simulation have shown that such flows have a significant impact on improving the confinement properties of fusion plasmas [20-22].

In the Compact Helical System [23], zonal flows were identified by measuring the density fluctuations of the plasma at different toroidal positions using heavy ion beam probe (HIBP) [24]. As shown in Fig. 1.3(a, b), the time evolution of the electric field in the same magnetic surfaces are in the same phase, but the time evolution of the electric

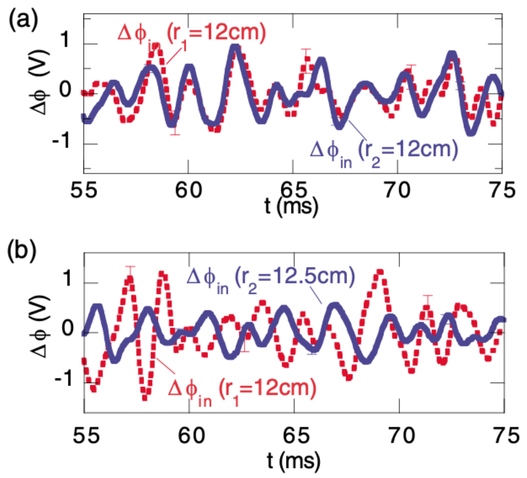

Fig. 1.3. Time evolution of zonal flows in the same magnetic flux surface at different toroidal positions (a) and in different magnetic flux surface at different toroidal positions (b) [24].

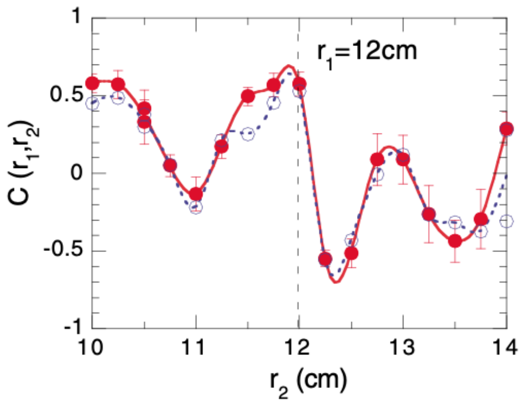

Fig. 1.4. The radial structure of zonal flow [24].

field in different magnetic surfaces are out of phase. In addition, as shown in Fig. 1.4, it is confirmed that the finite wavenumber is approximately 1 cm in the radial direction. It is observed that with and without the transport barrier, there is a clear difference in the amplitude of the density fluctuation and zonal flow, which indicates that turbulence is suppressed by the formation of the zonal flow.

On the other hand, it was demonstrated that the process by which drift waves excite zonal flows in a linear device due to parametric modulational instability [25]. Figure 1.5 shows the results of measuring the poloidal and radial wavenumbers of the drift wave and simultaneously the potential fluctuations of the zonal flow in the coexistence of the drift

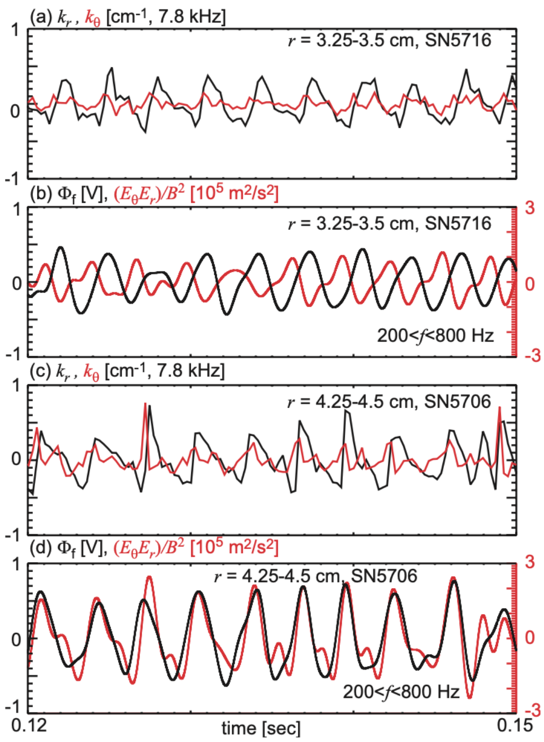

Fig. 1.5. Time evolution of wavenumbers (k_r and k_θ), zonal flows, and Reynolds stresses at different radial positions. (a, b) at radial position r = 3.25 - 3.5 cm and (c, d) at radial position r = 4.25 - 4.5 cm [25].

wave and the zonal flow at Large Mirror Device. It was observed that the radial wavenumber of the drift wave fluctuates significantly with the potential fluctuation of the zonal flow, confirming that the wavefront is bent by the zonal flow. Comparing Fig. 1.5(b, d), it was observed that the phase difference between the Reynolds stress of the drift wave and the potential fluctuation of the zonal flow was different in the radial position. Since these radial variations become torques that drive the rotation in the poloidal direction, these results indicate that the turbulent stresses accelerate the original rotation of the zonal flow. In a magnetic confinement plasma, microscopic instabilities can excite meso- and macroscale structures through nonlinear processes, thereby determining the plasma structure and affecting the confinement properties. Therefore, an advance in our understanding of the plasma turbulence structure formation process can make a significant contribution to improving the confinement of high-performance plasmas.

1.3 Symmetry Breaking of Plasma Turbulence

Symmetry is one of the fundamental concepts to constrain the physical systems through conservation of physical quantity such as angular momentum, momentum, and energy. The concept of symmetry is used in a variety of fields. For example, Galilean transformation symmetry in three-dimensional space in Newtonian mechanics, Lorentz transformation symmetry in the space-time continuum in special relativity, and gauge symmetry of gauge fields in quantum mechanics. As shown above, the concept of symmetry has played an important role in various fields in physical systems.

Symmetry is an important concept to consider in plasma turbulence. In particular, theoretical and experimental studies on "symmetry breaking" have been conducted in recent years with the development of plasma turbulence physics and measurement systems [26-29]. In research of magnetic confinement plasmas, it is observed in several experiments that symmetry breaking of turbulence field in response to inhomogeneous confinement field [30-36]. In the confinement field of a toroidal device, the in-out

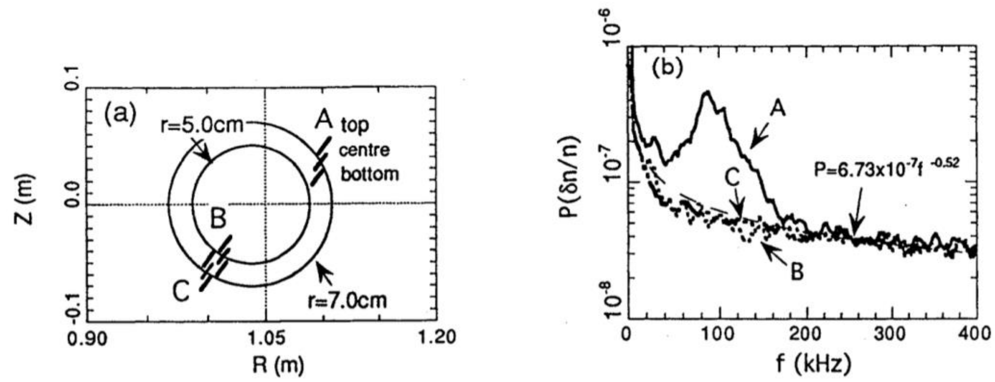

Fig. 1.6. Density fluctuation measurements with HIBP in the HFS and LFS. (a) Sample volume location. (b) Power spectra of density fluctuations [34].

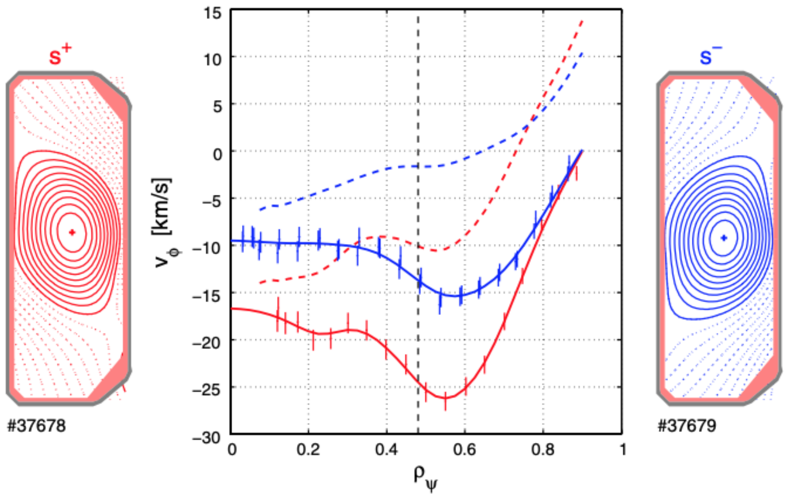

Fig. 1.7. Radial profiles of toroidal rotation velocity in different plasma geometries. The colors correspond to the respective plasma geometries, and the solid and dashed lines are carbon impurities and main ions, respectively. [35].

asymmetry, where the magnetic field strength is stronger inside (high-field side: HFS) and weaker outside (low-field side: LFS), is a central issue to be considered in turbulent transport. In the Texas Experimental Tokamak-Upgrade (TEXT-U), simultaneous measurements of density fluctuations on the high-field side and the low-field side have been performed using a HIBP [34]. As shown in Fig. 1.6, a comparison of the density fluctuation spectra of the high-field side and the low-field side shows that the low-field side has a peak at ~100 kHz, while the high-field side has no peak, which results in different fluctuation characteristics depending on the magnetic field strength. This shows the typical features of the "ballooning mode", which is the source of the disruption.

The tokamak à configuration variable (TCV) can produce a wide variety of plasma shapes and magnetic field configurations [35]. In plasma geometries with up-down asymmetry as shown in Fig. 1.7, it was shown that the profile of the toroidal rotation velocity measured by charge exchange recombination spectroscopy (CXRS) depends on the plasma geometry. In this experiment, it is assumed that there is no external toroidal

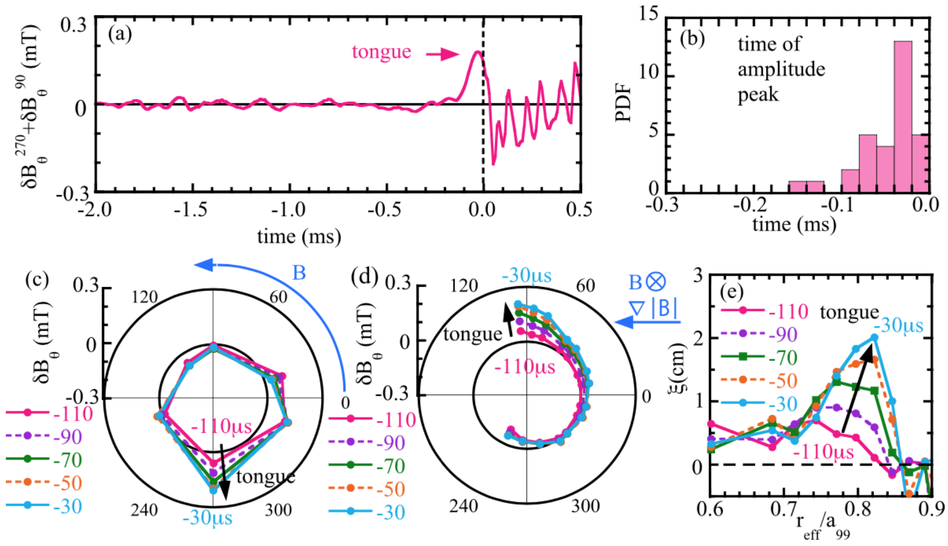

Fig. 1.8. (a) Time evolution of sum of magnetic field B_θ at φ = 90 and 270° in toroidal array and (b) probability distribution function of time of its amplitude peak and polar plot of magnetic field perturbation B_θ of (c) toroidal array and (d) poloidal array and (e) radial profiles of the plasma displacement during the 'tongue' event (t = −110, −90, −70, −50 and −30 μs). [36].

momentum source affecting the toroidal rotation. Such differences in toroidal rotation velocity can be attributed to changes in momentum transport due to the up-down asymmetry of the plasma, indicating the importance of the effect of the up-down asymmetry on the intrinsic rotation of the plasma.

In addition to asymmetries in magnetic field strength and plasma shape, it has been revealed that auxiliary heating causes symmetry breaking of the magnetic confinement plasma and asymmetries in the plasma distribution. In particular, auxiliary heating using NBI is used in various torus devices. One such phenomenon that directly affects the plasma confinement is the tongue phenomenon, which is caused by symmetry breaking due to such auxiliary heating. In the Large Helical Device (LHD), when energetic ions are injected by NBI, perturbations of the magnetic field are observed to be localized near the NBI port at toroidal angles and in the B×∇B drift direction at poloidal angles with temporal evolution as shown in Fig. 1.8 [36]. This result clearly shows the features of the

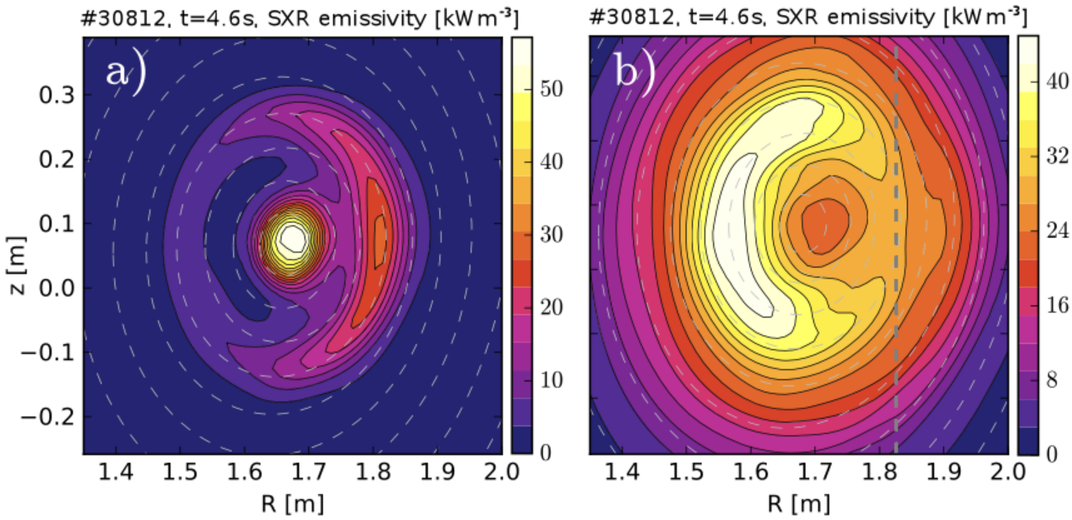

Fig. 1.9. Tomographic reconstruction of the SXR emissivity in ASDEX-U discharge 30812 at (a) 4.4 s with 2.5 MW of NBI heating only and (b) with additional 4.3 MW of ICRF, vertical dashed line indicates resonance location. Tungsten is localized in the HFS and LFS, respectively, by each auxiliary heating method. [38].

"tongue" phenomenon and indicates that the symmetry breaking of the magnetic surface is caused by the auxiliary heating. The "tongue" phenomenon is expected to lead to abrupt plasma disruption and should have a significant impact on the confinement of high-performance plasmas. It has also been reported that asymmetry of the distribution in tokamak devices can affect neoclassical transport, especially the localization of highly charged impurity ions inboard side the torus due to ICRH. ICRH increases the perpendicular velocity of minority ions, and the resulting mirror force pushes them toward the outboard side of the torus. The presence of such a non-uniform distribution of minority ions suggests the existence of a poloidally varying electrostatic potential. A poloidal electric field will be generated to satisfy the quasi-neutrality, driving the highly charged impurity ions toward the inboard side of the torus. It has been shown that the asymmetry affects neoclassical transport and turbulent generation [37-42]. In addition, asymmetry of the distribution has also been observed in plasma cross-section measurements using soft X-ray (SXR) tomography, as shown in Fig. 1.9 [38], and the understanding of the effect on neoclassical transport has been deepened experimentally.

As shown above, symmetry breaking of the turbulence field and asymmetry of the distribution affect not only the transport and confinement performance of the plasma, but also local to global nonlinear oscillations of the plasma such as Sawtooth oscillations. Further progress in understanding these phenomena is required to achieve the sustainment of high-performance plasmas.

1.4 Purpose of This Thesis

This thesis presents a global measurement system that can observe the entire plasma cross-section to discover the nonlinear effects of asymmetry in the steady-state plasma structure on the spatial pattern of the plasma. In recent years, our understanding of the effects of turbulence structure formation and symmetry breaking on plasma turbulence has been advanced by measuring structure and fluctuations in the plasma cross-section using imaging measurements such as Electron Cyclotron Emission, Gas Puff Imaging, Beam Emission Spectroscopy, Visible Light Emission and so on, have been carried out in toroidal and linear device [43-54]. However, the observation area of these measurement devices is limited to a localized region of the plasma cross-section. Simultaneous measurements of structure and fluctuations over the entire plasma cross-section are required to further our understanding of the structure formation of plasma turbulence and the effects of turbulence field symmetry breaking and/or asymmetry of the distribution on transport. Therefore, as a fundamental study to advance our understanding of such phenomena, simultaneous measurements of plasma fluctuation and structure were performed using a tomography system with a measurement line-of-sight covering the entire plasma cross-section, which is installed in a linear magnetized device with flexible access and high mobility.

This paper is composed as follows. Chapter 2 describes the linearly magnetized plasma device PANTA and the attached measurement devices, especially the tomography used in this study. Chapter 3 describes a reconstruction algorithm for tomography measurements called the Maximum Likelihood-Expectation Maximization method, and the Fourier-Bessel series expansion, Fourier-Rectangular series expansion, image correlation method, and modal polarization analysis used to analyze the spatial structure. Chapter 4 describes CECAME, a new conditional average method proposed in this study. In Chapter 5, the results on the relationship between the asymmetry of the background structure and the deformation of the spatial pattern of solitary oscillations obtained by tomographic measurements, which is the subject of this dissertation, are described in detail. Chapter 6 discusses the symmetric ($m = 0$) and asymmetric ($m \neq 0$) components resulting from the restoration of the spatial structure of the original solitary oscillations and nonlinear coupling when there is no asymmetry in the background structure. Chapter 7 summarizes the results presented above.

Chapter 2

Experimental Device and Diagnostics

In tokamak devices, it is necessary to consider the effects of magnetic field curvature and poloidal asymmetry in order to investigate turbulence dynamics. In addition, the location of the measurement device is also subject to various restrictions due to the heating system, coil configuration, vacuum vessel geometry, and other factors. On the other hand, linear devices have simple structures and easy access to the measurement system. Therefore, turbulence measurement using a linear device has been widely used to understand basic plasma turbulence dynamics in a simple manner. In the linear magnetized plasma device PANTA (Plasma Assembly Nonlinear Turbulence Analysis) [55], experimental studies of nonlinear interactions and structure formation in turbulence have been conducted. In order to investigate these issues, fluctuation measurements using electrostatic probes have been widely used in PANTA. However, there is a concern that the probe measurement may cause unexpected disturbances because the electrode is directly inserted into the plasma. Therefore, a new tomography system has been developed, which enables global accurate measurement of turbulence without any contact and disturbance to the plasma. In this chapter, we describe the outline of the PANTA system, the electrostatic probe as a local measurement system, and the tomography system as a global measurement system.

2.1 Linear Magnetized Device PANTA

PANTA is a compact linear device capable of generating a cylindrical plasma. The advantages of the compact linear device for turbulent fluctuation measurements include easy access to the measurement device, a simple magnetic field structure, ease of proposing experiments, and good reproducibility of experiments. Studies using linear apparatus have been conducted worldwide, such as CSDX [56,57], VINETA [58], MIRABELLE [59], LMD-U [60,61], and QT-Upgrade machine [62,63]. PANTA is dedicated to the study of plasma turbulence, and numerous studies have been conducted on structure formation [64-66], intermittent structure [67,68], turbulence transport [69,70] and so on.

A schematic diagram of PANTA is shown in Fig. 2.1. The vacuum vessel is 450 mm in

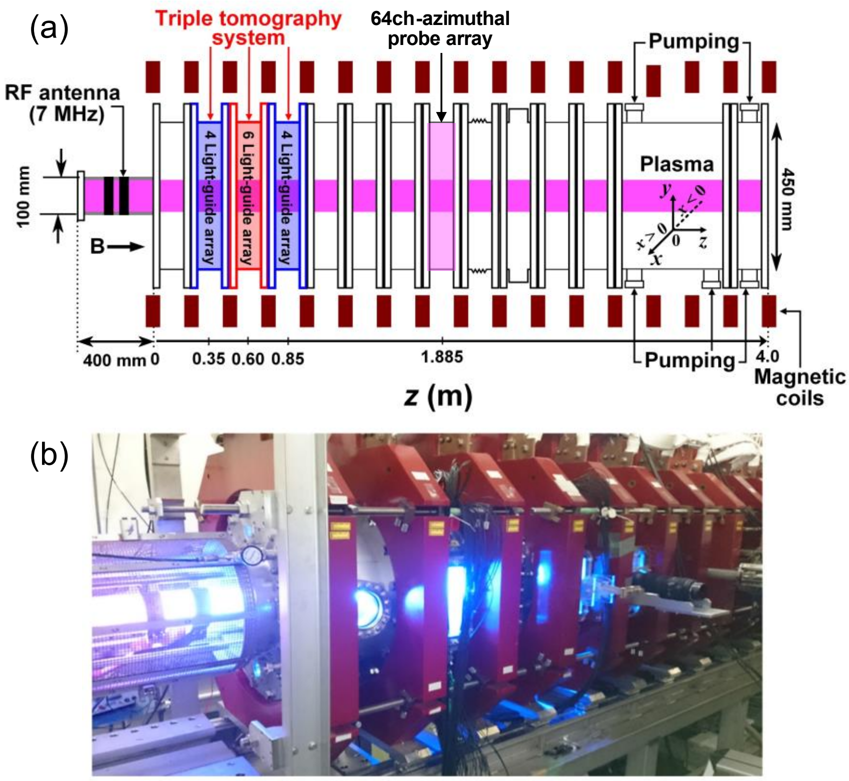

FIG.2.1. (a) Schematic of PANTA and (b) its photograph

diameter and 4050 mm long, and is modularized into 16 vacuum vessels, allowing for flexible selection of the location of the measurement system. Currently, the tomography system is installed in three cross sections near the plasma heating source, with 4 light-guide array tomography at axial distances z = 350 mm and 850 mm, and 6 light-guide array tomography at z = 600 mm. In addition, baffle plates with a diameter of 150 mm are inserted in the vacuum vessel near the plasma heating source and near the end plates, respectively, to prevent neutral gas from being released from the plasma region. In addition, a magnetic field is generated by 18 coils attached to the outside of the vacuum vessel, and the field strength can be flexibly set from 0.01T to 0.15T. Argon gas is used for plasma generation and is injected into the vacuum vessel from near the plasma heating source. The filling gas pressure is controlled by adjusting the flow rate with a mass flow meter, and the setting range is $8.0\times10^{-2} - 6.5\times10^{-1}$ Pa. In order to maintain a high vacuum condition, PANTA is equipped with five turbo molecular pumps at the rear of the vacuum vessel, exhausting air at 1100 L/s. The plasma source is heated by applying radio frequency (RF) to a copper double-loop antenna to excite helicon waves (1.5 ~ 6 kW, 7 MHz). The double-loop antenna is wound around the surface of a quartz tube 100 mm in diameter and 400 mm long, and is connected to a matching box and a high-frequency power supply. The matching box is adjusted to minimize the ratio of reflected power to input power by using two variable capacitors.

In PANTA, various experiments are performed by varying the main experimental parameters: gas pressure, magnetic field strength, and RF input power. By controlling these parameters, plasmas with different pressure gradients can be generated. Adjusting these parameters can change the pressure gradient in the direction perpendicular to the magnetic field of the plasma. Such pressure gradients can be energy source to drive turbulence influencing factors such as plasma velocity shear. Thus, the nonlinear

Table. 2.1: Typical operational condition in PANTA

Parameters	Avalable range
Background Gas Pressure	**8.0×10^{-5} – 1.0×10^{-4} [Pa]**
Filling Gas pressure	**8.0×10^{-2} – 6.5×10^{-1} [Pa]**
Magnetic Field Strength	**0.01 – 0.15 [T]**
RF input power	**1.5 – 6 [kW]**
Peak Electron Density	**1.0×10^{18} – 1.0×10^{19} [m^{-3}]**
Electron Temperature	**2 – 4 [eV]**

phenomena to be observed can be selected by controlling the experimental parameters. Here, Table 2.1 shows the typical parameter ranges for the plasmas that can be produced. In the PANTA experiment, two types of nonlinear phenomena have been observed by controlling the magnetic field strength and gas pressure, respectively. It is a “streamer” and “solitary oscillations”. Streamer is nonlinear phenomena caused by the nonlinear interaction between a drift wave and a mode called a “mediator” that is excited nonlinearly by the drift wave [13]. streamer is azimuthally localized and radially elongated, and is thought to accelerate radial transport. Therefore, there is concern that this may lead to a deterioration of confinement performance in fusion plasmas. Solitary oscillations are a nonlinear phenomenon formed by nonlinear coupling of fluctuations to generate harmonics. The detailed spatial structure is described in Chapter 5. Each of these nonlinear phenomena has a dominant experimental regime, with streamer being observed in the low gas pressure and medium magnetic field regime, and solitary oscillation being observed in the wide range parameter regime [65].

2.2 Diagnostics

Probe measurement is the most fundamental technique for measuring physical quantities of plasma (density, temperature, potential, etc.). This is because of its simple structure and capability to measure various plasma parameters with high temporal and spatial resolution. In particular, the relatively low temperature of PANTA plasmas makes them suitable for the electrostatic probe measurements. Therefore, in addition to the common Langmuir probe [71], various types of probes such as Mach probes [66,72], ball-pen probes [73-75], and Reynolds stress probes [25,76] have been used to measure fluctuations in magnetized plasma. However, the plasma parameters obtained through probe measurements are localized, making it challenging to comprehensively understand the global nature of plasma turbulence in detail. Therefore, it is necessary to develop a measurement system that can simultaneously measure the entire plasma. In recent years, turbulence measurements using tomography systems have been actively used in PANTA to investigate the global nonlinear interaction of turbulence at different scales. Here we describe the Langmuir probe and 64-ch probes used in the PANTA experiments as well as the global measurement system, tomography, used in this study.

2.2.1 Basic Langmuir Probe

The Langmuir probe method was developed by Langmuir and Mott Smith in 1926 [71]. A small metal probe tip is inserted directly into the plasma and a bias voltage V_p is applied to measure the probe current I_p. From the dependence of the probe current I_p and the bias voltage V_p, a characteristic curve called the I_p-V_p curve can be drawn. The I_p-V_p curve is divided into three regions according to the bias voltage applied: the electron saturation region, the electron deceleration region, and the ion saturation region.

By using the changes in the probe current in each region, we can evaluate the physical quantities of the plasma such as electron density, electron temperature, floating potential, and plasma potential. Therefore, fluctuation measurements using Langmuir probes are the most common method for determining the time evolution of physical quantities in plasmas.

2.2.2 64-Channel Azimuthal Probe Array

To investigate nonlinear interactions between fluctuations, the wavenumber and frequency of each fluctuation is required. As one of the methods to obtain this information, fluctuation measurement using a poloidal probe array with multiple Langmuir probes arranged in an azimuthal direction has been used in various linear devices [77]. In PANTA, a poloidal probe array called "64 channel azimuthal probe array" (64ch-probe array) is in operation and is used to investigate structure formation and nonlinear coupling processes [64-66,78,79]. As shown in Fig. 2.2, the 64ch-probe array consists of 64 azimuthally arranged Langmuir probes, equally spaced, each of which can measure density and

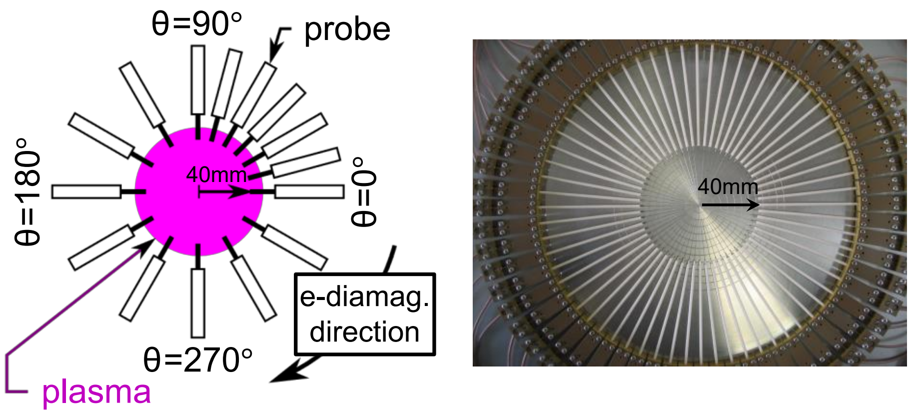

FIG.2.2: Schematic and photograph of 64-channel azimuthal probe array.

potential fluctuations. The 64ch-probe array is located at an axial distance of z = 1885 mm from PANTA as shown in Fig. 2.1. Each probe tip is made of tungsten that is high-melting-point metal material, 0.8 mm in diameter and 3 mm in length, and is located 40 mm radially from the center of the PANTA plasma with an azimuthal spacing of 3.9 mm. Since there are 64 probes in the azimuthal direction, the azimuthal mode number that can be measured is m = 32. Here, the azimuthal mode number m is defined by $m = k_\theta r_p$, and $r_p = 40$ mm, so the measurable azimuthal mode number m = 1~32 corresponds to the wave number $k_\theta = 0.025\ \mathrm{mm}^{-1} \sim 0.8\ \mathrm{mm}^{-1}$. From the above, a two-dimensional power spectrum of wavenumber and frequency at $r = 40$ mm can be obtained, and the nonlinear interaction of wavenumber and frequency between fluctuations can be analyzed. The data acquisition for the 64ch-probe is differ from the tomography system, it is digitized by using an ADC named "WE7000" with a sampling rate of 1MHz.

2.2.3 Tomography System

Plasma turbulence is a phenomenon in which structures of different scales are coexist, such as microscale structures like drift waves, mesoscale structures like zonal flow and streamer, and macroscale structures that exert influence across the entire plasma [10,13,17]. Since these structures grow and decay due to nonlinear interactions between structures of different scales, it is necessary to measure disparate scale structures simultaneously in order to understand the detailed physical mechanisms. However, it is difficult to simultaneously measure structures with different spatial and temporal scales, and even advanced measurement methods such as HIBP [80], reflectometer [81], and any other imaging measurements are limited to localized regions of the plasma cross-section. Fast imaging cameras have been used in linear devices such as NAGDIS-II [82],

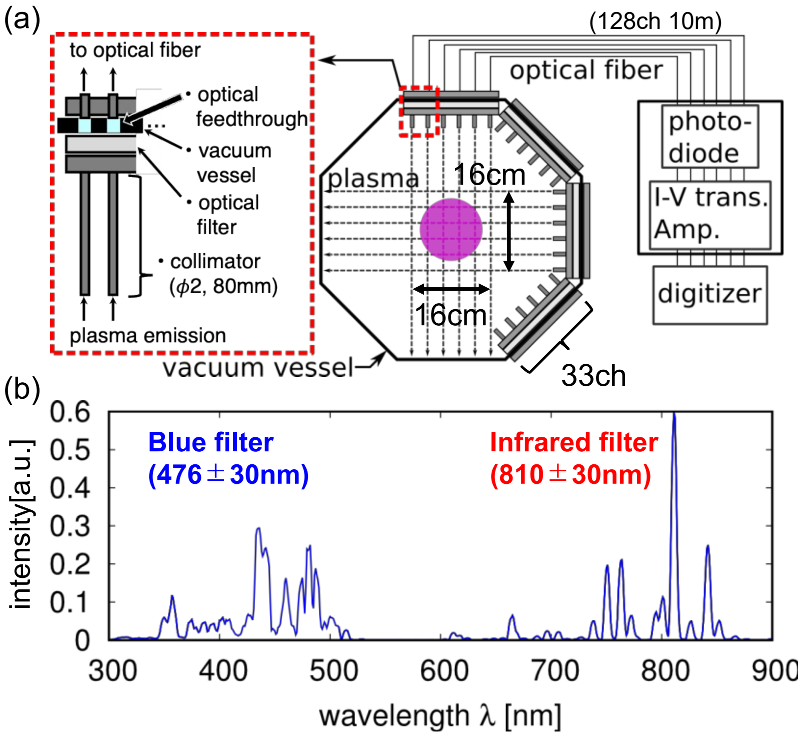

FIG.2.3: (a) Schematic of 4 light-guide array tomography system and data acquisition. (b) Emission spectrum from argon plasma and optical filter region.

MIRABELLE [83], and PANTA [84] for structural measurements over the entire plasma cross-section. However, structural measurements with fast imaging cameras measure plasma cross sections that are integrated in the direction of magnetic field lines. In addition, there is a concern that the sampling frequency is lower than that of probe measurements. Therefore, in order to obtain detailed features of plasma turbulence, it is necessary to develop a new global measurement system that can measure local plasma cross sections at high sampling frequencies and can measure a wide range of fluctuations from micro- to macro- scales. One candidate for an effective measurement system to address these issues is a computer tomography (CT) system. Since the turbulence to be observed is a micro- to macro-scale structure, the tomography should have sufficient temporal and spatial resolution, requiring about the drift wave frequency and ion Larmor radius, respectively. To achieve such resolution, plasma turbulence tomography requires many measurement lines-of-sight and good image reconstruction algorithms.

The spatial structure of plasma has been determined using tomography systems on linear and toroidal devices of various sizes, such as W7-X [85], JET [86,87], LHD [88,89], Mistral [90], CSDX-U [91], and so on. In PANTA, the tomography system [92-94] dedicated to plasma turbulence measurement has been developed. Figure 2.3(a) shows a schematic of the tomography system installed in PANTA, in which 4 pairs of light-guide arrays are arranged at 45-degree intervals in the azimuthal direction of the plasma. Each light-guide array has 33 fiber channels, and a total of 132 fiber channels are used to measure the line-integrated emission from the plasma. The measurement lines-of-sight cover the plasma and are equally spaced within ±80 mm from the center of the device (plasma center). The line-of-sight integral data obtained with 132ch is used to reconstruct an 11×11 grid image by using the MLEM method described later in Chapter 3. The measurement range is $16\ \mathrm{cm} \times 16\ \mathrm{cm}$, as it depends on the line-of-sight range of the light-guide array. Therefore, the spatial resolution of the 4 light-guide array tomography system is approximately 1.4 cm, which is comparable to the ion Larmor radius of the PANTA plasma. One light-guide array consists of a collimator, an optical filter, and a feedthrough. The collimator is made of an aluminum pipe with an inner diameter of 2 mm and a length of 80 mm, which limits the focused plasma emission in the line-of-sight direction. This reduces the effect of the line-of-sight spread that is taken into account when reconstructing images from the obtained line-of-sight-integrated emission. The optical filter detects only the emission of specific wavelengths. Figure 2.3(b) shows the emission spectrum from the argon plasma and the region of the optical filter $\lambda \pm \Delta\lambda$. Here, λ and $\Delta\lambda$ represents the central wavelength and full width at half maximum of the optical filter, respectively. The blue filter ($\lambda \pm \Delta\lambda$: 476 ± 30 nm) detects the emission of argon ions (ArII), and the infrared filter (λ ± Δλ: 810 ± 30 nm) detects the emission of neutral particles (ArI). In this study, ArI emission is observed by using the infrared filter. Here, if only one emission line is included in the transmitting region of the optical filter, the amount of light is not sufficient and fluctuation measurement is hindered, so multiple lines are included in the transmitting region to compensate for the amount of light. On the other hand, there is a concern that including multiple lines in the transmitting region of an optical filter makes it difficult to determine physical quantities (e.g., density and temperature). However, tomography measurement mainly focuses on the measurement of emission fluctuations across the entire plasma cross-section. Therefore, while allowing for a certain degree of difficulty in understanding physical quantities, the time evolution of the spatial structure is accurately measured by including multiple emission lines in the transmitting region of the optical filter.

The expression of the ArI emission $\varepsilon_{\mathrm{ArI}}$ is a bit complicated. As in Ref. [95], $\varepsilon_{\mathrm{ArI}}$ can be modeled as follows.

$$\varepsilon_{\mathrm{ArI}} \approx B(T_e) n_e n_0. \tag{2.1}$$

Where $T_{\mathrm{e}}, B(T_{\mathrm{e}}), n_{\mathrm{e}}$, and n_0 represent the electron temperature, reaction rate, electron density, and argon gas density, respectively. In addition, the ArI emission fluctuations can be written as follows,

$$\frac{\tilde{\varepsilon}_{\mathrm{Ar\,I}}}{\bar{\varepsilon}_{\mathrm{Ar\,I}}} \approx \frac{\bar{T}_{\mathrm{e}}}{B} \frac{\partial B}{\partial T_{\mathrm{e}}} \frac{\tilde{T}_{\mathrm{e}}}{\bar{T}_{\mathrm{e}}} + \frac{\tilde{n}_{\mathrm{e}}}{\bar{n}_{\mathrm{e}}} + \frac{\tilde{n}_0}{\bar{n}_0}. \tag{2.2}$$

Where $\bar{A}$ and $\tilde{A}$ in each physical quantity represent the mean and fluctuation of A, respectively. To determine n_0, consider the equilibrium conditions of monovalent ionization and recombination to neutral particles. Under the assumption that transport is negligible, the reaction rate equation for n_0 can be written as follows,

$$\frac{dn_0}{dt} = -S_0(T_e)n_e n_0 + R_0(T_e)n_e n_i. \tag{2.3}$$

where $S_0(T_\mathrm{e})$ and $R_0(T_\mathrm{e})$ represent the ionization rate from Ar gas to Ar+ and the recombination rate from Ar+ to Ar gas, respectively, satisfying $S_0 n_0 = R_0 n_i$ at steady state. Hence, $\tilde{n}_0$ can be expressed from $n_0 = R_0/S_0\, n_i \approx R_0/S_0\, n_e = P(T_e)n_e$ as follows,

$$\frac{\tilde{n}_0}{\bar{n}_0} \approx \frac{\bar{T}_e}{P}\frac{\partial P}{\partial T_e}\frac{\tilde{T}_e}{\bar{T}_e} + \frac{\tilde{n}_e}{\bar{n}_e}. \tag{2.4}$$

From the above, the reaction coefficients are defined as $B(T_e) \propto T_e^{\alpha_0}$, $S_0(T_e) \propto T_e^{\alpha_\mathrm{ionize}}$, $R_0(T_e) \propto T_\mathrm{e}^{\alpha_\mathrm{recomb}}$, and $P(T_e) \propto T_e^{(\alpha_\mathrm{recomb} - \alpha_\mathrm{ionize})}$ using the each reaction rates, and α_0, α_ionize, and α_recomb are assumed to be constant in the vicinity of mean T_e. The ionization coefficients α_0 and α_ionize should be about 2-4 at $T_\mathrm{e} \sim 3$ eV from Lotz's empirical formula [96]. The recombination coefficient α_recomb is suggested by Seaton's equation for hydrogen-like atoms [97] to be negative but larger than -1. Therefore, $\alpha_\mathrm{recomb} - \alpha_\mathrm{ionize} < 0$. From the above, Eq. (2.2) can be rewritten as follows,

$$\frac{\tilde{\varepsilon}_\mathrm{Ar\,I}}{\bar{\varepsilon}_\mathrm{Ar\,I}} \approx \delta\frac{\tilde{T}_\mathrm{e}}{\bar{T}_\mathrm{e}} + 2\frac{\tilde{n}_\mathrm{e}}{\bar{n}_\mathrm{e}}. \tag{2.5}$$

where $\delta = \alpha_0 + \alpha_\mathrm{recomb} - \alpha_\mathrm{ionize}$, and δ can be estimated using the same procedure as in Ref. [91].

In addition, fluorescent glass, which converts ultraviolet light to visible light, is used in the feedthrough to prevent degradation of the optical fiber, as it is envisioned to be used for high-temperature plasma in the future. The length of the optical fiber cable was set to 10 m to improve the signal-to-noise ratio when transferring the obtained plasma emission. In addition, the intensity calibration of the emission in the fiber optic cable is also performed using an oscilloscope, and the error range is within a few %.

The plasma emission signal measured by tomography is detected by a photodiode with

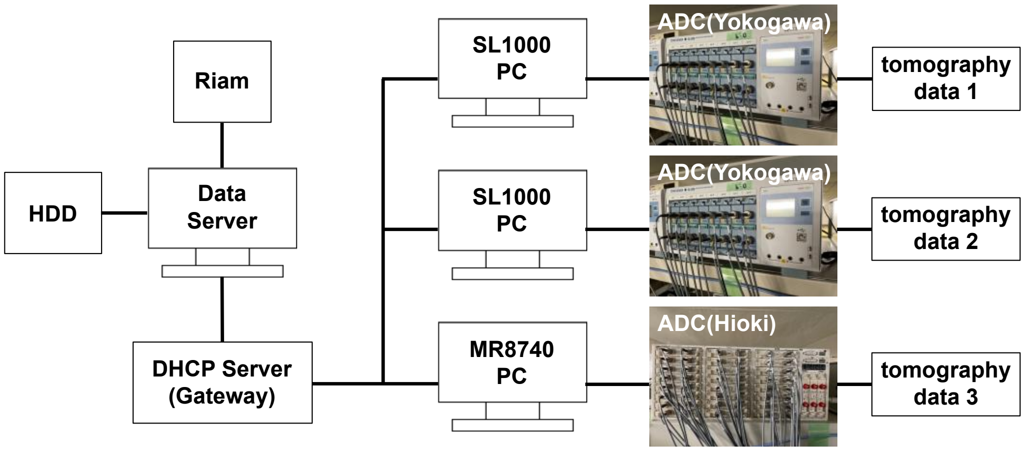

FIG.2.5: Tomography data acquisition and network system in PANTA

low noise characteristics and converted to a voltage signal by an I-V conversion amplifier. The gain and frequency bandwidth of the amplifier are 10^8 V/A and up to 50 kHz, respectively. The noise of the tomography system depends on the noise of the amplifier, whose level is less than ±50 mV. The data acquisition of the detected voltage signals is excuted using Analogue-to-Digital Convertors (ADC) named "SL1000" by “Yokogawa” and "MR8740" by “Hioki”, both equipped with a sampling frequency of 1 MHz. In this study, the data of 4 light-guide array tomography was collected using the "SL1000". The data acquisition procedure of the tomography system in PANTA is shown in Fig. 2.5.

Chapter 3

Analysis Method for Tomography Data

In magnetized plasmas, it is difficult to study the time evolution of turbulent phenomena with complex structures. In particular, while data obtained by global measurement devices such as tomography are novel, huge amounts of data must be processed to extract important phenomena. For this purpose, it is necessary to apply image analysis methods suitable for tomographic data. This chapter is described analytical methods for extracting global and local properties of nonlinear oscillations from tomographic data.

3.1 Maximum Likelihood-Expectation Maximization

There are many methods for two-dimensional reconstruction of projection data obtained by tomography systems, including algebraic methods, statistical methods, and methods using basis functions [98-102]. In our laboratory, since plasma turbulence is measured from the plasma emission distribution, we use a statistical method named the Maximum Likelihood-Expectation Maximization method (MLEM method) [103]. The MLEM method have two advantages: (1) can be reconstructed without any basis function and (2) does not return emission values less than or equal to 0. The MLEM method is a reconstruction technique commonly used in the medical field. Consider a reconstruction algorithm that estimates the local emission ε_j at the j-th grid as shown in Fig.3.1. The line-integrated emission g_i measured at the i-th detector can be written as $g_i = \sum_j C_{ij}\varepsilon_j$, where C_{ij} is the probability of detecting a photon from the j-th grid at the i-th detector. In

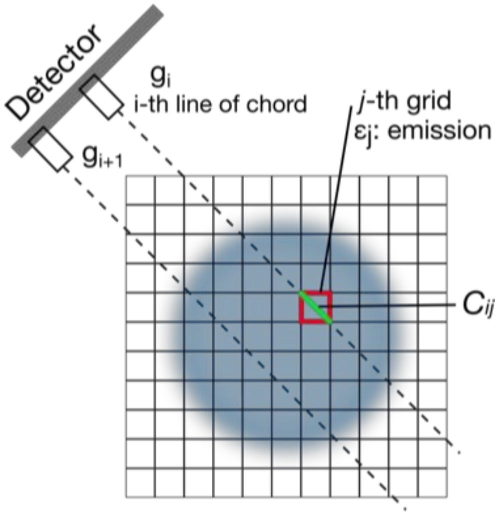

FIG. 3.1: Image reconstruction by MLEM method

addition, since the number of photons emitted by each grid follows a Poisson distribution, the probability that photons from the *j*-th grid x_{ij} will enter the *i*-th detector is

$$P(x_{ij}) = e^{-C_{ij}\varepsilon_j} \frac{C_{ij}^{x_{ij}} \varepsilon_i^{x_{ij}}}{x_{ij}!}. \tag{3.1}$$

Thus, the simultaneous probability that the realization of grid *j* in all detectors is x_{ij} can be represented as follows.

$$P(x) = \prod_i \prod_j P(x_{ij}) = \prod_i \prod_j e^{-C_{ij}\varepsilon_j} \frac{C_{ij}^{x_{ij}} \varepsilon_j^{x_{ij}}}{x_{ij}!}. \tag{3.2}$$

If this simultaneous probability is determined by the emission intensity ε_j, the log-likelihood can be represented as follows.

$$\begin{aligned} L(\varepsilon) &= \ln\big(P(x)\big) \\ &= \ln\left(\prod_i \prod_{\mathrm{j}} e^{-C_{ij}\varepsilon_j} \frac{C_{ij}^{x_{ij}} \varepsilon_j^{x_{ij}}}{x_{ij}!}\right) \end{aligned}$$

$$= \sum_i \sum_j \left(-C_{ij}\varepsilon_j + x_{ij}\left(\ln C_{ij} + \ln \varepsilon_i\right) - \ln x_{ij}!\right)$$
$$= \sum_i \sum_j \left(-C_{ij}\varepsilon_j + x_{ij} \ln \varepsilon_i\right) + const. \tag{3.3}$$

Where x_{ij} is not directly measurable. Therefore, it is necessary to calculate the estimate that maximizes the conditional expectation of the emission estimates for k-th iterations ε_j^k and the log-likelihood function $L(\varepsilon)$ in order to perform maximum likelihood estimation. The conditional expectation of ε_j^k and $L(\varepsilon)$ is shown in the following formula.

$$Q\left(\varepsilon \middle| \varepsilon^k\right) = E\left[\ln P(x) | g, \varepsilon^k\right]$$
$$= \sum_i \sum_j \left(-C_{ij}\varepsilon_j + E\left[x_{ij} \middle| g, \varepsilon^k\right] \ln \varepsilon_j\right) + const. \tag{3.4}$$

To obtain the conditional expectation of x_{ij}, the posterior probability of x_{ij} when the line-of-sight integral of the emission obtained at the i-th detector is g_i, can be represented using Bayes' theorem as follows.

$$P\left(x_{ij} \middle| g_i\right) = \frac{P\left(x_{ij}\right) P\left(g_i \middle| x_{ij}\right)}{P\left(g_i\right)}. \tag{3.5}$$

Here, the probability that the amount of line-of-sight integration is g_i is shown as follows.

$$P\left(g_i\right) = e^{-\sum_m C_{im}\varepsilon_m} \frac{\left(\sum_m C_{im}\varepsilon_m\right)^{g_i}}{g_i!}. \tag{3.6}$$

Furthermore, since $P\left(g_i \middle| x_{ij}\right) = P(g_i - x_{ij})$, it can be rewritten as follows.

$$P\left(g_i \middle| x_{ij}\right) = e^{-\sum_m\left(C_{im}\varepsilon_m - C_{ij}\varepsilon_j\right)} \frac{\left(\sum_m\left(C_{im}\varepsilon_m - C_{ij}\varepsilon_j\right)\right)^{\left(g_i - x_{ij}\right)}}{\left(g_i - x_{ij}\right)!}. \tag{3.7}$$

Therefore, Eq. (3.5) can be rewritten from Eqs. (3.1), (3.6), and (3.7) as follows.

$$P(x_{ij}|g_i) = \frac{g_i!}{x_{ij}!(g_i\text{-}x_{ij})!}\left(\frac{C_{ij}\varepsilon_j}{\sum_m C_{im}\varepsilon_m}\right)^{x_{ij}}\left(\frac{\sum_m(C_{im}\varepsilon_m\text{-}C_{ij}\varepsilon_j)}{\sum_m C_{im}\varepsilon_m}\right)^{(g_i\text{-}x_{ij})}. \tag{3.8}$$

It is shown that $P(x_{ij}|g_i)$ follows a binomial distribution, and the conditional expectation of x_{ij} can be represented as follows.

$$E[x_{ij}|g, \varepsilon^k] = g_i\frac{C_{ij}\varepsilon_j^k}{\sum_m C_{im}\varepsilon_m^k}. \tag{3.9}$$

The conditions under which a function substituting Eq. (3.9) into Eq. (3.4) takes extreme values are as follows.

$$\begin{aligned}\frac{\partial}{\partial\varepsilon_j}Q(\varepsilon|\varepsilon^k) &= \frac{\partial}{\partial\varepsilon_j}\left[\sum_i\sum_j(\text{-}C_{ij}\varepsilon_j + E[x_{ij}|g, \varepsilon^k]\ln\varepsilon_j) + const\right] \\ &= \text{-}\sum_i C_{ij} + \frac{1}{\varepsilon_j}\sum_i g_i\frac{C_{ij}\varepsilon_j^k}{\sum_m C_{im}\varepsilon_m^k} = 0.\end{aligned} \tag{3.10}$$

Thus, the estimated local emission ε_j^{k+1} from the k+1-th iterative operation can be represented as follows.

$$\varepsilon_j^{k+1} = \frac{\varepsilon_j^k}{\sum_i C_{ij}}\sum_i\frac{C_{ij}g_i}{\sum_m C_{im}\varepsilon_m^k}. \tag{3.11}$$

In actual calculations, iterative calculations are performed until the estimated local emission obtained by iterative calculations satisfies the following,

$$|\varepsilon_j^{k+1}\text{-}\varepsilon_j^k| < \delta,\ \delta \sim 10^{-5}\varepsilon_{\max}^k, \tag{3.12}$$

where $\varepsilon_{\max}^k$ is the maximum value of local emission at the k-th iteration.

3.2 Fourier-Bessel Function Expansion

Fitting using the Fourier-Bessel function expansion (FBF) is often used to analyze the global dynamics from the spatial structure of plasmas obtained by tomography or fast cameras [84, 104-107]. The Fourier-Bessel series expands the emission image as follows.

$$\begin{aligned}\hat{\varepsilon}(r,\theta) &= \sum_i A_i \phi_i(r,\theta) \\ &= \sum_{m,n} A_{m,n} J_m(k_{mn} r)\cos(m\theta) + B_{m,n} J_m(k_{mn} r)\sin(m\theta)\,. \end{aligned} \tag{3.13}$$

Where A_i and $\phi_i(r,\theta)$ represent the expansion coefficients and the i-th basis function of the Fourier-Bessel expansion, respectively. Also, $J_m(r)$, k_{mn}, and m in the basis functions represent the m-th Bessel function, the zero point of the n-th Bessel function, and azimuthal mode number, respectively. Since the Fourier-Bessel basis function $\phi_i(r,\theta)$ includes the $\cos(m\theta)$ and $\sin(m\theta)$, the index i of the Fourier-Bessel basis functions can be expressed by using the azimuthal mode number and the radial node number as follows.

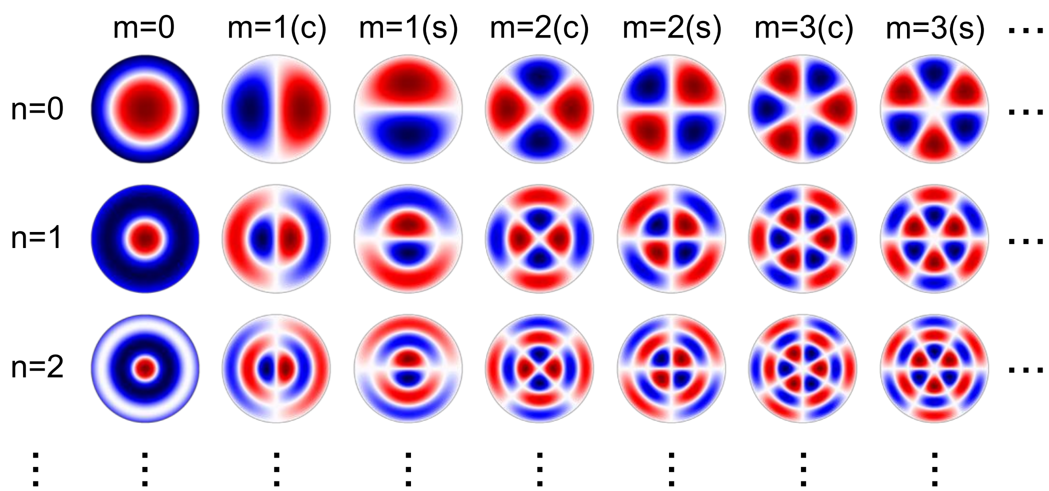

FIG. 3.2: Basis in Fourier-Bessel function series expansion. In parentheses “c” and “s” correspond to the cos and sin components of the respective modes.

$$i = n_{\max}(0) + \sum_{j=1}^{m-1} 2n_{\max}(j) + 2n - 1\,,$$

$$i = n_{\max}(0) + \sum_{j=1}^{m-1} 2n_{\max}(j) + 2n\,. \tag{3.14}$$

Where $n_{\max}(m)$ is the maximum radial node number in the azimuthal mode number. From the above, the Fourier-Bessel coefficients are obtained by fitting the basis functions as shown in Fig. 3.2 to the emission distribution of the tomography, and the spatial structure is reconstructed. Also, the Fourier-Bessel coefficients A_i are determined by the least-squares method to minimize the error between the original emission distribution $\varepsilon(r_j, \theta_j)$ and the Fourier-Bessel expanded emission distribution $\hat{\varepsilon}(r_j, \theta_j)$ as follows.

$$\begin{aligned}\chi^2 &= \sum_j \left(\varepsilon(r_j, \theta_j) - \hat{\varepsilon}(r_j, \theta_j)\right)^2 + \gamma|\hat{\varepsilon}(r, \theta)|^2 \\ &= \sum_j \left(\varepsilon(r_j, \theta_j) - \sum_i A_i \phi_i(r_j, \theta_j)\right)^2 + \gamma \sum_i A_i^2\,.\end{aligned} \tag{3.15}$$

Here, in order to maintain the normal orthogonality, the regularization parameter shown in the second term on the right side of equation (3.15) is introduced, at which time $\gamma = 8.0\times10^{-3}$. From the above, the Fourier-Bessel coefficient A_i can be obtained by solving the following equation.

$$\sum_l (\Phi_{kl} + \lambda\delta_{kl}) A_l = B_k. \tag{3.16}$$

Where, Φ_{kl} and B_k are defined as,

$$\begin{aligned}\Phi_{kl} &= \sum_j \phi_{kj}\phi_{lj} \\ B_k &= \sum_j \phi_{kj}\varepsilon_j\,,\end{aligned} \tag{3.17}$$

with $\phi_{kl} = \phi_k(r_j, \theta_j)$, where k and l represent the coordinate numbers of the basis and spatial coordinate (r, θ), respectively.

3.3 Fourier-Rectangular Function Expansion

For analyzing the dynamics of local structures from tomography images, a Fourier-Rectangular function expansion (FRF) has been developed. This method employs a Fourier series in the azimuthal direction and a rectangular function in the radial direction [108]. Consequently, analysis of local structures in the radial direction can be performed. Using the FRF expansion, the emission distribution can be approximated as follows.

$$\varepsilon(r, \theta) \simeq \sum_{n=1}^{N_r} a_{0,n} \frac{R_n(r)}{\sqrt{2}} + \sum_{n=1}^{N_r} \sum_{m=1}^{M} R_n(r) \left[a_{m,n} \cos(m\theta) + b_{m,n} \sin(m\theta) \right]$$

$$= \sum_{l=1}^{L} a_l \phi_l(r, \theta) . \tag{3.18}$$

where $R_n(r)$ represents a rectangular function and is defined as follows.

$$R_n(r) = \begin{cases} \dfrac{N_r}{a} \sqrt{\dfrac{2}{\pi(2n\text{-}1)}}, & (\dfrac{a(n\text{-}1)}{N_r} < r < \dfrac{an}{N_r}) \\ 0, & (\text{else}) \end{cases} . \tag{3.19}$$

In eq. (3.18), the correspondence of the basis function is denoted as follows.

$$\phi_l(r, \theta) = R_n(r)/\sqrt{2} \ \ [l{=}n,\ m{=}0]$$

$$\phi_l(r, \theta) = R_n(r) \cos(m\theta) \ \ [l{=}2N_r(m\text{-}1){+}N_r{+}n,\ m{>}0]$$

$$\phi_l(r, \theta) = R_n(r) \sin(m\theta) \ \ [l{=}2N_r(m\text{-}1){+}N_r{+}n{+}1,\ m{>}0].$$

The basis functions also satisfy the following quasi-normal relationship.

$$\int_0^a \int_0^{2\pi} \phi_i(r, \theta) \phi_j(r, \theta) dS = \delta_{ij}. \tag{3.20}$$

Where δ_{ij} is Kronecker's delta. The expansion coefficients can be given by the following equation.

$$a_l = \int \varepsilon(r, \theta)\, \phi_l(r, \theta) dS. \tag{3.21}$$

The coefficients of the symmetric ($m = 0$) and asymmetric components ($m > 0$) are defined as $a_{0,n}$, $a_{m,n}$, and $b_{m,n}$, respectively, and can be obtained from the following equation.

$$a_{0,n} = \int \varepsilon(r, \theta) \frac{R_n(r)}{\sqrt{2}} dS, \tag{3.22}$$

$$a_{m,n} = \int \varepsilon(r, \theta) R_n(r) \cos(m\theta)\, dS, \tag{3.23}$$

$$b_{m,n} = \int \varepsilon(r, \theta) R_n(r) \sin(m\theta)\, dS. \tag{3.24}$$

Using these FRF coefficients, the radial dependence of amplitude and declination for each mode structure can be investigated.

The coefficients expanded in the cylindrical coordinate system by FRF expansion can be converted to the Cartesian coordinate system. A two-dimensional image of the emission distribution in the Cartesian coordinate system can be expressed as follows.

$$\varepsilon(x,y) \simeq \sum_{n=0}^{N} \varepsilon_n \delta_n(x,y). \tag{3.25}$$

Where N and ε_n are the grid number on the two-dimensional image and the emission on the n-th grid, respectively. Substituting eq. (3.25) into eq. (3.21), the FRF coefficient of $\varepsilon(x,y)$ in the Cartesian coordinate system can be expressed as follows.

$$a_l = \int \left(\sum_{n=0}^{N} \varepsilon_n \delta_n\big(x(r, \theta), y(r, \theta)\big) \right) \phi_l(r, \theta) dS$$

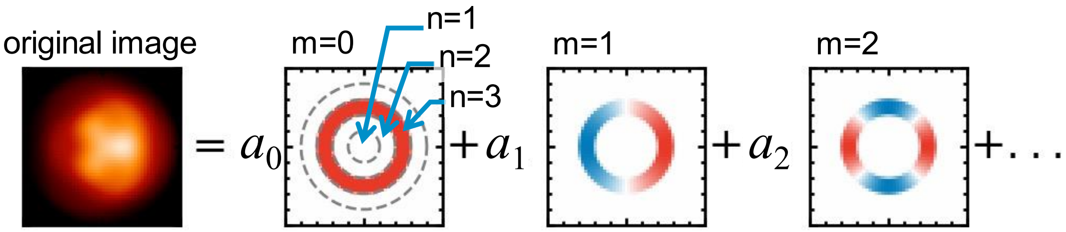

Fig. 3.3: Schematic of pattern reconstruction for each band of radial positions by FRF expansion. In the figure, m, n, and a_l (l = 0, 1, 2, …) correspond to the azimuthal mode number, the number of nodes in the radial band, and a_l in Eq. (3.26), respectively.

$$= \sum_{n=0}^{N} \varepsilon_n \int_{\Delta S_n} \phi_l\big(r(x,y),\, \theta(x,y)\big) dS$$

$$= \sum_{n=0}^{N} \Phi_{l,n} \varepsilon_n \,. \tag{3.26}$$

Where $\Phi_{l,n}{=}\phi_l\big(r(x,y),\,\theta(x,y)\big)dxdy$ means the area of the l-th FRF basis in the n-th Cartesian grid. Consequently, the two-dimensional image is expanded as a pattern of bands of radial positions, as shown in Fig. 3.3. Moreover, by using the transformation matrix $\Phi_{l,n}$, the FRF coefficients can be expressed as the emission at the local position ($r(x, y)$, $\theta(x, y)$) in the Cartesian coordinate system. Therefore, it is possible to convert between FBF and FRF expansion images.

3.4 Field Operator Method

Global measurement is advanced in the study of plasma turbulence because it enables simultaneous measurement of the entire plasma cross-section. To understand the dynamics of plasma turbulence from the data obtained from such measurements, it is necessary to evaluate the characteristics of the spatial structure of the plasma directly from a two-dimensional image. Hence, a method was proposed to extract features from two-dimensional images and to apply pattern recognition to quantitatively investigate structural changes in plasmas directly from 2D images [109]. In this method, if $\varphi(r,\theta)$ and $\phi(r,\theta)$ are two-dimensional images defined on some area S, the inner product is defined as follows.

$$\langle\varphi,\phi\rangle = \int \varphi(r,\theta)\phi(r,\theta)dS. \tag{3.27}$$

Using eq. (3.27), we define the similarity index σ, which evaluates the similarity between two-dimensional images obtained from tomography by applying the digital image correlation method [110], as follows,

$$\begin{aligned}\sigma(\varphi,\phi) &= \frac{\langle\varphi,\phi\rangle}{\sqrt{\langle\varphi^2\rangle\langle\phi^2\rangle}} \\ &= \frac{\sum_{mn}\left(A_{mn}A'_{mn}+B_{mn}B'_{mn}\right)}{\sqrt{\sum_{mn}\left(A_{mn}^2+B_{mn}^2\right)\sum_{mn}\left(A'^2_{mn}+B'^2_{mn}\right)}}.\end{aligned} \tag{3.28}$$

Where (A,B) and (A',B') are the Fourier-Bessel coefficients of $\varphi(r,\theta)$ and $\phi(r,\theta)$, respectively. The deformation in eq. (3.28) exploits the orthonormal nature of the FBF. In addition, creative use of the FBF series can provide a method for further image quantification. For example, the spatial structure of a plasma is thought to be a symbiosis of structures with various azimuthal mode numbers, and the dominant mode structure changes with time, resulting in structural changes. Therefore, by using the FBF coefficients, the average number of azimuthal modes can be defined from each two-dimensional image as shown in the following equation.

$$\overline{m} = \frac{\sum_{mn} m\left(A_{mn}^2 + B_{mn}^2\right)}{\sum_{mn}\left(A_{mn}^2 + B_{mn}^2\right)}. \tag{3.29}$$

From the above equation, it is possible to quantify how the spatial structure changes over time by examining the time variation of the averaged azimuthal mode number.

3.5 Modal Polarization Analysis Method

The Stokes parameter is used in optics as a statistical measure of polarization state. It is also used in the study of plasma turbulence to understand the dynamics of spatial structure [111]. Recently, a method has been proposed to investigate the local polarization state in the radial direction for each mode structure by combining polarization analysis using the Stokes parameter and FRF expansion, which is excellent for local spatial structure analysis. With the aforementioned FRF expansion, the FRF coefficients $a_m(r_n, t)$ and $b_m(r_n, t)$ can be used to define the complex coefficients of a two-dimensional image as in the following equation.

$$c_m(r_n, t) = a_m(r_n, t) + ib_m(r_n, t). \tag{3.30}$$

Here, the absolute value of the complex coefficient $|c_m(r_n, t)|$ and the polarization $\theta_m(r_n, t) = \arg[c_m(r_n, t)]$ correspond to the amplitude and polarization of each mode structure, respectively, and can be obtained for each radial position r_n. For example, if the declination angle $\theta_m(r_n, t) = \arg[c_m(r_n, t)]$ increases or decreases monotonically, the mode indicates circular polarization. While, if the declination angle $\theta_m(r_n, t) = \arg[c_m(r_n, t)]$ is a constant value, the mode indicates linear polarization. Although eq. (3.30) shows the change in polarization state in the time domain, an analysis in the frequency imperative for investigating to investigate the characteristics of the mode structure. Therefore, the FRF coefficients are expressed by Fourier transform as in the following equation.

$$\begin{aligned} a_m(r_n, t) &= \sum \hat{a}_m(r_n, \omega)e^{i\omega t} + \sum \hat{a}_m^*(r_n, \omega)e^{-i\omega t}. \\ b_m(r_n, t) &= \sum \hat{b}_m(r_n, \omega)e^{i\omega t} + \sum \hat{b}_m^*(r_n, \omega)e^{-i\omega t}. \end{aligned} \tag{3.31}$$

Then, the complex coefficients in eq. (3.30) can be rewritten from eq. (3.31) in the

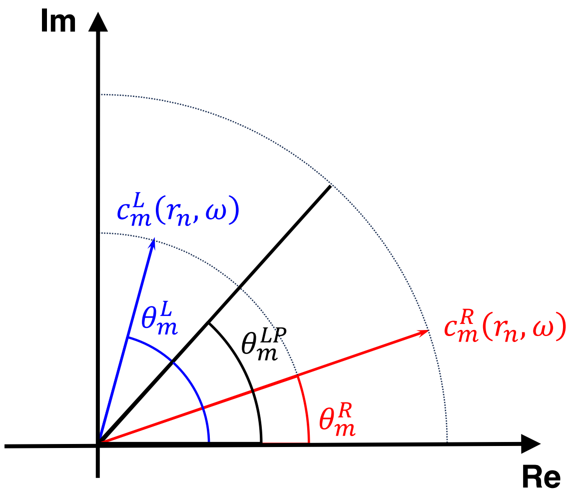

FIG. 3.3: Schematic diagram of the relationship between FRF complex coefficients $c_m^R(r_n,\omega)$ and polarization.

following equation.

$$\begin{aligned} c_m(r_n,t) &= \sum\left(\hat{a}_m(r_n,\omega)+i\hat{b}_m(r_n,\omega)\right)e^{i\omega t}+\sum\left(\hat{a}_m^*(r_n,\omega)+i\hat{b}_m^*(r_n,\omega)\right)e^{-i\omega t} \\ &= \sum c_m^L(r_n,\omega)e^{i\omega t}+\sum c_m^R(r_n,\omega)e^{-i\omega t} \\ &= \sum |c_m^L(r_n,\omega)|e^{\left(i\omega t+\theta_m^L(r_n)\right)}+\sum |c_m^R(r_n,\omega)|e^{-\left(i\omega t+\theta_m^R(r_n)\right)}. \end{aligned} \tag{3.32}$$

Where, $c_m^R(r_n,\omega)$ and $c_m^L(r_n,\omega)$ are as follows.

$$\begin{aligned} c_m^R(r_n,\omega) &= \hat{a}_m^*(r_n,\omega)+i\hat{b}_m^*(r_n,\omega). \\ c_m^L(r_n,\omega) &= \hat{a}_m(r_n,\omega)+i\hat{b}_m(r_n,\omega). \end{aligned} \tag{3.33}$$

In addition, $\theta_m^L(r_n)$ and $\theta_m^R(r_n)$ represent the declination angles of $c_m^L(r_n,\omega)$ and $c_m^R(r_n,\omega)$, respectively. Therefore, when $\omega>0$, $\left(i\omega t+\theta_m^L(r_n)\right)$ and $-\left(i\omega t+\theta_m^R(r_n)\right)$ in eq. (3.32) represent monotonically increasing and monotonically decreasing declination, respectively. In other words, eq. (3.33) represents the right- and left-rotating components of each mode structure with amplitudes $|c_m^R(r_n,\omega)|$ and $|c_m^L(r_n,\omega)|$ rotating at frequency ω. In addition, the polarization state of the mode structure can be examined from Eq. (3.33). For example, if the amplitudes of $c_m^R(r_n, \omega)$ and $c_m^L(r_n, \omega)$ are different, the spatial pattern represents a right- or left-handed rotational characteristic (or circular polarization). On the other hand, if the amplitudes of $c_m^R(r_n, \omega)$ and $c_m^L(r_n, \omega)$ are equal, the spatial pattern represents a standing wave (or linear polarization) oscillating with phase difference $\theta_m^{LP}(r_n) = \left(\theta_m^L(r_n) + \theta_m^R(r_n)\right)/2$ as shown in Fig.3.4. Here, since the characteristics of $c_m^L(r_n, \omega)$ and $c_m^R(r_n, \omega)$ are different for each time window under Fourier analysis, it is necessary to understand the average characteristics. Accordingly, with $\langle \cdots \rangle$ as the operator to ensemble average the time windows, the mode power of circular polarization can be determined by the difference between the power of right- and left-rotation, as shown below,

$$P_m^{CP}(r_n, \omega) = \left| |\langle c_m^L(r_n, \omega)\rangle|^2 \text{-} |\langle c_m^R(r_n, \omega)\rangle|^2 \right|. \tag{3.34}$$

The mode power of the linear polarization is expressed below using the coherence-like value $\gamma_m^{LP}(r_n, \omega)$ of the rotation coefficients $c_m^L(r_n, \omega)$ and $c_m^R(r_n, \omega)$.

$$P_m^{LP}(r_n, \omega) = \gamma_m^{LP}(r_n, \omega) \cdot 2\min[|\langle c_m^L(r_n, \omega)\rangle|^2, |\langle c_m^R(r_n, \omega)\rangle|^2]. \tag{3.35}$$

where $\gamma_m^{LP}(r_n, \omega)$ can be expressed as following equation.

$$\left(\gamma_m^{LP}(r_n, \omega)\right)^2 = \frac{|\langle c_m^L(r_n, \omega) c_m^R(r_n, \omega)\rangle|^2}{|\langle c_m^L(r_n, \omega)\rangle|^2 |\langle c_m^R(r_n, \omega)\rangle|^2}. \tag{3.36}$$

Also, *min*[...] represents the function that selects the minimum value. As shown above, the radial dependence of the polarization state of each mode structure can be directly examined from the two-dimensional image.

Chapter 4

Conditionally Averaging Technique for Nonlinear Oscillations

Plasma is a matter of strong nonlinearity, which causes the emergence of intermittent or short-lived structure, such as blobs [112] and streamers [13], and nonlinear oscillation including sawtooth oscillations [113, 114], fishbone instabilities [115], edge localized modes [116-118] and so on. The bursty events or the quasi-periodic phenomena observed commonly in linear and toroidal plasmas can be regarded as a combination of deterministic trend and probabilistic residual fluctuations in their development. In this chapter, the method for separating nonlinear oscillation into deterministic trend and residual fluctuation is discussed.

4.1 Conditional Average

The conditional average [119–124] is a technique to extract the typical waveform from such phenomena. For instance, using the conditional averaging method, quasi-coherent but probabilistic phenomena are divided into two parts as,

$$f(t) = f_{\mathrm{D}}(t) + f_{\mathrm{P}}(t), \tag{4.1}$$

where the function, $f(t)$, is the entire waveform showing quasi-periodic oscillations, and the first and second terms on the right-hand side, $f_D(t)$ and $f_P(t)$ are the deterministic trend and residual fluctuations, respectively. In the technique, the typical waveform is deduced as the average of the waveforms belonging to the ensemble of the identical events of the phenomenon. Then the problem is how to determine identical events or how to set appropriate conditions to choose the events. Such arbitrariness is often present in the conditional average method. Here, we describe the arbitrariness of conditional averaging methods using two examples of commonly used methods.

4.1.1 Threshold Method

The threshold method is widely applied to extract abrupt phenomena from nonlinear oscillatory phenomena. The steps of the method are quite simple and consist of three processes. First, a threshold value is set for the nonlinear oscillation of the target. Next, the timing of the peak value of the abrupt phenomena that exceeds the set threshold is recorded as the onset time of the fluctuation. Finally, each of the abrupt phenomena in the time window including the recorded timing is extracted as an ensemble and averaged to

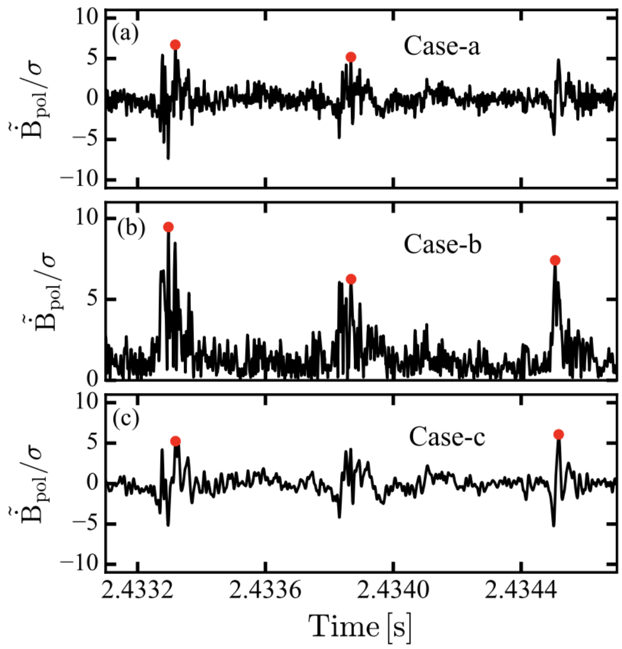

FIG. 4.1: Time series data of the magnetic field fluctuations measured with the Milnoff coil in ASDEX-U. These data represent (a) raw signal, (b) envelope of the raw signal, and (c) raw signal with low-pass 90 kHz applied, normalized by the respective standard deviation σ. Adapted from [124].

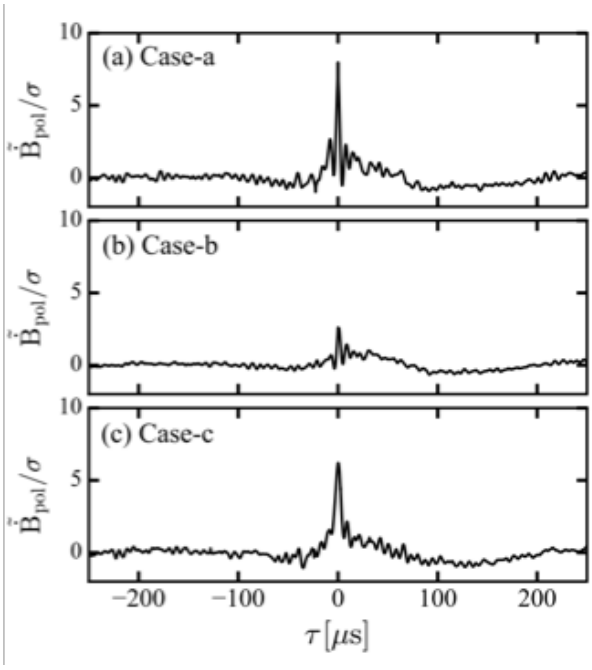

FIG. 4.2: Conditional averaging (a) raw signal, (b) envelope of the raw signal, and (c) raw signal with low-pass 90 kHz applied, normalized by the respective standard deviation σ. Adapted from [124].

extract a conditionally averaged waveform. As shown above, this method is effective as a simple tool for understanding the dynamics of abrupt phenomena, However, due to its simplicity, it contains a lot of arbitrariness. One of these is that the conditional averaged waveform varies depending on how the data is processed. The reason for this is that the waveform extracted as an ensemble is arbitrary because the timing of oscillation onset is determined by the "point" at which the peak value exceeds the threshold value. To explain the arbitrariness of the threshold method, an example is given in a study [124] in which conditionally averaged waveforms were extracted from abrupt phenomena of magnetic field fluctuations measured with the Milnoff coil in ASDEX-U. Figure 4.1 shows the time series data of the magnetic field fluctuations (a) raw signal, (b) envelope of the raw signal, and (c) raw signal with low-pass 90 kHz applied, normalized by the respective standard deviation σ. The point indicated by the red dot represents the timing of the peak that exceeds the threshold value. Here, the threshold value set is the standard deviation multiplied by 5, respectively. It can be seen that the timing of the onset of fluctuations, indicated by the red dots, is different in each time-series data. Therefore, it has been confirmed that differences appear in the conditionally averaged waveforms obtained as shown in Figs. 4.2(a)-(c). In order to eliminate such arbitrariness, a method named the "template method" was developed, in which the timing of the onset of oscillations is determined not by a "point" but by a "shape" and a conditionally averaged waveform is extracted. The details of the template method are explained in the following subsection.

4.1.2 Template Method

The template method, which was first applied to plasma physics in [123], can extract the deterministic trend from the quasi-deterministic waveform. The method is briefly reviewed as follows. The template method is composed of three steps. The first step is to assume an initial template waveform that owns the fundamental characteristics of the phenomenon. Then the correlation is calculated for every sampling time of the entire signal with the initial template waveform. The correlation between the template waveform and each cycle of the oscillation shows some local maxima, which indicate 'times of phase matching', $t_{c,\,i}$. As the second step, the conditional average is taken place according to the following formula,

$$f_{\mathrm{D}}(t) = \frac{\sum_{i=1}^{N} f\left(t + t_{c,\,i}\right)}{N},\ (-T/2 < t < T/2), \tag{4.2}$$

where T, $t_{c,i}$, and N are the oscillation period of the phenomenon, the i-th times of phase matching (or the correlation peaks), and the total number of identical events, respectively. Usually, the times of phase matching are obtained as the local peaks of the correlation

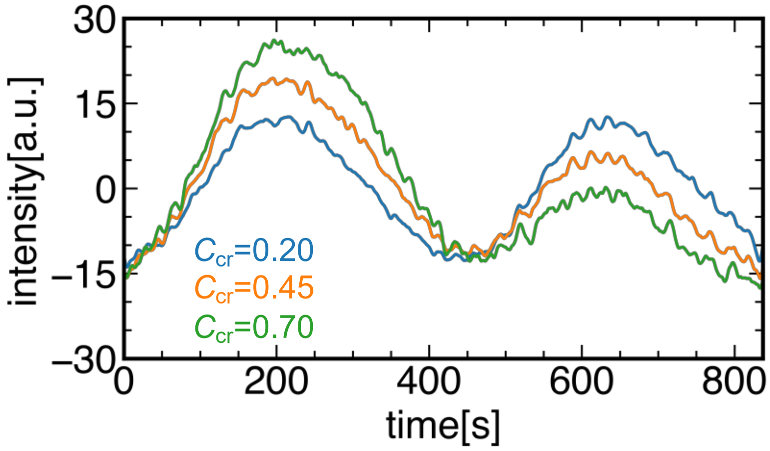

FIG. 4.3: Conditional averaged waveforms at different thresholds: C_{cr}=0.20 (blue line), C_{cr}=0.45 (orange line), C_{cr}=0.7 (Green line).

whose value should be more than a critical value, C_{cr}. As the third step, the obtained average waveform, $f_D(t)$, is regarded as the second template waveform, and the times of phase matching are recalculated to obtain the third template waveform. The above-mentioned process is repeated until the template waveform converges. The converged template waveform should be finally fixed as the deterministic trend of the phenomenon. Unlike the threshold method, which focuses on the "point" that exceeds the threshold in determining the timing of fluctuation onset, this method focuses on the "shape" of the phenomenon by setting a threshold for the correlation with the initial template waveform. Therefore, waveforms with similarity exceeding the set threshold can be extracted as an ensemble, eliminating arbitrariness such as different timing of oscillation onset depending on how the data is processed, as shown in Fig. 4.1. Hence, the template method is a conditional average method that eliminates the arbitrariness that existed in the threshold method. The arbitrariness in determining the oscillation onset time that existed in the threshold method has been resolved by the template method, but arbitrariness still exists in template method. In the template method, the setting of threshold values is empirical and consequently arbitrary. Figure 4.3 shows the conditionally averaged waveforms obtained by the template method at arbitrary threshold values (C_{cr}= 0.2, 0.45, 0.7). It can be seen that the obtained conditionally averaged waveforms are different for each threshold value. This is because the ensemble required for the conditionally averaging depends on the threshold value given to the correlation. The subsequent subsection describes the improved conditional average method, which eliminates this arbitrariness existing in the template method.

4.2 Correlation-Estimated Conditional Averaged Method

For the simple template method, a question should arise: how the critical correlation value, C_{cr}, should be determined, and how the obtained waveform should be dependent on the selection of the critical value. The method, Correlation-estimated conditional averaged method (CECAME) [125], is proposed to answer this question and to give a manner to choose the most appropriate critical correlation value, C_{cr}. The most appropriate critical correlation value should be determined in the optimization of the ensemble property in terms of both statistics and identity. Thus, the optimization parameter,

$$\xi(C_{cr}) = \frac{\sigma^2(C_{cr})}{N_{ens}(C_{cr})-1}, \tag{4.3}$$

is introduced, where $\sigma^2(C_{cr})$ and $N_{ens}(C_{cr})$ are the degree of the deviation from the deterministic trend, and the number of the ensemble, respectively. At the boundary of C_{cr} = 0, the optimization parameter should take a huge value due to the loss of the identity of the ensemble elements, while it is also large at the other boundary, C_{cr} = 1, where it loses

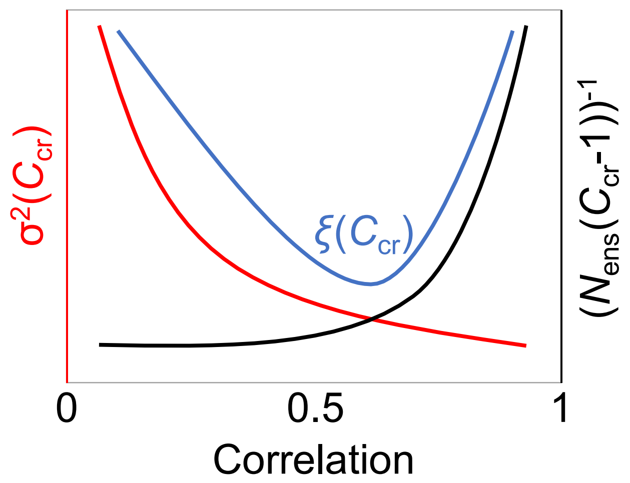

FIG. 4.4: Overview of the optimization parameter ξ in CECAME. Both axes represent uncertainty (red) and statistical properties (black), respectively.

the statistical significance due to the minimum number of elements, probably one. Accordingly, the dependences of $\sigma^2(C_{\mathrm{cr}})$ and $N_{\mathrm{ens}}(C_{\mathrm{cr}})$ on the critical correlation value are in conflict with each other as shown in Fig. 4.4. Therefore, the most appropriate critical correlation value C_{cr} should be in correspondence of the minimum of the optimization parameter.

On the other hand, a simple consideration gives an explicit relation between the critical correlation value, C_{cr}, and the power of the residual fluctuations (or deviation of the deterministic trend). According to the definition of eq. (4.1), these two quantities satisfy the following relation,

$$
\begin{aligned}
C_{\mathrm{cr}} &= \frac{f_{\mathrm{D}} \cdot (f_{\mathrm{D}} + f_{\mathrm{P}})}{\sqrt{f_{\mathrm{D}}^2 (f_{\mathrm{D}} + f_{\mathrm{P}})^2}} \\
&= \frac{f_{\mathrm{D}}^2}{\sqrt{f_{\mathrm{D}}^2 (f_{\mathrm{D}}^2 + f_{\mathrm{P}}^2)}}
\end{aligned}
$$

$$= \frac{1}{\sqrt{1+\frac{f_{\mathrm{P}}^2}{f_{\mathrm{D}}^2}}}, \tag{4.4}$$

where the dot product represents the inner products of the two functions as

$$p(t){\cdot}q(t) = \frac{1}{N}\sum_{i=1}^{N} p(t+t_i)q(t+t_i)\,, \tag{4.5}$$

and f_{D}^2 and f_{P}^2 represent the integrated powers of the deterministic trend and the residual fluctuations for the oscillation period. The relation is rewritten as

$$f_{\mathrm{P}}^2 = f_{\mathrm{D}}^2 \frac{1 - C_{\mathrm{cr}}^2}{C_{\mathrm{cr}}^2}. \tag{4.6}$$

Then, by setting $\sigma^2 = f_{\mathrm{P}}^2 / f_{\mathrm{D}}^2$, the optimization parameter, $\xi(C_{\mathrm{cr}})$, is

$$\begin{aligned}\xi(C_{\mathrm{cr}}) &= \frac{\sigma^2(C_{\mathrm{cr}})}{N_{\mathrm{ens}}(C_{\mathrm{cr}}) - 1} \\ &= \frac{1}{N_{\mathrm{ens}}(C_{\mathrm{cr}}) - 1}\left(\frac{f_{\mathrm{P}}^2}{f_{\mathrm{D}}^2}\right) \\ &= \frac{1 - C_{\mathrm{cr}}^2}{(N_{\mathrm{ens}}(C_{\mathrm{cr}}) - 1)C_{\mathrm{cr}}^2},\end{aligned} \tag{4.7}$$

where N_{ens} is the number of the ensemble element. Besides, by assuming that the integrated power of the residual fluctuations should be defined as the averaged deviation of the residual fluctuations,

$$f_{\mathrm{P}}^2 = \sum_{i=1}^{N_{\mathrm{ens}}} \left(f_i - f_{\mathrm{D}}\right)^2 / N_{\mathrm{ens}}(C_{\mathrm{cr}})\,. \tag{4.8}$$

We obtain,

$$\xi(C_{\mathrm{cr}}) = \frac{\sum_{i=1}^{N_{\mathrm{ens}}} \left(f_i - f_{\mathrm{D}}\right)^2}{N_{\mathrm{ens}}(C_{\mathrm{cr}})(N_{\mathrm{ens}}(C_{\mathrm{cr}}) - 1)f_{\mathrm{D}}^2}, \tag{4.9}$$

consequently, the optimization parameter, $\xi(C_{\mathrm{cr}})$, should have a minimum in the range of correlation from 0 to 1, and the most probable deterministic part should be obtained at the critical correlation value taken in correspondence of the minimum of $\xi(C_{\mathrm{cr}})$. At the critical correlation value, the most appropriate ensemble is that obtained for the conditional average. Finally, it is worth a mentioning that the expression of the optimization parameter, $\xi(C_{\mathrm{cr}})$, should correspond to the standard deviation of the averaged waveform (or the deterministic trend). Therefore, the minimum of the optimization parameter indicates the correlation value giving the minimum uncertainty to the deterministic trend. The results of the application of the CECAME to the spatial structure of solitary oscillation obtained by tomography measurements are described in Chapter 5.

Chapter 5

Quantification of Spatial Pattern Deformation

By development of tomography measurement, the spatial structure of the fluctuations over the entire plasma cross-section can now be measured, and new facts have been discovered. One of them is the plasma background asymmetry. Although the detailed conditions and dynamics of the excitation have not been clarified for the plasma background asymmetry, it is considered to be mainly due to the inhomogeneity of the heating input and particle source. In previous studies, background structure (e.g., steady-state density distribution) has been assumed azimuthal symmetry. However, nonlinear simulation result has recently suggested that in the presence of non-uniform particle sources (i.e., non-uniform density and temperature distributions in the azimuthal direction) in a linear plasma, nonlinear interactions with the drift wave can enhance the zonal flow. This can only mean that the plasma background asymmetry affects the structure formation of turbulence. Consequently, this chapter describes the results of an experimental investigation of the effect of the plasma background asymmetry on the spatial structure of nonlinear oscillations.

5.1 Plasma Stationary Structure Asymmetry

Conventional measurements using electrostatic probes are limited to localized plasma observation and cannot provide an accurate picture of the global steady-state structure of the plasma. Although it is possible to perform global measurement by increasing the

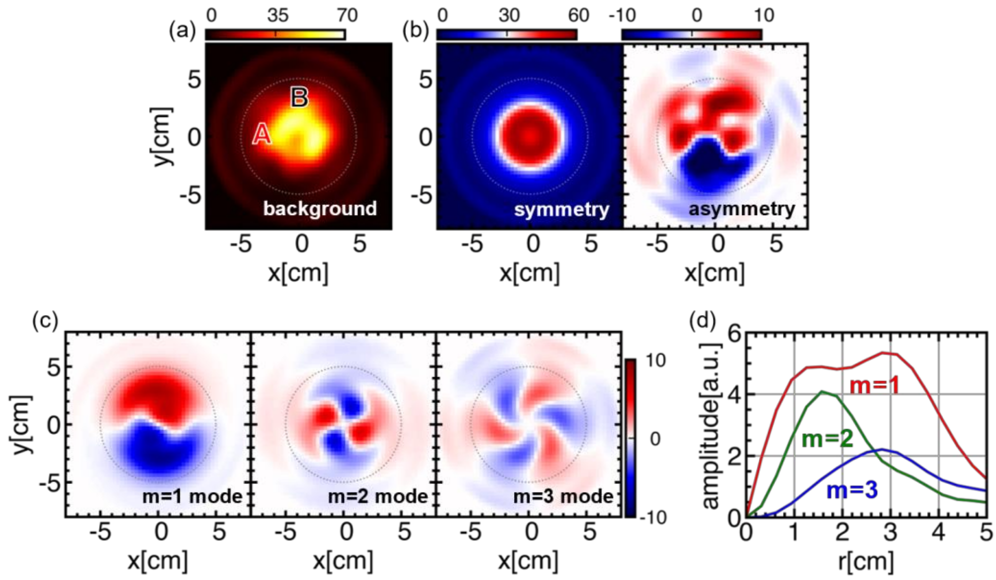

FIG. 5.1: (a) Steady-state emission distribution of the plasma (background structure). (b) Symmetric and asymmetric components of the background structure. (c) Azimuthal mode number m =1, 2, 3 structures in the background structure. (d) The radial profile of each mode amplitude.

number of measurement points of probes, it is not suitable for understanding the structure of the plasma because the cross-sectional area where the metal tips directly touch the plasma is larger, which may cause strong disturbances. Therefore, it has been assumed that the background structure of the plasma is spatially symmetric when measuring turbulence. In recent years, however, the development of global measurement systems has made it possible to measure the spatial distribution of plasmas in a non-contact manner. The spatial distribution of emission obtained from tomography can be decomposed as the following equation.

$$\varepsilon(r, \theta, t) = \langle \varepsilon(r, \theta, t) \rangle + \tilde{\varepsilon}(r, \theta, t). \tag{5.1}$$

Where $\langle \varepsilon(r, \theta, t) \rangle$ and $\tilde{\varepsilon}(r, \theta, t)$ represent the time-averaged and oscillating components, respectively, with the time-averaged component corresponding to the time-invariant structure called “background structure”. The background structure causes asymmetry in the spatial pattern, as shown in Fig. 5.1(a). Such asymmetry can be attributed to the inhomogeneity of plasma generators such as heating sources and particle sources. Then, how does the asymmetric component in the background structure have spatial structure? To investigate the structure in detail, the background structure was mode decomposed into symmetric ($m = 0$) and asymmetric ($m \neq 0$) components by using FB fitting as shown in the following equation.

$$\bar{\varepsilon}(r, \theta) = \bar{\varepsilon}_{\mathrm{S}}(r, \theta) + \bar{\varepsilon}_{\mathrm{A}}(r, \theta). \tag{5.2}$$

Where $\bar{\varepsilon}_{\mathrm{S}}(r, \theta)$ and $\bar{\varepsilon}_{\mathrm{A}}(r, \theta)$ represent the symmetric and asymmetric components of the background structure, respectively. The symmetric component has a hollow profile, while the asymmetric component has a complex structure in which the azimuthal mode number $m = 1$ is dominant. The intensity of the asymmetric component in the background structure is approximately 20 % of the total. Furthermore, by mode decomposition of the asymmetric component as shown in Figure 5.1(c), it is possible to reconstruct the spatial structure at each azimuthal modes. As shown in Fig. 5.1(d), the radial distribution of the amplitude of the background structure for each azimuthal modes shows that the $m = 1$structure is the most dominant, followed by the $m = 2$ and $m = 3$ structures. Moreover, the $m = 2$ structure has a relatively steep peak near the center of the plasma, while the $m = 3$ structure has a gentle peak on the outside of the plasma, and the amplitudes of each structure are inverted around $r \sim 2.5$ cm.

5.2 Solitary Oscillations

Solitary oscillation is a drift wave turbulence, which is a structure formed by the nonlinear coupling of the fundamental wave and its harmonics one after the other. Since the excited harmonics evolve at the same phase speed as the fundamental wave, they

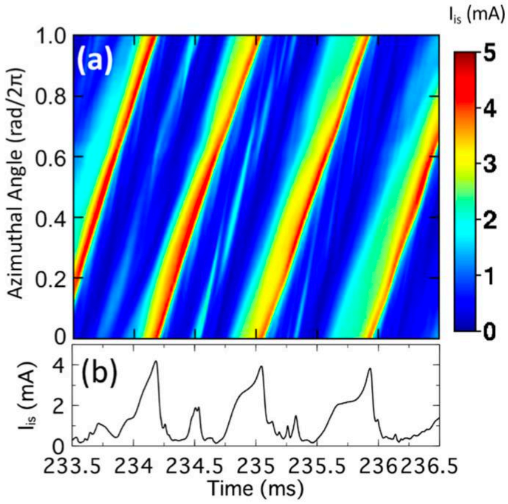

FIG. 5.2: (a) Spatio-temporal evolution of ion saturation currents measured with 64ch-probe. (b) Time evolution of ion saturation current at $\theta = 0$ on 64ch-probe. Adapted from [118].

propagate in the electron-diamagnetic direction with extremely distorted waveforms as shown in Fig. 5.2 [126-130]. It is also known that solitary oscillation is often accompanied by spatially localized structures named "solitary eddy" and "splash". It has been experimentally confirmed that the excitation and decay of solitary eddy and splash are synchronized with perturbations of the zonal flow, indicating that they interact dynamically with the zonal flow. In particular, although solitary eddy has only about 1/10 the energy of solitary oscillation, they have the same force to accelerate the azimuthal flow as solitary oscillation, and it has been confirmed that they efficiently transport energy to the zonal flow. From the above, it is important to understand the interaction of the three systems of solitary oscillation, solitary eddy, and zonal flow. However, studies that have investigated such interactions have been based on local measurements, and there are no examples of studies based on global measurements. Therefore, we first used a tomography system to understand the global dynamics of solitary oscillation, which is the key to the interaction between the three systems. In this study, the gas pressure was fixed at 2.16 mTorr, the magnetic field strength at 700 G, and the RF injection power at 3 kW,

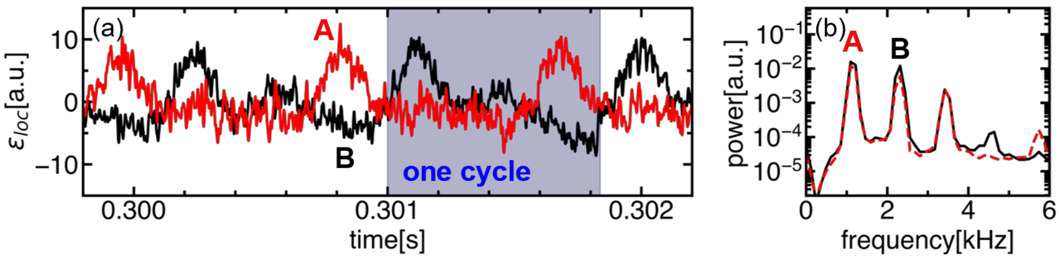

FIG. 5.3: (a) Temporal evolution of local emission. The red and black lines show the local positions in Fig.1(a) showing A (x = -3 cm, y = 0 cm) and B (x = 0 cm, y = 3 cm), respectively. (b) The frequency spectra of local emissions.

and experiments were performed in the parameter region where solitary oscillation excited.

Figure 5.3 shows the time evolution of the local emission and its frequency spectrum obtained from tomographic measurements. Each local position corresponds to A and B shown in Fig. 5.1(a). In Figure 5.3(a), the peak of the emission at (x, y) = (-3 cm, 0 cm) appears before the peak at (x, y) = (0 cm, 3 cm), which indicates that the observed target is rotating in the electron diamagnetic direction. Moreover, the frequency spectra at each local position show that the peaks exist at the fundamental frequency ($f \sim 1.2$ kHz) and its harmonic frequencies ($f \sim 1.2n$ kHz, $n = 1, 2, 3, \ldots$), confirming the characteristic of solitary oscillations. Figure 5.4 shows the time evolution of the spatial structure of the Fourier-Bessel fitted solitary oscillations. The two-dimensional image also shows that the emission peak propagates in the electron diamagnetic direction, while the structure is distorted irregularly with rotation. Since the waveforms in each period of nonlinear oscillation in the plasma are different, the spatial pattern is considered to be deformed in a complex manner during one period. To understand the dynamics of the structure from

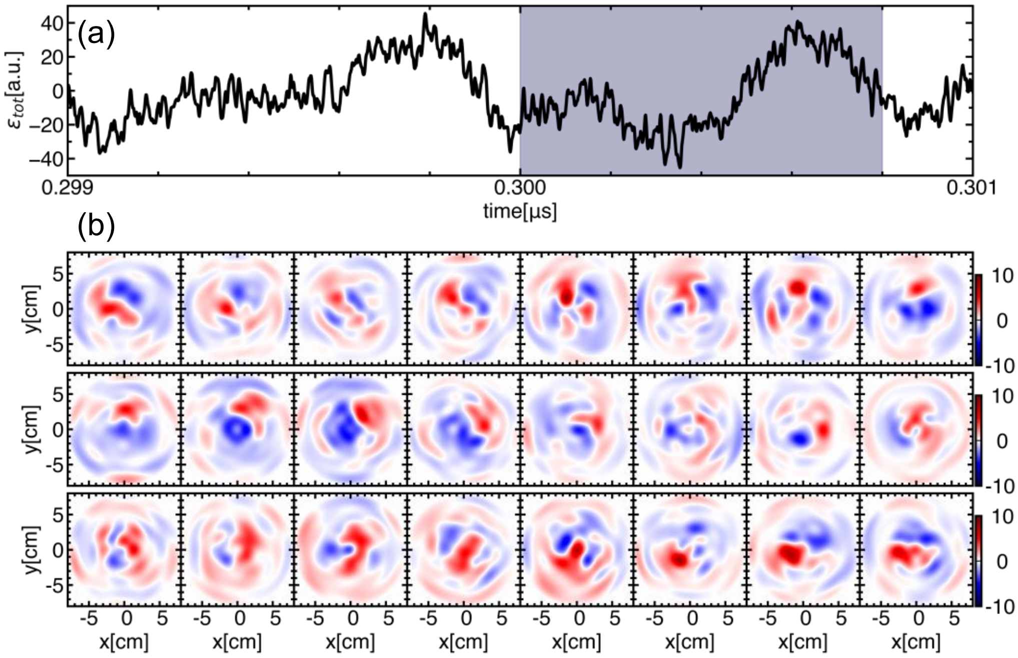

FIG. 5.4: (a) Time evolution of total emission. Here, total emission means the sum of local emissions in each grid of the tomography 2D image. (b) Temporal evolution of the spatial structure of the masking region at total emission, showing the spatial structure every 35 μs from top left to bottom right.

such a probable phenomenon, it is necessary to extract identical waveforms to perform ensemble averaging to separate the spatio-temporal (deterministic) evolution part from the stochastic part to observe the periodic spatial pattern rotation.

5.3 Separation of Deterministic Trend and Residual Fluctuation

The conditional average method is often used to separate the deterministic and probabilistic trend. In solitary oscillations observed by tomography, the oscillatory part $\tilde{\varepsilon}(r, \theta, t)$ in the second term of Eq. (5.1) can be separated into a deterministic part $\tilde{\varepsilon}_{\mathrm{D}}(r, \theta, t)$ and a probabilistic part $\tilde{\varepsilon}_{\mathrm{R}}(r, \theta, t)$ using the conditional averaged method.

The time evolution of the emission distribution obtained by the tomography shown in Eq. (5.1) can be rewritten as follows by also using Eq. (5.2).

$$\varepsilon(r, \theta, t) = \bar{\varepsilon}_{\mathrm{S}}(r, \theta) + \bar{\varepsilon}_{\mathrm{A}}(r, \theta) + \tilde{\varepsilon}_{\mathrm{D}}(r, \theta, t) + \tilde{\varepsilon}_{\mathrm{R}}(r, \theta, t). \tag{5.3}$$

Since the deterministic part $\tilde{\varepsilon}_{\mathrm{D}}(r, \theta, t)$ is the periodic rotation pattern of the ensemble averaged solitary oscillations, it should be rotationally symmetric if the solitary oscillations that excluded the probability. In this study, to investigate the time evolution of the deterministic part of the spatial pattern of solitary oscillations, a new conditional averaging method, CECAME, was applied to the time evolution of the spatial structure of solitary oscillations obtained by tomography measurements, and the deterministic part was separated from the probabilistic part.

This section first describes the results of applying CECAME to solitary oscillations and extracting the deterministic part. Then, the results of a statistical investigation of the nature of the separated stochastic part are presented.

5.3.1 Deterministic Trend of Solitary Oscillations

In extracting the deterministic trend, it is necessary to determine the onset timing of the oscillations that can be regarded as identical and extract the ensemble. First, CECAME is applied to the time series data of total emission as shown in Fig. 5.5(a) to determine the timing of the global onset of oscillation. The initial template is an arbitrary one-period waveform of the total emission. Figure 5.5(b) shows the time-series changes in the correlation values with the selected template waveform. It shows that the phase matching time is represented by the red dots. For each correlation value C_{cr}, the ensemble number N_{ens} is determined by aggregating the data at the phase matching time. Therefore, as shown in Fig. 5.6(a), when the correlation value C_{cr} is gradually increased from 0, it can

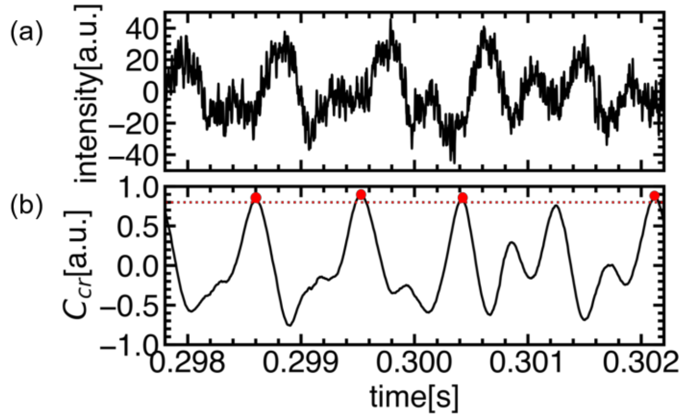

FIG. 5.5: (a) Temporal evolution of total emission. (b) The temporal evolution of the correlation between total emission and the initial template. The red points indicate the times of phase matching.

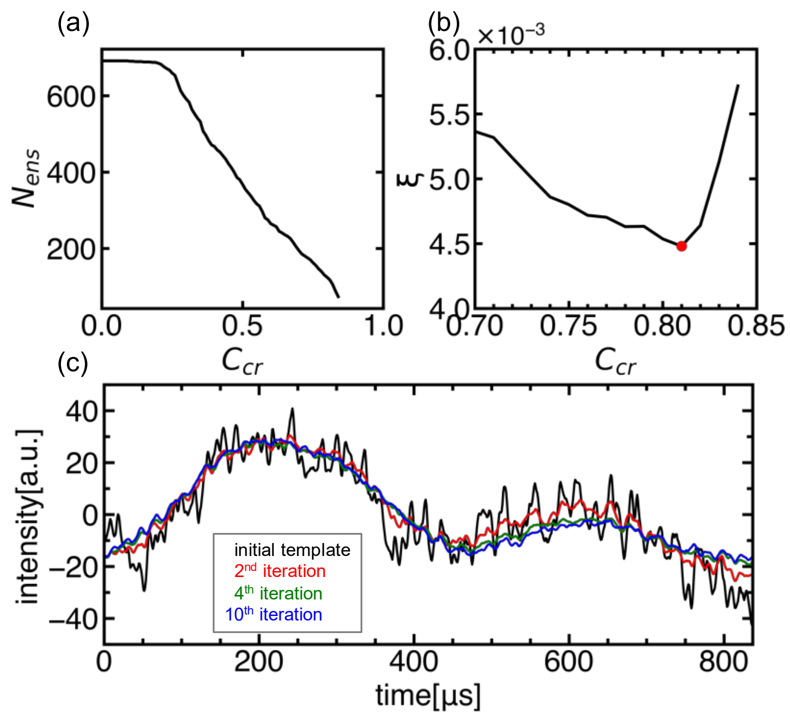

FIG.5.6: Change in (a) ensemble number and (b) optimization parameters with response to changes in correlation values. (c) Convergence of conditional averaged waveforms in the iteration number.

be confirmed that the ensemble number N_{ens} begins to monotonically decrease when $C_{\mathrm{cr}}\sim$ 0.3 exceeds, and eventually moves toward 0. Also, as mentioned in Chapter 4, as the correlation value is gradually increased, the uncertainty in the deterministic trend

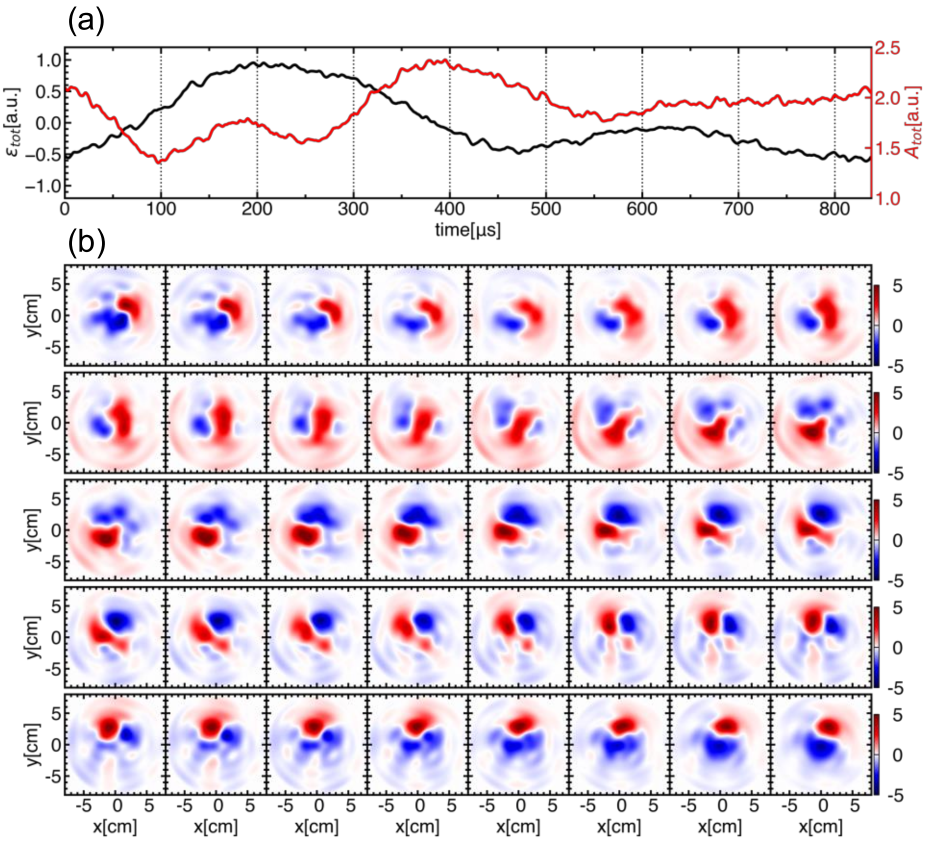

FIG. 5.7: (a) Temporal evolution of integrated deterministic trend (black line) and integrated amplitude of deterministic trend (red line). (b) Temporal evolution of the 2D structure of deterministic trend fitted with the Fourier-Bessel function series. Time slices are shown every 20 µsec from upper left to lower right.

decreases. Therefore, the optimization parameter ξ, which is composed of the uncertainty of the deterministic trend and the ensemble number, decreases as the correlation value C_{cr} increases, eventually reach a minimum value, and then begins to increase, as shown in Fig. 5.6(b). At this point, the correlation value at which the optimization parameter ξ takes the minimum value is the threshold of optimal correlation, which in this study was $C_{\mathrm{cr}} = 0.81$. Figure 5.6(c) shows the convergence of the template waveform at the correlation value $C_{\mathrm{cr}} = 0.81$. Here, the blue line shows the initial template waveform. It shows the change in the conditional averaging waveform at different iteration steps, indicating that the process converged well because the waveform did not change when the number of iterations exceeded 4. Thus, the proposed optimization method successfully extracts the most probable deterministic trend of the solitary oscillation in PANTA.

Next, the deterministic trend of the oscillatory waveform is extracted by acquiring and averaging the ensemble in each grid using the global phase matching time determined in the time series data of total emission. By reconstructing these deterministic trends, a two-dimensional structure of the most probable deterministic trend can be obtained, as shown in Fig. 5.7. On the other hand, it was also confirmed that the spatial pattern of the deterministic part is deformed with rotation and the symmetry is broken. Solitary oscillations observed by probe measurements have been used to understand the spatial structure in the plasma cross-section by targeting components that are highly correlated in the direction of the magnetic field lines. Therefore, the structure composed of the fundamental and its harmonics rotates in the electron-diamagnetic direction without deformation because the phase velocity is the same. In this paper, too, the deterministic trend is extracted by averaging the highly correlated waveforms as an ensemble using the conditional averaging method, so the spatial pattern is not expected to be deformed. Then, what is the cause of the deformation observed in the spatial pattern of the deterministic trend. One possible factor is the background structure asymmetry. If coherent structures such as solitary oscillations are a phenomenon in a cylindrical plasma that is strictly rotationally symmetric, then the deterministic pattern obtained by ensemble averaging should be rotationally symmetric. In addition to such an assumption, since it is known that the asymmetry of the distribution affects nonlinear oscillations and transport, it is necessary to investigate the relationship between the background structure asymmetry and the spatial pattern deformation of the deterministic trend.

5.3.2 Residual Fluctuation of Solitary Oscillations

What are the properties of the residual fluctuation shown in the third term of Eq. (5.2). If the residual fluctuation is purely random, its amplitude and power should be nearly constant regardless of the time variation of the deterministic trend. However, the deterministic trend should be related to quantitative changes in the plasma. For example, the plasma flow should affect structures such as the residual fluctuation on shorter spatio-temporal scales relative to the deterministic trend. Therefore, there should be a causal relationship between the deterministic and residual; fluctuations. To answer this question, we first need to evaluate the error in the amplitude of the residual fluctuation. The time evolution of the average power of the residual fluctuation, $P_{\tilde{\varepsilon}_\mathrm{R}}(t)$, can be statistically expressed as the following equation.

$$\begin{aligned} P_{\tilde{\varepsilon}_\mathrm{R}}(t) &= \mathrm{EA}\left[\tilde{\varepsilon}_\mathrm{R}{}^2(t)\right] \\ &= \frac{\sum_{i=1}^{N_\mathrm{ens}}\left(\tilde{\varepsilon}_{\mathrm{R},\,i}{}^2(t)\right)}{N_\mathrm{ens}} \\ &= \frac{\sum_{i=1}^{N_\mathrm{ens}}\left(\tilde{\varepsilon}_i(t) - \tilde{\varepsilon}_\mathrm{D}(t)\right)^2}{N_\mathrm{ens}}. \end{aligned} \tag{5.4}$$

Where EA[...] represents the ensemble mean. Using Eq. (5.3), the variance of the mean power $P_{\tilde{\varepsilon}_\mathrm{R}}(t)$ of the residual fluctuation can be defined as follows.

$$\begin{aligned} \left|\Delta P_{\tilde{\varepsilon}_\mathrm{R}}(t)\right|^2 &= \mathrm{EA}\left[\left(\tilde{\varepsilon}_{\mathrm{R},i}{}^2(t) - P_{\tilde{\varepsilon}_\mathrm{R}}(t)\right)^2\right] \\ &= \frac{\sum_{i=1}^{N_\mathrm{ens}}\left(\tilde{\varepsilon}_{\mathrm{R},i}{}^2(t) - P_{\tilde{\varepsilon}_\mathrm{R}}(t)\right)^2}{N_\mathrm{ens}} \\ &= \mathrm{EA}\left[\tilde{\varepsilon}_\mathrm{R}{}^4(t)\right] - P_{\tilde{\varepsilon}_\mathrm{R}}(t). \end{aligned} \tag{5.5}$$

From the above, the following relationship holds for the average amplitude of the residual fluctuation and its error.

$$|\tilde{\varepsilon}_{\mathrm{R}}(t)| \pm |\Delta\tilde{\varepsilon}_{\mathrm{R}}(t)| = \sqrt{P_{\tilde{\varepsilon}_{\mathrm{R}}}(t) \pm \Delta P_{\tilde{\varepsilon}_{\mathrm{R}}}(t)}$$
$$\cong \sqrt{P_{\tilde{\varepsilon}_{\mathrm{R}}}(t)}\left(1 \pm \frac{1}{2}\left(\frac{\Delta P_{\tilde{\varepsilon}_{\mathrm{R}}}(t)}{P_{\tilde{\varepsilon}_{\mathrm{R}}}(t)}\right)\right). \tag{5.6}$$

Thus, the error in the mean amplitude of the residual fluctuation can be defined as follows.

$$|\Delta\tilde{\varepsilon}_{\mathrm{R}}(t)| = \frac{\sqrt{P_{\tilde{\varepsilon}_{\mathrm{R}}}(t)}}{2}\left(\frac{\Delta P_{\tilde{\varepsilon}_{\mathrm{R}}}(t)}{P_{\tilde{\varepsilon}_{\mathrm{R}}}(t)}\right). \tag{5.7}$$

Figure 5.8 shows the time evolution of the average amplitude of the residual fluctuation of the total and local emission at (x, y) = (0 cm, 3 cm), along with the error bars defined by Eq. (5.6). In figure 5.8(b) the variation of the residual fluctuations of the total emission amplitude should have a large variation beyond error bar; the later part of the variation should be larger than that of earlier phase (for example, the difference in the fluctuation powers is larger beyond the error at the times shown by the black arrows, $t = 429\ \mu s$ and $t = 485\ \mu s$), and the deviation is beyond the error bars. This indicate that the difference of residual fluctuation is not a simple random component and should have a physical reality due to the asymmetry of the plasma background structure, changes in the deterministic trend (e.g., creation of distortion structures), and nonlinear interactions among the respective components.

Also, in figure 5.8(c), the comparison shows that the local residual fluctuations should change in a synchronized manner with the deterministic trend, since the amplitude variation is beyond the errors; note that the error bars are plotted but too small to be seen. The change of the residual fluctuations should become more visible in the local observation than in the global one, since the local fluctuations may be smoothed out in

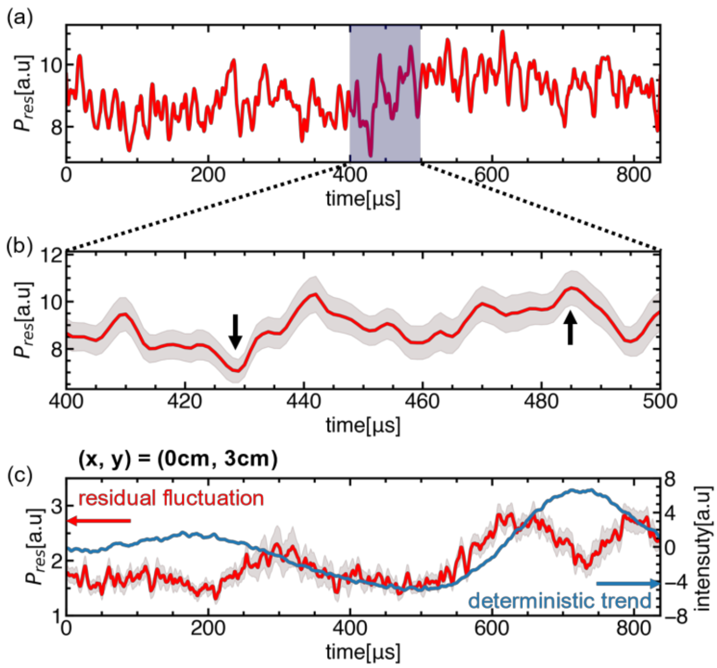

FIG. 5.8: (a) The amplitude of the residual fluctuations of total emission. (b) An expanded view of the residual fluctuations of total emission for the time range of 400–500μs. (c) The amplitude of residual fluctuations of local emission for the position at (x, y) = (0 cm, 3 cm). The evaluated errors, $|\Delta f_P(t)|$, of the residual fluctuations, plotted by red masking region, are quite small. The blue line is the deterministic trend at the same position.

the total emission. It should be left as a future work to investigate the detailed relationship between the deterministic trend and the residual fluctuations: we research the mutual interaction between the smaller scales of fluctuations and background plasma.

5.4 Modal Decomposition of Deterministic Trend

In section 5.3, it is revealed that the deterministic pattern of solitary oscillations extracted using CECAME shows symmetry breaking and pattern deformation with rotation. Although the deterministic pattern is not expected to be deformed in cylindrical plasmas assuming strict rotational symmetry, tomographic measurements confirm the existence of a significant asymmetric component in the background structure of the plasma. The nonlinear effect of such background asymmetry should possibly cause the deformation of the deterministic pattern.

In this section, based on the above assumptions, FBF and FRF expansions are applied to the time evolution of the deterministic pattern of solitary oscillations, and mode structure analysis and Fourier analysis are performed to decompose the modes in terms of the azimuthal mode number m and frequency ω, respectively. The deformation of the deterministic pattern is quantified by evaluating the mode power and the modal polarization from the respective coefficients obtained from the mode decomposition.

5.4.1 Qualitative Understanding of Spatial Pattern Dynamics

To analyze two-dimensional images obtained by tomographic measurements, analyses using FBF and FRF expansions have been developed. In this study, to identify the factors causing the deformation of the deterministic pattern of solitary oscillations, a global analysis using FBF expansion and a local analysis using FRF expansion are performed to investigate the inherent properties in the pattern. First, mode decomposition is performed using FBF expansion to identify the azimuthal mode number m inherent in the deterministic pattern. Figure 5.9 shows the time evolution of the integrated deterministic pattern ε_{int} and its amplitude A_{int} and the mode decomposition of the spatial structure

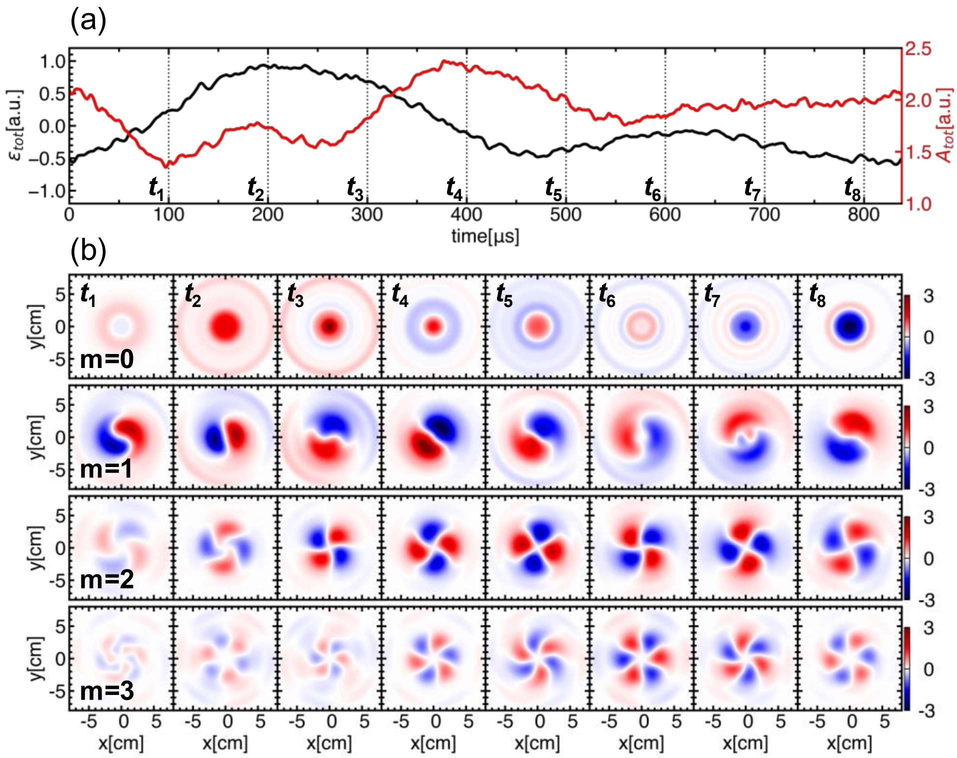

FIG. 5.9: (a) Temporal evolution of integrated deterministic trend (black line) and integrated amplitude of deterministic trend (red line). (b) Temporal evolution of the 2D structure of deterministic trend.

of the deterministic pattern to m = 0~3, respectively. Here, the integrated emission ε_{int} and amplitude A_{int} are defined as $\int \tilde{\varepsilon}_{\mathrm{d}}(r, \theta, t) r dr d\theta$ and $\sqrt{\int \tilde{\varepsilon}_{\mathrm{d}}^2(r, \theta, t) r dr d\theta}$, respectively. The m = 0 structure shown in Fig. 5.9(b) shows that the symmetric structure fluctuates like a longitudinal wave. This fluctuation is stronger inside the plasma and weaker outside the plasma at r ~ 3.0 cm, which indicates that the structure has a steep peak at the center of the plasma. Moreover, the amplitude changes show one positive amplitude region (shown in red) and one negative amplitude region (shown in blue) appearing alternately, and it is confirmed that the fundamental frequency at $f = 1\omega$ ($\omega \sim 1.2$ kHz) is dominant. On the other hand, the m = 1 structure is observed to rotate with deformation in the electron diamagnetic direction once during one cycle of the pattern. If the m = 1 structure consists only of the fundamental frequency, there should be no deformation of the pattern in this rotation. The m = 2 structure is observed to rotate at the same phase speed as the m = 1 structure, without a single rotation of the pattern during one cycle. This is a typical feature of solitary oscillations. Moreover, since the typical pattern of the second harmonic rotates relatively undeformed, it is considered that the different frequency components included in the m = 2 structure are fewer than those in the m = 1 structure. On the other hand, the m = 3 structure shows a complex deformation of the pattern. Especially in the first to third images in Fig. 5.9(b), the pattern orientation alternates and the amplitude becomes stronger toward the latter half of the cycle. This suggests that the m = 3 structure, which has a different frequency from the third harmonic, is dominant.

These results suggest that the deformation of the deterministic patterns of solitary oscillations is due to the complex deformation of each mode structure. It is also suggested that the pattern deformation in each mode structure is caused by a contamination of modes which have the same azimuthal mode but different frequencies from the harmonics (non-harmonic modes with different phase velocities from the harmonics).

5.4.2 Global Spatial Pattern Analysis with FBF

In the previous subsection, it was qualitatively shown from the 2D images that the observed solitary oscillations are contaminated with non-harmonic modes, resulting in a deterministic pattern deformation. However, the frequency components in each mode structure have not yet been identified, so it is necessary to analyze the mode structure and Fourier analysis to decompose them into azimuthal mode number and frequency and identify the dominant mode. Moreover, to clarify the mechanism of pattern deformation, it is necessary to investigate the process by which the non-harmonic modes emerge. Therefore, in this subsection, the results of the investigation of global properties in the deformation of deterministic patterns by making full use of FBF expansions are described.

As mentioned in section 3.2, FBF expansion uses a radially continuous function to expand the image, allowing for the study of global changes in spatial structure. Consequently, by performing mode decomposition on the deterministic pattern, the manner of deformation can be evaluated as an azimuthal mode vector $\overrightarrow{M}(t) = (A_m(t), B_m(t))$, whose elements are calculated from the 2D images as follows,

$$A_m(t) = \frac{1}{\sqrt{\pi}} \int \tilde{\varepsilon}(r, \theta, t) \cos(m\theta)\, rdrd\theta,$$
$$B_m(t) = \frac{1}{\sqrt{\pi}} \int \tilde{\varepsilon}(r, \theta, t) \sin(m\theta)\, rdrd\theta. \tag{5.8}$$

Note that the absolute value and phase of the modal vector represents the amplitude and location of each mode structure. Figure 5.10(a, b) also shows the temporal evolution of the vector elements, and their Lissajous trajectories. The amplitude of each azimuthal mode is found to vary during the cycle, and the corresponding Lissajous trajectories are found to deform from circles that would be expected if a mode simply rotated without deformation. This deviation of the Lissajous trajectory from a circle is ascribed to

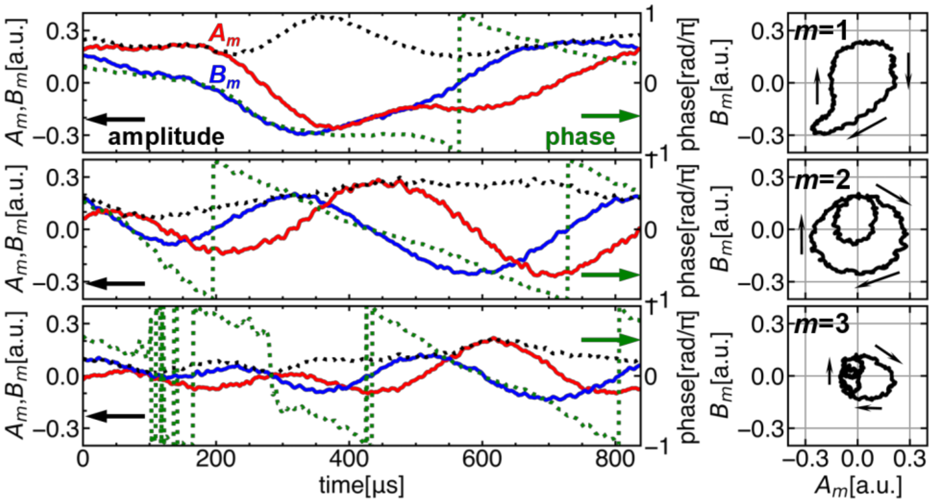

Fig. 5.10: (a) The temporal evolution of the moment vector elements A_{m} and B_{m} of azimuthal modes (red and blue line) and its amplitude (black dotted line) and phase (green dotted line). (b) Lissajous trajectories of moment vector elements A_{m} and B_{m}.

emergence of backward propagating harmonic and/or non-harmonic frequency modes which result in different phase velocities from harmonic one.

Focusing on each mode structure, the vector element of the m = 1 structure changes only once during one cycle, and the phase change shown by the green dotted line also confirms that the structure rotates only once during one cycle, indicating that the m = 1 harmonic mode is dominant. On the other hand, it is quantitatively expressed that multiple backward propagating modes and/or non-harmonic modes are included, since the amplitude and phase do not vary monotonically. This is evident from the distorted shape of the Lissajous trajectory shown in Fig. 5.10(b) compared to the other mode structures. The vector elements of the m = 2 structure also show two rotations of the structure from the time evolution of the phase, confirming that the m = 2 harmonic mode is dominant. The time evolution of amplitude and phase is also monotonous compared to the m = 1 structure, and the Lissajous trajectory has a characteristic trajectory of two circles or ellipses, which indicates that the m = 2 structure does not contain backward propagating modes and/or non-harmonic modes as much as the $m = 1$ structure. On the other hand, the $m = 3$ structure is observed to have multiple phase wraps in the first half of the period, which suggests that the direction of rotation is changing minutely. This suggests that stronger backward propagating modes are contaminated in the structure compared to the other mode structures.

In summary, it is demonstrated that the modulation of amplitude and deviation of the Lissajous trajectory from the circle in each mode structure can be explained by the emergence of backward propagating harmonics and/or non-harmonic modes that have different phase velocities to the harmonics. Consequently, the deformation can be further quantified by evaluating the power and polarization characteristics of each mode. Here, the concept of "*polarization*" is used in analogy of electromagnetic field polarization of light in optics. In the following, deformation degree and polarization properties of the deterministic pattern, quantified by evaluating the power and polarization properties of each mode, are described.

Distinction between right- (electron diamagnetic) and left-handed (ion diamagnetic) rotation is made using the following Fourier transformation,

$$A_{\pm}(m, n\omega) = \frac{1}{\sqrt{\pi T}} \int \tilde{\varepsilon}(r, \theta, t) \cos(m\theta \pm n\omega t)\, rdrd\theta dt,$$
$$B_{\pm}(m, n\omega) = \frac{1}{\sqrt{\pi T}} \int \tilde{\varepsilon}(r, \theta, t) \sin(m\theta \pm n\omega t)\, rdrd\theta dt, \qquad (5.9)$$

where $\tilde{\varepsilon}(r, \theta, t)$ is the FBF expanded deterministic pattern, and A_+, B_+, A_- and B_- represent the coefficients of right- and left-hand rotation, respectively, and the respective power can be expressed as $P_i(m, n\omega) = A_i^2 + B_i^2$ ($i = +, -$). Fig. 5.11(a) shows 2D map of the modal power $P_i(m, n\omega)$ obtained from the above transformation resolved by frequency $n\omega$ and azimuthal mode number m. The $m = 1$ structure is found to be dominated by the harmonic mode power, $P_+(1, 1\omega)$, while $P_-(1, 1\omega)$, $P_-(1, 2\omega)$, and

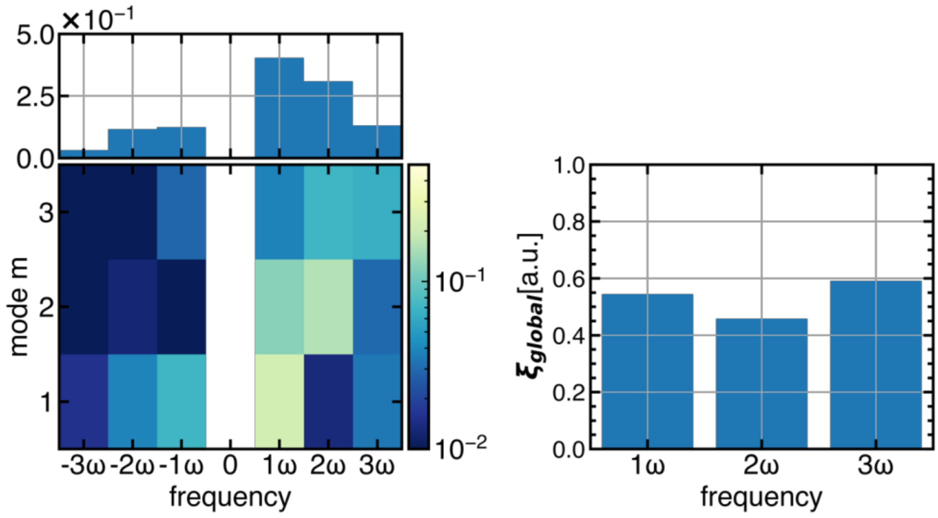

Fig. 5.11: (a) Modal power obtained using the FBF, and integrated modal power in terms of frequency (top). (b) The degree of deformation parameter ξ as a function of frequency.

$P_{+}(1, 3\omega)$ are also dominant. The $m = 2$ structure is found to be dominated by harmonic and non-harmonic modes of right-handed rotation, while the influence of modes of backward propagating modes is found to be small. The $m = 3$ structure has $P_{+}(3, 1\omega)$ and $P_{-}(3, 1\omega)$ of about comparable, which indicates that the influence of the backward propagating modes is significant compared to the other mode structures. Moreover, since $P_{+}(3, 3\omega)$ and $P_{+}(3, 2\omega)$ are present in almost the same order, it is considered that the deterministic pattern and phase changes in the $m = 3$ structure is occurred as shown in Fig. 5.9(b) and 5.10. Then, using the defined mode power, the degree of the spatial pattern deformation of M-th harmonics is evaluated by a deformation parameter ξ, defined below,

$$\xi(M) = \frac{\sum_m P(m, M\omega) - P(M, M\omega)}{P(M)}. \tag{5.10}$$

where $P(M) = \sum_m P(m, M\omega)$. The parameter indicates the non-harmonic mode contribution to the deformation of the M-th harmonic mode.

On the other hand, emergence of backward propagating mode ($n < 0$) also changes the

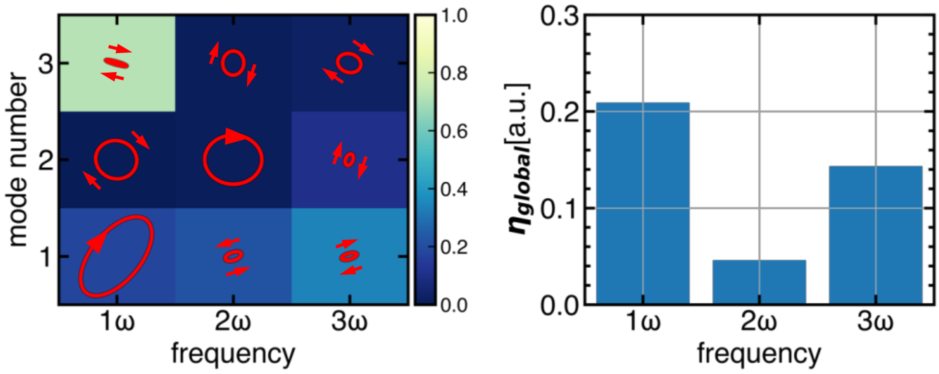

Fig. 5.12: (a) The polarization parameter γ for each mode with the corresponding Lissajous trajectories (or polarization pattern). (b) The degree of linear polarization contamination η as a function of frequency.

modal polarization property or causes the deformation of the Lissajous trajectories. In optics, when circular polarization rotating in different directions is added together, a linear polarization component is produced. This linear polarization component is contaminated with the circular polarization to produce elliptical polarization. In other words, if ellipticalization is generated, it means that the contribution of the backward propagating modes is large. From the above, by investigating the ratio of the linear polarization component of each mode, it is possible to evaluate how each pattern is deformed by the backward propagating modes. A modal polarization parameter to indicate the linear polarization property, γ, is introduced as,

$$\gamma(m, M > 0) = \frac{P_{\mathrm{Linear}}(m, M\omega)}{P_{\mathrm{Circular}}(m, M\omega) + P_{\mathrm{Linear}}(m, M\omega)}. \tag{5.11}$$

where, $P_{\mathrm{Linear}}(m, M\omega) = 2\min(P_{+}, P_{-})$ and $P_{\mathrm{Circular}}(m, M\omega) = P_{+} + P_{-} - P_{\mathrm{Linear}}$. The parameter γ for each mode obtained by Eq. 5.11 is shown in Fig. 5.12(a). The Lissajous trajectories corresponding to each mode are also displayed in the figure. The Lissajous trajectory becomes more elliptical as the parameter, γ, becomes larger. On the other hand, as shown in $\gamma(1,2)$, the direction of rotation of the Lissajous trajectory is left-handed, which confirms the superiority of the backward propagating mode. Moreover, an index η, which represents the degree of linear polarization contamination, is defined as a function of frequency as follows,

$$\eta(M) = \frac{\sum_m P_{\pm}(m, M\omega)\gamma(m, M\omega)}{P(M)}. \tag{5.12}$$

where $P_{\pm}(m, M\omega) = P(m, \text{-}M\omega) + P(m, M\omega)$. Figure 5.12(b) shows the ratio of linear polarization in the mode at each frequency evaluated from equation (5.12). Comparing the pattern deformation degree ξ and the degree of linear polarization contamination η, it is found that the degree of contamination is small relative to the degree of deformation in $\xi(2)$ and $\eta(2)$. This is considered that the dominant rotational mode is clear, unlike the other frequency components. Moreover, the total deformation ξ_{tot} and polarization η_{tot} index are 0.525 and 0.146, respectively, whose defined as,

$$\xi_{\text{tot}} = \frac{\sum_M \xi(M)P(M)}{\sum_M P(M)},\ \eta_{\text{tot}} = \frac{\sum_M \eta(M)P(M)}{\sum_M P(M)}. \tag{5.13}$$

The analyses show that the deformation of the solitary oscillations is quantified by the contamination of non-harmonic azimuthal modes, which cause amplitude and phase modulation to the original harmonic oscillations, as well as modifying the modal polarization characteristics in the Lissajous trajectories.

Figure 5.13 shows an example to clarify the deformation process by non-harmonic modes. The circular trajectory shown in Fig. 5.13(c-I) is an original harmonic mode which is deformed into an elliptical trajectory as shown in Fig. 5.13(c-II) by the emergence of the counter- propagating modes or contamination of the linear polarization. Then, the emergence of non-harmonic modes of 2ω or 3ω one by one, deforms the elliptical trajectory is further to the trajectories shown in Fig. 5.13(c-III) and (c-IV), finally

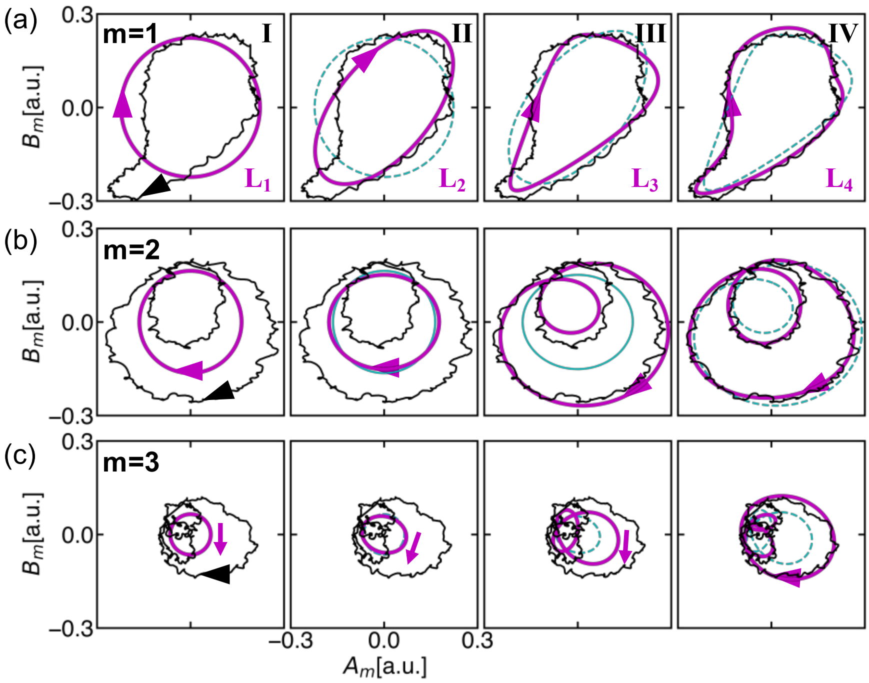

Fig. 5.13: An example of the deformation process of the m = 1, 2, and 3 modes. I) The circular Lissajous trajectory corresponds to the original harmonic mode, L_1, (magenta) and is shown with experimental data (black). II) The deformed trajectory by superposition of counter-propagating modes of the fundamental frequency, L_2, (magenta) with the trajectory of the previous step (dashed cyan) for the reference. III) and IV) Further superposition of non-harmonic modes of 2ω and 3ω one by one, deforms the elliptical trajectory L_2 to the ones, L_3 and L_4. The final one is almost identical to the experimental data.

resulting in a trajectory that is almost identical to the experimental data.

5.4.2 Local Spatial Pattern Analysis with FRF

As mentioned in section 3.3, since FRF expansion discretely expands the image using a rectangular function in the radial direction, it is possible to discuss the deformation of the oscillation pattern in the band at each radial position. Consequently, for the deterministic pattern reconstructed using FRF expansion, we defined the azimuthal mode vector $\vec{m}(r_n, t) = (a_m(r_n, t), b_m(r_n, t))$ at each radial position by performing the mode decomposition as shown below,

$$a_m(r_n, t) = \frac{1}{\sqrt{\pi}} \int \tilde{\varepsilon}(r_n, \theta, t) \cos(m\theta)\, r d\theta,$$
$$b_m(r_n, t) = \frac{1}{\sqrt{\pi}} \int \tilde{\varepsilon}(r_n, \theta, t) \sin(m\theta)\, r d\theta. \tag{5.14}$$

Figure 5.14(a, b) shows the time evolution of the elements of the mode vector and their Lissajous trajectories in the r_n = 1.8 cm band. It is observed that the amplitudes of the $m = 1$ and $m = 2$ structures are heavily modulated and the Lissajous trajectories are deformed accordingly. On the other hand, the amplitude of the $m = 3$ structure modulates relatively weakly, but the Lissajous trajectory is confirmed to be distorted and elliptical. In addition, the phase changes in the opposite direction from the other modes around $t = 100$ μs, and the phase changes are not periodic. The $m = 3$ structure is expected to have a larger ratio of contaminated backward propagating modes compared to the other mode structures. The same analysis is also applied to the r_n = 2.5 cm band, and the results are shown in Fig. 5.14(c, d). Although the trends of mode vectors and Lissajous trajectories are similar, the time evolution of amplitude and deformation of Lissajous trajectory are more gradual compared to the r_n = 1.8 cm band. This suggests that the backward propagating and non-harmonic modes contaminated in the r_n = 2.5 cm band are fewer than those in the r_n = 1.8 cm band.

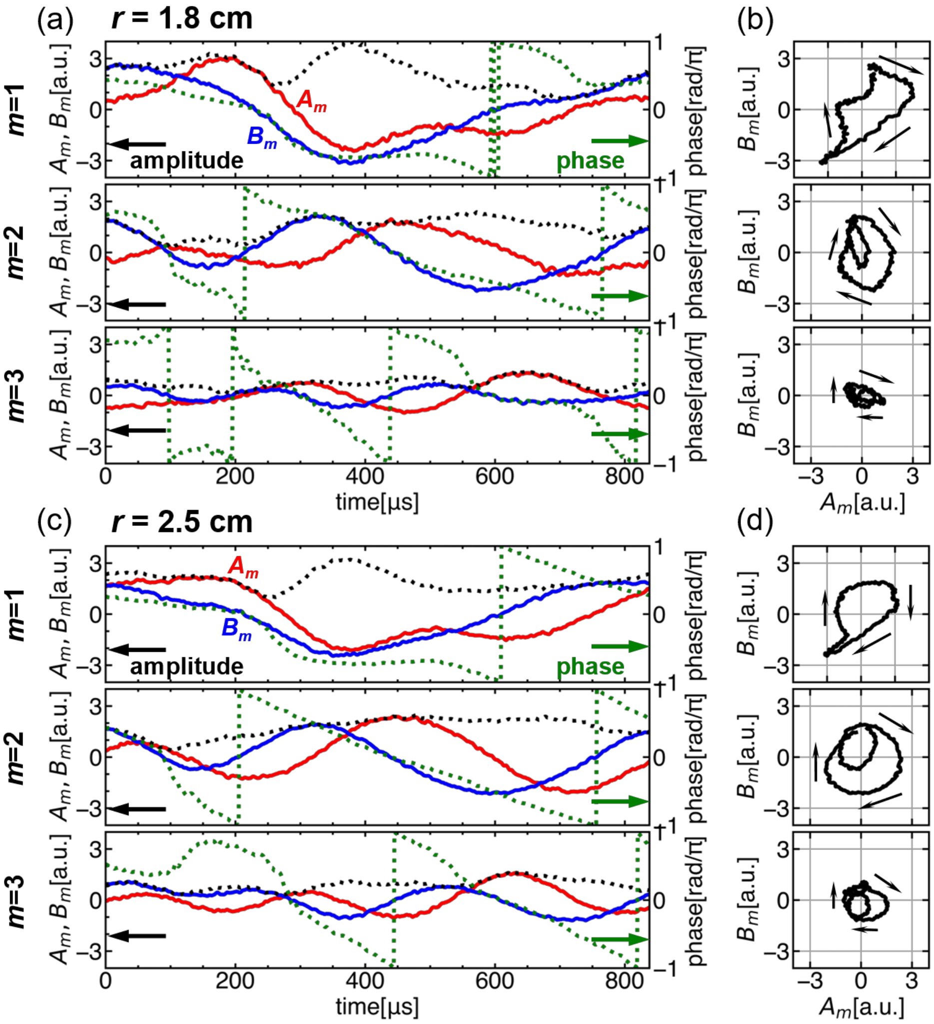

Fig. 5.14: The temporal evolution of the moment vector elements a_m and b_m of azimuthal mode (red and blue line) and its amplitude (black dotted line) and phase (green dotted line) at different radial position. (a, b) $r \sim 1.8$ cm and (c, d) $r \sim 2.5$ cm.

By performing the same analysis as in Section 5.4.2 on the deterministic pattern reconstructed using the FRF expansion, the degree of pattern deformation and the degree of linear polarization contamination can be evaluated for each radial position. In each mode structure and radial position, distinction between right- (electron diamagnetic) and left-handed (ion diamagnetic) rotation is made using the following Fourier transformation,

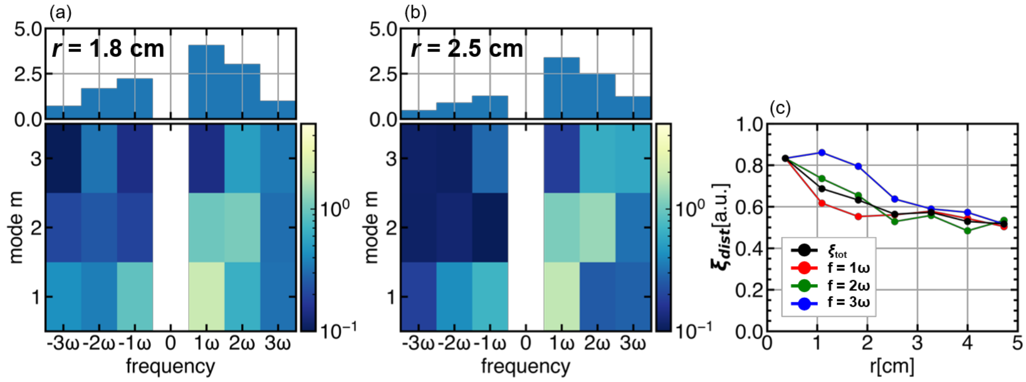

Fig. 5.15: (a, b) Modal power at $r \sim 1.8$ cm and $r \sim 2.5$ cm obtained using the FRF, and integrated modal power in terms of frequency (top). (c) The radial profile of the degree of deformation parameter ξ of each frequency. Black solid line represents the total deformation parameter ξ_{tot}.

$$a_{\pm}(r_n, m, n\omega) = \frac{1}{\sqrt{\pi T}} \int \tilde{\varepsilon}(r_n, \theta, t) \cos(m\theta \pm n\omega t)\, r d\theta dt,$$

$$b_{\pm}(r_n, m, n\omega) = \frac{1}{\sqrt{\pi T}} \int \tilde{\varepsilon}(r_n, \theta, t) \sin(m\theta \pm n\omega t)\, r d\theta dt, \tag{5.15}$$

where $\tilde{\varepsilon}(r_n, \theta, t)$ is the FRF expanded deterministic pattern. As in the global analysis, a_+, b_+, a_- and b_- represent the coefficients of right- and left-hand rotation, respectively, and the respective power can be expressed as $p_i(r_n, m, n\omega) = a_i^2 + b_i^2$ $(i = +, -)$. Figure 5.15(a, b) shows 2D maps of the mode power resolved in azimuthal mode number m and frequency $n\omega$ at r_n = 1.8 cm and r_n = 2.5 cm. Although it is clear from the integrated mode power in the azimuthal mode shown in the upper panel of the figure that the trends are similar at each radial position, some mode powers show different trends in each mode power. For example, at r_n = 1.8 cm, $p_-(1.8, 1, 2\omega) < p_+(1.8, 1, 2\omega)$, right-handed rotation power is dominant, while at r_n = 2.5 cm, $p_-(2.5, 1, 2\omega) > p_+(2.5, 1, 2\omega)$, left-handed rotation power is dominant. By using the defined modal power, the degree of deformation of the spatial pattern at each radial position can be evaluated by the deformation index ξ defined as follows,

$$\xi(r_n, M) = \frac{\sum_m p(r_n, m, M\omega) - p(r_n, M, M\omega)}{p(r_n, M)}, \tag{5.16}$$

where $p(r_n, M) = \sum_m p(r_n, m, M\omega)$. Figure 5.15(c) shows the radial profile of the contribution of non-harmonic modes to harmonic modes at each frequency obtained from Eq. (5.16). In all modes, it is shown that the pattern deformation is strongly observed at the plasma center. As observed in the analysis using the FBF expansion, the largest deformation is observed for the M = 3 frequency component. On the other hand, the degree of deformation for M = 1 and M = 2 is found to be reversed around r_n = 2.5 cm, which suggests that the spatial pattern of M = 2 harmonic modes is strongly deformed in the inner region, while the pattern deformation of M = 1 harmonic modes is stronger in the outer region. The degree of entire pattern deformation at each radial position is evaluated as follows,

$$\xi_{\mathrm{tot}}(r_n) = \frac{\sum_M \xi(r_n, M) p(r_n, M)}{\sum_M p(r_n, M)}. \tag{5.17}$$

As shown by the black line in Figure 5.16(c), it is revealed that the deformation is smaller in the outer region of the plasma than in the center.

The contribution of the change in polarization properties due to the emergence of the backward propagating mode, i.e., the linear polarization component, to the pattern deformation is evaluated for each radial position. By using the modal power $p_i(r_n, m, n\omega)$, the modal polarization parameter γ can be defined as,

$$\gamma(r_n, m, M > 0) = \frac{p_{\mathrm{Linear}}(r_n, m, M\omega)}{p_{\mathrm{Circular}}(r_n, m, M\omega) + p_{\mathrm{Linear}}(r_n, m, M\omega)}. \tag{5.18}$$

where $p_{\mathrm{Linear}}(r_n, m, M\omega) = 2\min(p_+, p_-)$ and $p_{\mathrm{Circular}}(r_n, m, M\omega) = p_+ + p_- - p_{\mathrm{Linear}}$. The linear polarization properties at r_n = 1.8 cm and r_n = 2.5 cm obtained from Eq. (5.18) are shown in Fig. 5.16(a, b), respectively. The Lissajous trajectories corresponding to each

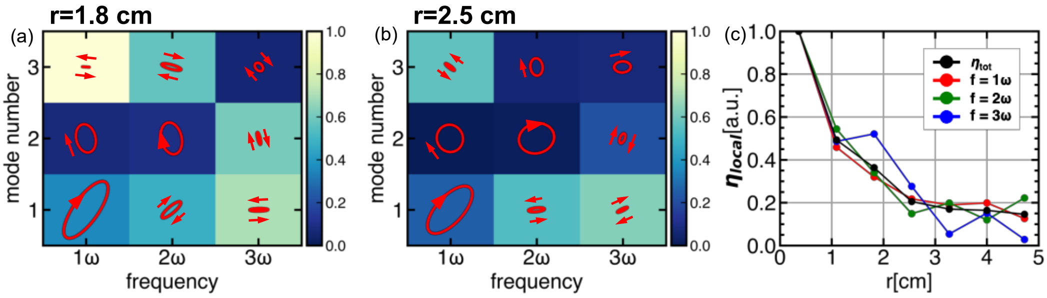

Fig. 5.16: (a, b) Modal power at $r = 1.8$ cm and $r = 2.5$ cm obtained using the FRF, and integrated modal power in terms of frequency (top). (c) The radial profile of the degree of deformation parameter ξ of each frequency. Black solid line represents the total deformation parameter ξ_{tot}.

mode are also inserted in each contour panel. Similar to the global analysis of spatial pattern, the ellopticalization of the Lissajous trajectories is more significant for the modes with larger linear polarization properties. Comparing the linear polarization properties at $r_n = 1.8$ cm and $r_n = 2.5$ cm, it is found that the linear polarization property for $r_n = 1.8$ cm is larger and the Lissajous trajectory for each mode is also deformed into more nearly linear elliptical shape. It is also confirmed that modes such as $\gamma(r_n, 1, 2)$ exist that have different rotation directions at different radial positions. Moreover, at each radial position, the index of the degree of linear polarization contamination, η, is defined as a function of frequency as follows,

$$\eta(r_n, M) = \frac{\sum_m p_{\pm}(r_n, m, M\omega)\gamma(r_n, m, M\omega)}{p(r_n, M)}. \tag{5.19}$$

where $p_{\pm}(m, M\omega) = p(r_n, m, -M\omega) + p(r_n, m, M\omega)$. Figure 5.17(c) shows the radial distribution of the degree of linear polarization contamination $\eta(r_n, M)$ in each of the frequency components evaluated by Eq. (5.19). For all M, $\eta(r_n, M)$ is smaller outside the plasma as well as the degree of pattern deformation, which indicates that the contribution of the backward propagating mode to the spatial pattern is smaller toward the outside of the plasma. It is also confirmed that the degree of linear polarization contamination increases at the local radial position, which is especially noticeable for the $M = 3$ mode. Moreover, the degree of linear polarization contamination in the entire pattern of the band at each radial position is shown by the black line in Figure 5.16(c) and is defined by the following equation.

$$\eta_{\mathrm{tot}}(r_n)=\frac{\sum_M \eta(r_n, M)p(r_n, M)}{\sum_M p(r_n, M)}. \tag{5.20}$$

This analysis suggests that the deformation of the pattern due to the backward propagating mode is more significant in the central region of the plasma.

5.5 Short Summary

In this chapter, it is described the results of an attempt to extract only deterministic patterns from probable oscillation patterns by performing a conditional average on solitary oscillations observed using tomography. Then, a new method was proposed to extract the deterministic trend by applying parameters that optimize the ensemble determination used for conditional averaging. The spatial pattern of the deterministic trend extracted using the conditional average method should not deform if a strictly rotationally symmetric plasma is assumed. However, it is found that the observed deterministic pattern deforms with time evolution and the symmetry is broken. Consequently, mode and frequency decompositions are performed to identify the causes of the pattern deformation using FBF and FRF analysis. As a result, the deformation of the spatial pattern in the deterministic trend is found to be caused by the mixing of modes of inverse rotation and modes with the same number of azimuthal modes but different frequencies (non-harmonic modes with different phase speed from the harmonics) from the original harmonics. Such spatial spectral broadening associated with the emergence of such backward propagating and non-harmonic modes could be explained by nonlinear coupling with the fluctuating modes ($\omega \neq 0$) the time-invariant stationary structure ($\omega = 0$). Focusing on the asymmetry in the background structure observed by tomographic measurements, it is shown by using a simple algebraic model that the emergence of all backward propagating and non-harmonic modes can be explained by the nonlinear coupling with harmonic modes. In the next chapter, the emergence process would be discussed using a simple nonlinear coupled model.

Chapter 6

Structure Formation by Non-linear Coupling of Background Asymmetry and Harmonic Modes

In a magnetic confinement plasma, various structures are formed by nonlinear interactions of microscopic fluctuations with structures at different scales, such as mesoscale and macroscale. Typical examples of such structures are streamers, which contribute to the deterioration of confinement performance, and zonal flows, which contribute to the improvement of confinement performance. In the nonlinear coupling process between fluctuating modes and stationary structures shown in this study, not only symmetry-breaking modes that deform the spatial pattern but also the emergence of symmetric structures with azimuthal mode number $m = 0$ have been observed. Consequently, it is necessary to decompose the non-harmonic modes generated by nonlinear coupling into symmetric structures ($m = 0$ modes) and symmetry-breaking structures ($m \neq 0$ modes) to understand the characteristics of each structure.

It was also mentioned in the previous chapter that the distortion of the spatial pattern present in the deterministic trend can be explained by considering the nonlinear coupling with background asymmetry and the harmonic modes to explain the formation of the structure contributing to the distortion. Generally, when considering nonlinear coupling, it is necessary to determine the degree of nonlinear coupling between the fluctuating modes. This is because it is unlikely that the coupling between each fluctuating mode is all in the same order. There should be some pairs of fluctuating modes that are easy to couple and some pairs that are hard to couple. Therefore, it is necessary to evaluate the degree of nonlinear coupling between the fluctuating modes and the stationary structure, even in nonlinear coupling of the kind considered in this study.

In this chapter, it is described the investigation of symmetric (m = 0 modes) and asymmetric ($m \neq 0$ modes) structures underlying the non-harmonic modes formed by nonlinear coupling of harmonic modes and background asymmetry, and the results of the evaluation of coupling coefficients.

6.1 Emergence Process of Pattern Deformation

The question in the previous chapter to arise is how there backward propagating and/or non-harmonic modes should emerge. Nonlinear coupling of the harmonics that compose the solitary oscillations should not give rise to modes with backward propagation or different phase velocities. The most possible explanations should be that these modes should be produced with nonlinear interaction of the original harmonic modes with the background asymmetry structure composed of stational non-zero azimuthal modes, i.e., $\omega = 0$. A nonlinear coupled model of background asymmetry and oscillating modes that can be expressed by a simple sinusoidal algebra can give a mathematical base to non-harmonic mode production and polarization modification due to such nonlinear interaction. Supposed that background asymmetry, $\bar{\varepsilon}_{\mathrm{A}}(m) \propto \cos(m\theta)$ and an original harmonic mode, $\tilde{\varepsilon}_{\mathrm{h}}(m') \propto \cos(m'\theta + m'\omega t)$, their couplings following a simple algebra should produce the non-harmonic modes as,

$$\bar{\varepsilon}_{\mathrm{A}}(m)\cdot\tilde{\varepsilon}_{\mathrm{h}}(m') \propto \cos(m\theta)\cos(m'\theta + m'\omega t)$$
$$= \cos\Big((m + m')\theta + m'\omega t\Big) + \cos\Big((m - m')\theta - m'\omega t\Big). \qquad (6.1)$$

The nonlinear coupling should produce two modes whose azimuthal mode numbers are

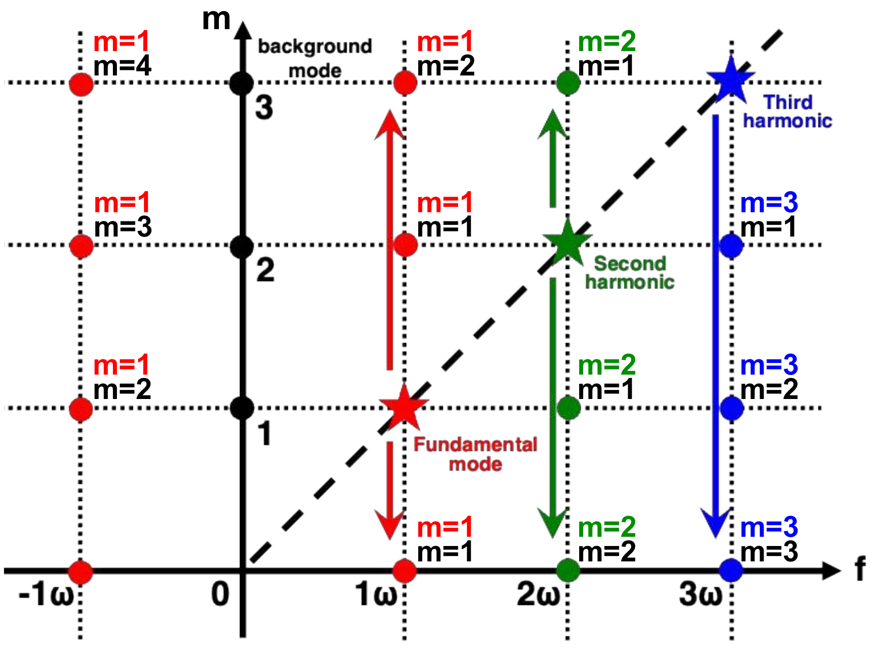

Fig. 6.1: Schematic of nonlinear coupling process between harmonic modes (star symbol) and background structure (black circle). Each color corresponds to a different frequency component of the harmonic mode.

$m + m'$ and $m - m'$. Moreover, if the integer, m, is larger than m', the mode of the second term propagates in the opposite direction to the original mode. For example, the dominant harmonic mode of m' = 1 should produce backward propagating mode through the couplings with the stationary m = 2 structure of the background. Similarly, all non-harmonic modes observed here can be produced through the nonlinear coupling between the original harmonic modes of 1ω, 2ω, 3ω..., indicated by star marks in Fig. 6.1 and the background asymmetry of the corresponding azimuthal mode numbers (black circle in Fig. 6.1). Note that the harmonic modes are assumed to be self-produced through their nonlinear couplings. The presented nonlinear coupling process between the stationary structure ($\omega = 0$) and the fluctuating modes ($\omega \neq 0$) should be a different kind of the ones between fluctuating modes, which have been conventionally discussed [131-133].

6.2 Evaluation of Nonlinear Coupling Constant

There have been studies to experimentally clarify the process of structure formation due to coupling between fluctuating modes. At this time, bicoherence analysis has often been used to evaluate the degree of nonlinear coupling between fluctuating modes. However, this method evaluates the degree of nonlinear coupling between fluctuating modes, and is not suitable for evaluating the degree of nonlinear coupling between fluctuating modes and stationary structure, as in this study. Therefore, we discuss the results of evaluating the formation of mode structures due to background asymmetry and nonlinear coupling of the basic structure by considering a simple nonlinear coupling model.

The process by which the non-harmonic modes are generated by the nonlinear coupling of the harmonic mode and the background asymmetry can be defined in a simplified model by considering the coupling coefficient $C_{m^{\mathrm{nh}}}$ as follows.

$$C_{m^{\mathrm{nh}}} \cdot \overline{A}_m \cos(m\theta) \cdot \widetilde{A}_m^{\mathrm{h}} \cos(m\theta + m\omega t)$$
$$= \widetilde{A}_m^{\mathrm{nh}} \left(\cos\left((m + m')\theta + m'\omega t\right) + \cos\left((m - m')\theta - m'\omega t\right) \right). \tag{6.2}$$

Where $\overline{A}_m$, $\widetilde{A}_m^{\mathrm{h}}$, $\widetilde{A}_m^{\mathrm{nh}}$, represent the background structure amplitude, harmonic mode amplitude, and non-harmonic mode amplitude respectively. The amplitudes of the harmonic and non-harmonic mode were calculated using the coefficients obtained in Eq. (5.9) and (5.15) in the previous chapter. Considering that the amplitudes of both sides in Eq. (6.2) are simply proportional to the coupling coefficient, the coupling coefficient $C_{m^{nh}}$ can be roughly defined as follows.

$$C_{m^{\mathrm{nh}}} = \frac{\widetilde{A}_m^{\mathrm{nh}}}{\overline{A}_m \widetilde{A}_m^{\mathrm{h}}} m'\omega. \tag{6.3}$$

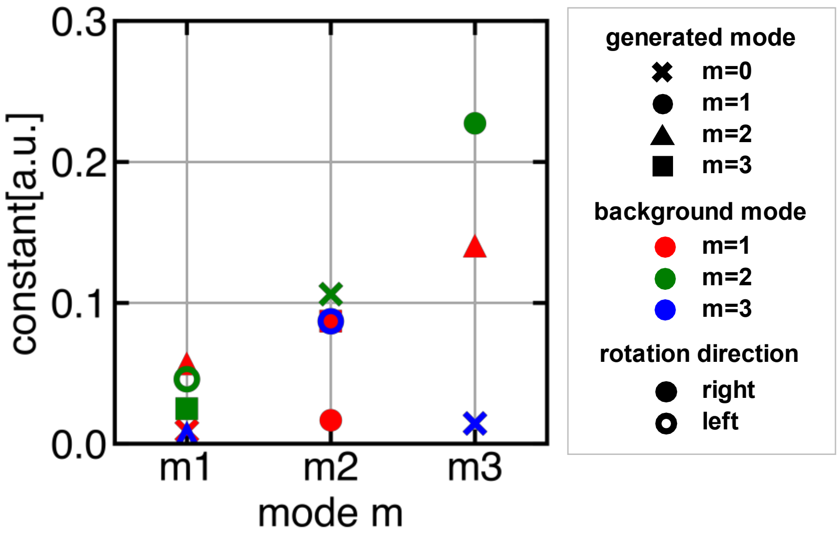

Fig. 6.2: Coupling coefficients in nonlinear coupling of the harmonic modes and the background structure. The color of each symbol represents the azimuthal mode numbers of the background structure, respectively. The shape of the symbol represents the generated non-harmonic modes, respectively. Furthermore, the filled and hollowed-out symbols represent the rotation direction of generated non-harmonic modes, respectively.

The reason for multiplying by $m'\omega$ in evaluating the coupling coefficient is discussed in the Appendix. The coupling coefficients estimated from the above are shown in Fig. 6.2. The vertical and horizontal axes represent the coupling coefficient values and $m = 1 \sim 3$ components of the harmonic modes, respectively. The color of each symbol, red, green, and blue, represents the azimuthal mode numbers $m = 1 \sim 3$ of the background structure, which is the counterpart of the nonlinear coupling with each component of the harmonic modes, respectively. The shape of the symbol represents the generated non-harmonic modes: cross, circle, triangle, and square represent the m = 0, 1, 2, and 3 modes, respectively. Furthermore, the filled and hollowed-out symbols represent the right- and left-handed rotating components of each mode structure, respectively. It can be confirmed that the magnitude of nonlinear coupling tends to be stronger for larger azimuthal mode numbers of the harmonic modes. It can also be seen that for the m = 1 and m = 2 components of the background structure, the relationship is almost constant fold for each azimuthal mode number of the harmonic modes. On the other hand, no specific relationship is found for the coupling coefficient with the m = 3 component of background structure. This difference can be attributed to the fact that the m = 1 and m = 2 components of the background structure have steep radial gradients, while the m = 3 component has a relatively flat radial gradient. Therefore, one would expect that the strength of the gradient of the background structure would be related to the magnitude of the coupling coefficient in the nonlinear coupling. Consequently, the coupling coefficients in the nonlinear coupling of the harmonic modes and background asymmetry are successfully estimated by considering the nonlinear coupling model.

6.3 Reconstruction of Harmonic and Non-Harmonic Modes Structure

Without background asymmetry, the solitary oscillations should consist only of simple harmonic components. The hypothesis makes it possible to reconstruct the original solitary oscillation composed of the original harmonic modes using Eq. (5.9) or (5.15). Consequently, the deterministic trend $\tilde{\varepsilon}_{\mathrm{d}}(r, \theta, t)$ obtained from the tomography can be separated as follows,

$$\tilde{\varepsilon}_{\mathrm{d}}(r, \theta, t) = \tilde{\varepsilon}_{\mathrm{h}}(r, \theta, t) + \tilde{\varepsilon}_{\mathrm{nh}}(r, \theta, t). \tag{6.4}$$

where $\tilde{\varepsilon}_{\mathrm{h}}(r, \theta, t)$ and $\tilde{\varepsilon}_{\mathrm{nh}}(r, \theta, t)$ represent harmonic and non-harmonic modes, respectively. The m = 0 and $m \neq 0$ modes inherent in the generated non-harmonic modes can also be reconstructed in the same way by using the coefficients shown in Eq. (5.9) or

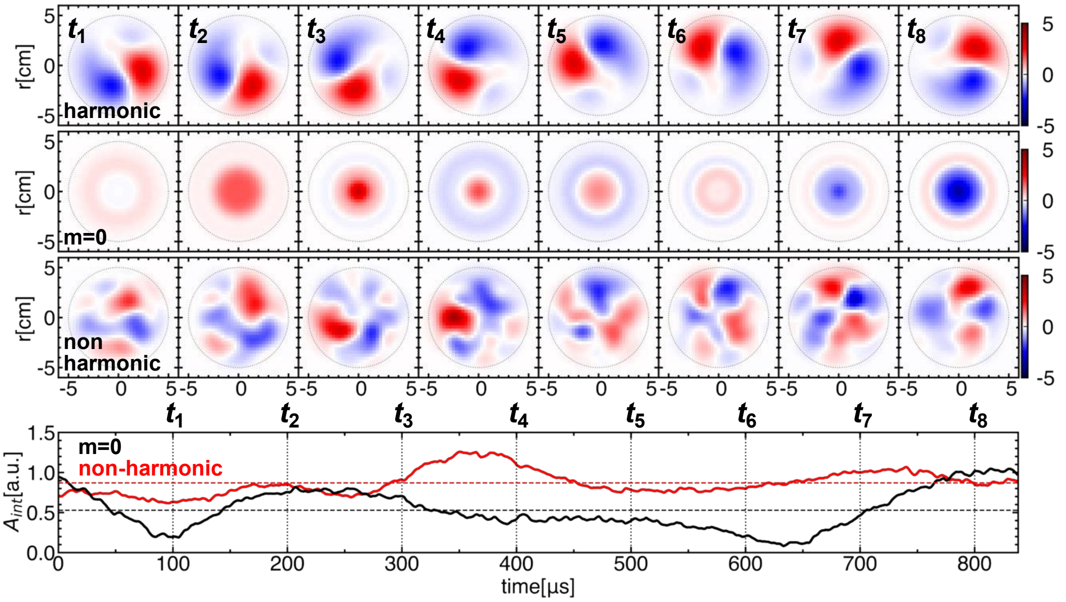

Fig. 6.3: (a) The temporal evolutions of 2D images of inferred original solitary oscillations, generated $m = 0$ mode (symmetric) part, and integrated (asymmetric) part of non-harmonic modes. (b) The temporal evolutions of the integrated amplitudes of symmetric and asymmetric part. The dashed lines show the temporal average of each part.

(5.15). Consequently, since $\tilde{\varepsilon}_{\mathrm{nh}}(r, \theta, t)$ also includes $m = 0$ modes, the non-harmonic modes can be separated into $m = 0$ modes and $m \neq 0$ modes, which can be expressed as follows,

$$\tilde{\varepsilon}_{\mathrm{nh}}(r, \theta, t) = \tilde{\varepsilon}_{m=0}(r, \theta, t) + \tilde{\varepsilon}_{m\neq 0}(r, \theta, t). \tag{6.5}$$

where $\tilde{\varepsilon}_{m=0}(r, \theta, t)$ and $\tilde{\varepsilon}_{m\neq 0}(r, \theta, t)$ represent $m = 0$ and $m \neq 0$ modes in non-harmonic modes, respectively. Thus, Eq. (6.4) can be rewritten as follows,

$$\tilde{\varepsilon}_{\mathrm{d}}(r, \theta, t) = \tilde{\varepsilon}_{\mathrm{h}}(r, \theta, t) + \tilde{\varepsilon}_{m=0}(r, \theta, t) + \tilde{\varepsilon}_{m\neq 0}(r, \theta, t). \tag{6.6}$$

From the respective reconstructed spatial structures shown in Fig. 6.3(a), it can be seen that the spatial pattern of the solitary oscillations is a distorted spatial pattern dominated by the $m = 1$ component, which rotates without distorting its shape. Since the amplitudes of the $m = 0$ and $m \neq 0$ modes shown in Fig. 6.3(b) are of the same order, the nonlinear coupling should not only deform the harmonic modes to make the oscillation pattern more turbulent, but also contribute to the symmetry restoration.

6.4 Behavior of Asymmetric ($m \neq 0$) Structure

It is mentioned that all the components in the non-harmonic modes ($m \neq 0$) affect the distortion of the spatial pattern of the deterministic trend. Thus, the amplitude of the distortion structure is modulated, as shown in Fig. 6.4(a-1). It can also be seen that the amplitude is strongly modulated not only in time but also in the radial direction. Therefore, the non-harmonic modes are decomposed by azimuthal mode number and frequency, and the radial and temporal evolution of each structure is investigated by using FRF.

First, the time evolution of the mode decomposed amplitude is discussed. From the radial distribution of the time evolution and time-averaged amplitude shown in Fig. 6.4(a-

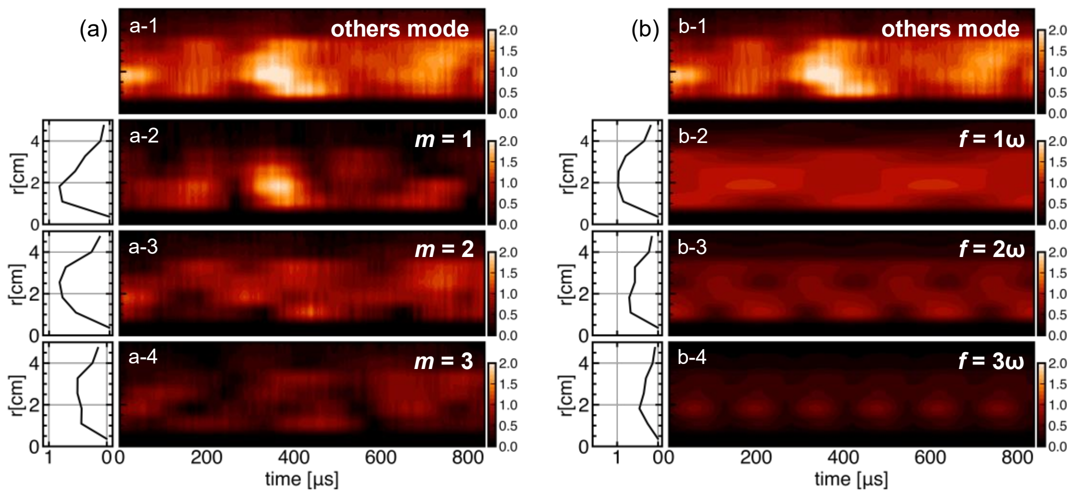

Fig. 6.4: Time evolution of the radial distribution of the amplitude of non-harmonic modes decomposed by (a) azimuthal mode number and (b) frequencies. The left side of each figure shows the radial distribution of time-averaged amplitudes.

2), the m = 1 component has a strong amplitude region inside $r \sim 2.0$ cm. It suggests that the m = 1 mode, which is caused by nonlinear coupling with background asymmetry, is concentrated in the inner radial direction. In addition, since the amplitude is modulated in a complex manner, it is possible that multiple modes are contaminated. On the other hand, the m = 2 mode shown in Fig. 6.4(a-3) exists in 1 cm < r < 4 cm with a strong amplitude range. This suggests that the nonlinear coupling that forms the m = 2 mode occurs outside the plasma rather than in the m = 1 mode. The m = 3 mode shown in Fig. 6.4(a-4) has about half the amplitude of the m = 1 and m = 2 modes. In addition, the amplitude is relatively constant at each radial position, suggesting that the nonlinear coupling that produces the m = 3 mode occurs in the entire plasma. On the other hand, the trend of temporal modulation of the amplitude is similar to the m = 2 mode. This suggests that the m = 3 non-harmonic mode is a high probability of being a mode generated by nonlinear coupling between the harmonic modes generating the m = 2 non-harmonic mode and the background asymmetry.

Next, time evolution of the frequency decomposed amplitude is discussed. The $f = 1\omega$ mode shown in Fig. 6.4(b-2) confirms that the strong amplitude region exists in 1 cm < r < 4 cm. This behavior is similar to the trend described for the m = 2 mode. Accordingly, the $f = 1\omega$ mode is expected to dominant by the m = 2 component. On the other hand, in the $f = 2\omega$ mode shown in Fig. 6.4(b-3), it can be seen that the strong amplitude region moves in time from the outer radial direction ($r \sim 3.0$ cm) toward the inner radial direction ($r \sim 1.0$ cm). The radial distribution of the time-averaged amplitude is relatively broad. This suggests the coexistence of the m = 1 component, which is dominant in the inner radial direction, and the m = 3 component, which is distributed in the entire plasma. The $f = 3\omega$ mode shown in Fig. 6.4(b-4), the strong amplitude region is localized at a local position ($r \sim 2.0$ cm). This is consistent with the trend for m = 1 mode. Accordingly, $f = 3\omega$ mode is considered to be dominated by $m = 1$ component.

As shown above, it is confirmed that the complex pattern deformation in the non-harmonic mode occurs not only in the azimuthal direction but also in the radial direction. Such changes suggest that since ArI emission is dependent on electron density and temperature, the electron density and temperature may vary non-uniformly in the radial direction. Currently, a method to evaluate density and temperature directly from tomography is under development, and further development is expected in the future.

6.5 Behavior of Symmetric (m = 0) Structure

Figure 6.5(a) shows the time evolution of the m = 0 mode variation at each radial position. The maximum variation is observed at the plasma center, while little variation is observed for $r > 2.5$ cm. The two-dimensional map of the time evolution of the variation for each radial position shows that there is a region of strong emission intensity from the plasma center to the outer radial direction but that the intensity decreases outside the

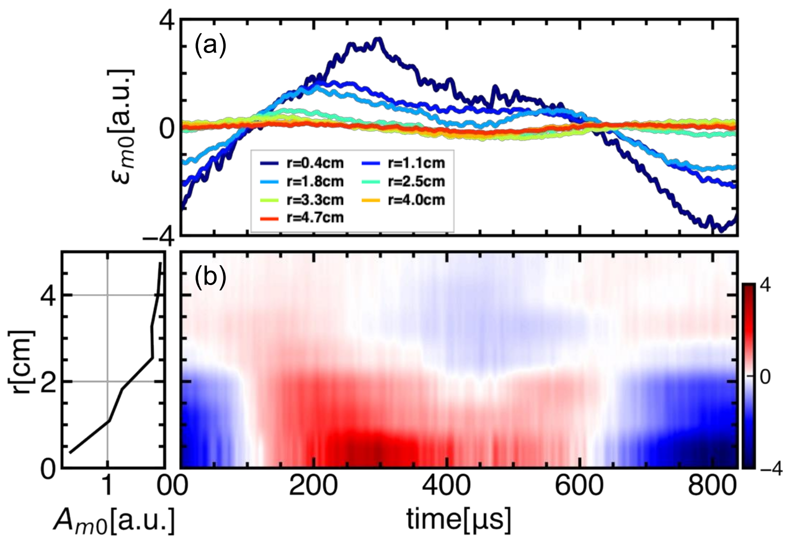

Fig. 6.5: (a) Time evolution of the m=0 mode fluctuation at each radial position. (b) Time evolution of radial profile of m = 0 mode fluctuation using FRF series. Time averages of the radial profile of amplitude are shown on the left.

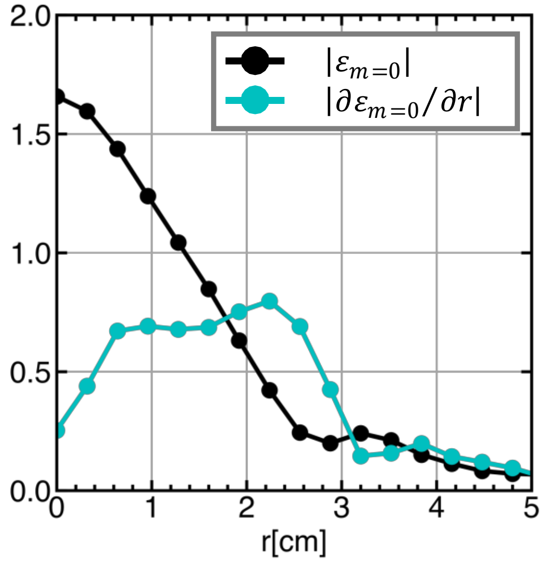

Fig. 6.6: Radial distribution of the time-averaged (a) amplitude of the m = 0 mode and (b) its first-order derivative.

radial direction at r > 2.5 cm, as shown in Fig. 6.5(b). This trend is also confirmed by the time-averaged radial distribution of the m = 0 mode shown on the left side of Fig. 6.5(b). To quantitatively understand the change in the radial emission distribution, the first-order derivative of the amplitude of the m = 0 mode in the radial direction is calculated. Figure 6.6 shows the results. From the first-order derivative shown blue line, it can be confirmed that the emission significantly decays in the region of r < 2.5 cm, and that the decay of the emission is gradual for r > 3.0 cm. If the emission is allowed to be proportional to the pressure of the plasma, the steep gradient could correspond to a shear creation in the diamagnetic velocity. It is possible that such shear creation could affect the instabilities [134-138]. Moreover, if such velocity shear exists, it can be expected to be accompanied by structures that affect the suppression of turbulence such as zonal flows. A resent simulation has suggested that nonlinearity interaction between the background density asymmetry caused by inhomogeneous particle sources and the drift wave can enhance zonal flows, which may be consistent with the present observation [139]. The present scenario leads to a hypothesis that steady state asymmetries in magnetically confined plasma, which could be induced by auxiliary heating, may enhance turbulence and/or zonal flows to change the confinement properties.

Chapter 7

Conclusion

To maintain steady-state high performance plasmas, it is important to resolve the effects of turbulence structure formation, symmetry breaking, and asymmetry in the plasma distribution, which affect confinement performance. However, these phenomena are known to be caused by nonlinear interactions of oscillations at disparate scales and/or to affect the entire plasma from the local to the global scale, requiring global measurements to understand the phenomena. In many torus devices, imaging measurements such as ECE measurements, BES, and GPI are used, but they are limited to localized regions of the plasma cross-section. Therefore, the development of a global measurement system that covers the entire plasma cross-section and a method for analyzing the data are required to further progress our understanding of the phenomena. In this study, solitary oscillations were observed using a tomography system that can measure the entire plasma cross-section in the linearly magnetized plasma device PANTA, and nonlinear effects of asymmetry in the background profile on solitary oscillations were investigated. The following is a summary of the results of this study.

The emission distribution observed by the tomography system can be separated into a background structure, which is a time-averaged component, and a fluctuation structure. Mode decomposition of the background structure using the Fourier-Bessel series expansion confirms the presence of an asymmetric component with an intensity of about 20%. Since the fluctuation structure of solitary oscillations is also quasi-periodic but probable, we have attempted to extract the deterministic trend by using the conditional average method. A new method, CECAME, is proposed to optimize the ensemble by using the uncertainty and statistical properties of the deterministic part, which is a tradeoff relationship, to determine the threshold value for the correlation, which was arbitrary in the Template method. In CECAME, the threshold value that minimizes the optimization parameter is the correlation value that optimizes the ensemble and at the same time coincides with the value that minimizes the mean value error of the deterministic trend. Therefore, it is possible to optimize the determination of the ensemble and extract the most probable deterministic trend by using CECAME. The proposed method should be applicable to short-lived phenomena such as blob and streamers, as well as the quasi-oscillatory phenomena. Also, CECAME is applied to the tomography data to extract the spatial structure of the deterministic trend of the solitary oscillations, which confirms that the spatial pattern is deformed. The ArI emission observed by tomography measurements can be modeled by electron density and temperature as shown in Chapter 3. Therefore, it is conceivable that if the pattern is deformed, transport may also be changed. Since it is difficult to discuss the transport only by tomography measurements, it is necessary to simultaneously measure physical quantities using electrostatic probes and other methods to clarify the relationship with the transport.

Since the deterministic trend extracted by ensemble averaging removes the probability of waveforms, the deformation of the deterministic pattern should not occur if the phenomenon is in an axisymmetric plasma system. Then, to investigate the causes of pattern deformation, the deterministic pattern is decomposed into structures by the azimuthal mode number using FBF and FRF expansions, and the deformation of the pattern for each mode structure is investigated. In addition, the pattern deformation of each mode structure is quantitatively shown by representing the pattern deformation as a vector using moment vectors. It is suggested that each mode structure contains not only harmonic modes consisting of fundamental and its harmonics but also backward propagating and non-harmonic modes whose phase speed is different from that of harmonic modes, resulting in pattern deformation. To quantify the effect of backward propagating and non-harmonic modes on pattern deformation, the rotation coefficients of right- and left-handed are evaluated for each azimuthal mode number and frequency by performing Fourier transform on the moment vectors. The results revealed the existence of non-harmonic modes with significant power in addition to harmonic modes, as well as the existence of significant backward propagating modes. It is also shown that there are non-harmonic modes with an intensity of about 50% with respect to the deterministic pattern. In addition, by defining polarization using rotation coefficients evaluated from moment vectors, it is possible to quantitatively evaluate the effect of only the backward propagating mode on pattern deformation. This is because polarization is defined as the superposition of vectors, and the superposition of vectors with different rotation directions produces a linear polarization component. Then, the effect of the backward propagating mode was quantified by evaluating the degree of contamination of the linear polarization component in each mode. As a result, it was successfully quantified that the influence of the backward propagating mode in the deterministic trend of the pattern is about 15% of the total pattern. From the above, it is shown that the backward propagating and non-harmonic modes deform the spatial pattern and make it turbulent. In general, the space spectral broadening can be explained by parametric instabilities, which should lead the plasma to a turbulent state. Here, the background structure observed in this study also has an asymmetric distribution and meaningful mode structure. The existence of nonlinear interaction between such time-invariant modes and coherent modes should also be considered. Therefore, it is important to investigate the nonlinear interaction between the steady asymmetric distribution and the fluctuating modes as a new possibility to lead the plasma to a turbulent state.

In Chapter 6, it was shown that a simple sinusoidal algebra can give a mathematical base to the generation of backward propagating and non-harmonic mode due to such nonlinear interaction. Such a nonlinear coupling process is a coupling between fluctuating modes and structure, which is different from the coupling conventionally considered, and was discovered by performing global measurements that can observe the entire plasma cross-section, such as tomography measurements. Although it is general to evaluate the degree of nonlinear coupling by bicoherence analysis, it is difficult to use this method for nonlinear coupling between fluctuating modes and structures. Therefore, a simplified coupling coefficient was also evaluated by using a nonlinear coupling model. This suggested that the gradient of the background structure may affect the coupling coefficient. Furthermore, as the nonlinear coupling model indicates, non-harmonic modes form not only the asymmetric component ($m \neq 0$) which contributes to the deformation of the pattern, but also the symmetric component ($m = 0$). Focusing on the structure of the symmetric component, it is confirmed that a steep gradient change occurs in the radial direction. If the emission is proportional to the plasma pressure, the steep gradient may correspond to the formation of a diamagnetic velocity shear. Such shear creation should affect the instability. Simulation studies have also shown that zonal flows are enhanced by the nonlinear interaction between the asymmetry of the density profile and the drift wave. These results suggest that distribution asymmetry in magnetic confinement plasmas, which may be caused by auxiliary heating, may change the confinement properties by enhancing turbulence and zonal flows.

Finally, the measurements and analyses on the plasma images obtained with the tomography show that the nonlinear effects of background asymmetry, its nonlinear coupling with the harmonic modes, should produce the non-harmonic modes that deform the original pattern of the solitary oscillation with breaking the rotational symmetry. Therefore, the results suggest an unfeatured route for plasma to change into turbulence state, as well as the excellent capability of the tomography to explore a research frontier for magnetized plasmas.

Acknowledgement

It is a great pleasure to thank many people who gave me great guidance and encouragement during my three years of research in the doctoral course.

First of all, I deeply thankful to my supervisor, Professor A. Fujisawa. He gave me continuous advice and provided an ideal environment for conducting my research. Also, I could participate in research using advanced measurement systems, and received helpful guidance on data processing and analysis methods. In addition, I had the valuable experience of start-up of the Tokamak device. I would like to express my special thanks to Associate professor Y. Nagashima, Associate Professor C. Moon, and Assistant Professor T. Nishizawa for their useful discussion and advice. I would like to express my gratitude to Assistant Professor K. Yamasaki (Univ. Hiroshima) for the excellent advice about my data analysis. I could never have completed my thesis without his help.

This work was partly supported by JST SPRING, Grant Number JPMJSP2136 and JSPS KAKENHI Grant Numbers JP17H06089, 20K14443, JP21K13898, JP22H00120, and JP23KJ1702.

Furthermore, I wish to thank Professor S. Inagaki (Univ. Kyoto), Professor T. Ido, Professor T. Yamada, Professor N. Kasuya, and Associate Professor Y. Kosuga for useful discussions on research and support of research life.

I would like to express my appreciation to my research group students, especially for Mr. D. Nishimura, Mr. S. Mochinaga, Mr. Y. Nishimura, T. Suetsugu, and Mr. I. Oyama. Thanks to their kind support, I have enjoyed my campus life. I would also like to thank Ms. H. Sugitani, Ms. Y. Hieida, and Ms. M. Funaki for their assistance with the administrative procedures of research life. Finally, I would like to special thank my family for their support throughout my research life.

Bibliography

[1] https://www.un.org/

[2] https://www.iter.org/

[3] F. Romanelli *et al*., Nucl. Fusion **51**, 094008 (2011).

[4] H. Kishimoto *et al*., J. Nucl. Mater. **145-147**, 41 (1987).

[5] C. M. Muscatello *et al*., Rev. Sci. Instrum. 90, 073504 (2019).

[6] R. Hemsworth *et al*., Nucl. Fusion **49**, 045006 (2009).

[7] M. J. Mantsinen *et al*., Phys. Rev. Lett. **88**, 105002 (2002).

[8] V Erckmann and U Gasparino., Plasma Phys. Control. Fusion 36, 1869 (1994).

[9] P. H. Diamond *et al*., Plasma Phys. Control. Fusion **47**, R35 (2005).

[10] A. Fujisawa *et al*., Nucl. Fusion **49**, 013001 (2009).

[11] C. Holland *et al*., Phys. Rev. Lett. **96**, 195002 (2006).

[12] A. D. Liu *et al*., Phys. Rev. Lett. **103**, 095002 (2009).

[13] T. Yamada *et al*., Nature. Phys. **4**, 721 (2008).

[14] N. Kasuya *et al*., Phys. Plasmas **15**, 052302 (2008).

[15] Y. Kosuga and K. Hasamada, Phys. Plasmas **25**, 100701 (2018).

[16] T. Kobayashi *et al*., Phys. Rev. Lett. **120**, 045002 (2018).

[17] S. Inagaki *et al*., Phys. Rev. Lett. **107**, 115001 (2011).

[18] S. Maeyama *et al*., Phys. Rev. Lett. **114**, 255002 (2015).

[19] Y. Kaspi *et al*., Nature **555**, 223 (2018).

[20] M. Sasaki *et al*., Plasma Fusion Res. **14**, 1401161 (2019).

[21] L. Chen, Z. Lin, and R. White, Phys. Plasmas **7**, 3129 (2000).

[22] T.-H. Watanabe, H. Sugama, and S. Ferrando-Margalet, Phys. Rev. Lett. **100**, 195002 (2008).

[23] A. Fujisawa *et al*., Phys. Rev. Lett. **79**, 1054 (1997).

[24] A. Fujisawa *et al*., Phys. Rev. Lett. **93**, 165002 (2004).

[25] Y. Nagashima *et al*., Phys. Plasmas **16**, 020706 (2009).

[26] M. Sasaki *et al*., Nucl. Fusion **52**, 023009 (2012).

[27] Y. Camenen *et al*., Phys. Rev. Lett. **102**, 125001 (2009).

[28] K. Itoh, K. Hallatschek, and S.-I. Itoh, Plasma Phys. Control. Fusion **47,** 451(2005).

[29] F. L. Waelbloaeck and L. Chen, Phys. Fluids B **3**, 601 (1991)

[30] C. Watts *et al*., Phys. Rev. Lett. **76**, 2274 (1996).

[31] G. Birkenmeier *et al*., Phys. Rev. Lett. **107**, 025001 (2011).

[32] M. F. J. Fox *et al*., Plasma Phys. Control. Fusion **59,** 034002 (2017).

[33] Y. Xu *et al*., Nucl. Fusion **53**, 072001 (2013).

[34] A. Fujisawa *et al*., Nucl. Fusion **36**, 375 (1996).

[35] Y. Camenen *et al*., Phys. Rev. Lett. **105**, 135003 (2010).

[36] K. Ida *et al*., Sci. Rep. **6**, 36217 (2016).

[37] H. Chen *et al*., Phys. Plasmas **7**, 4567 (2000).

[38] T. Odstrcil *et al*., Plasma Phys. Control. Fusion **60,** 014003 (2018).

[39] C. Angioni and P. Helander, Plasma Phys. Control. Fusion **56,** 124001 (2014).

[40] A. Y. Aydemir, Phys. Plasmas **25**, 050702 (2018).

[41] P. Donnel *et al*., Plasma Phys. Control. Fusion **61,** 014003 (2019).

[42] T. Fulop and P. Helander, Phys. Plasmas **8**, 3305 (2001).

[43] H. K. Park *et al*., Phys. Rev. Lett. **96**, 195003 (2006).

[44] G. S. Yun *et al*., Phys. Rev. Lett. **107**, 045004 (2011).

[45] J. E. Lee *et al*., Sci. Rep. **7**, 45075 (2017).

[46] Y. C. Li *et al*., Sci. Rep. **13**, 4785 (2023).

[47] I. Shesterikov *et al*., Phys. Rev. Lett. **111**, 055006 (2013).

[48] W. Han *et al*., Sci. Rep. **12**, 18142 (2022).

[49] K. L. Wong *et al*., Phys. Rev. Lett. **66**, 1874 (1991).

[50] G. R. McKee *et al*., Rev. Sci. Instrum. **77**, 10F104 (2006).

[51] K. Ida *et al*., Phys. Rev. Lett. **120**, 245001 (2018).

[52] D. K. Gupta *et al*., Phys. Rev. Lett. **97**, 125002 (2006).

[53] D. Iraji, I. Furno, and C. Theiler, Phys. Plasmas **17**, 122304 (2010).

[54] G.Y. Antar, J. H. Yu, and G. Tynan, Phys. Plasmas **14**, 022301 (2007).

[55] S. Oldenburger *et al*., Plasma Phys. Control. Fusion **54**, 055002 (2012).

[56] M. J. Burin *et al*., Phys. Plasmas **12**, 052320 (2005).

[57] P. Manz *et al*., Phys. Rev. Lett. **107**, 195004 (2011).

[58] T. Windisch, O. Grilke, and T. Klinger, Phys. Plasmas **13**, 122303 (2006).

[59] F. Brochard *et al*., Phys. Plasmas **13**, 052509 (2006).

[60] T. Yamada *et al*., Phys. Rev. Lett. **105**, 225002 (2010).

[61] H. Arakawa. *et al*., Plasma Phys. Control. Fusion **52**, 105009 (2010)

[62] T. Kaneko, H. Tsunoyama, and R. Hatakeyama, Phys. Rev. Lett. **90**, 125001(2003).

[63] C. Moon, T. Kaneko, and R. Hatakeyama, Phys. Rev. Lett. **111**, 115001(2013).

[64] S. Inagaki *et al*., Sci. Rep. **6**, 22189 (2016).

[65] T. Kobayashi *et al*., Plasma Fusion Res. **12**, 1401019 (2017).

[66] T. Kobayashi *et al*., Phys. Plasmas **23**, 102311 (2016).

[67] F. Kin *et al*., Phys. Plasmas **26**, 042306 (2019).

[68] Y. Kawachi *et al*., Plasma Phys. Control. Fusion **62**, 055011 (2020).

[69] N. Ohyama *et al*., Plasma Fusion Res. **7**, 1201025 (2012).

[70] B. Zhang *et al*., Plasma Phys. Control. Fusion **61**, 115010 (2019).

[71] H. M. Mott-Smith *et al*., Phys. Rev. 28, 727 (1926).

[72] S. Oldenburger *et al*., Plasma Fusion Res. **7**, 2401146 (2012).

[73] J. Adamek *et al*., Czech. J. Phys. **55**, 235 (2005).

[74] G. Bousselin *et al*., Rev. Sci. Instrum. **84**, 013505 (2013).

[75] G. Grenfell *et al*., Rev. Sci. Instrum. **93**, 023507 (2022).

[76] Y. Nagashima *et al*., J. Plasma Fusion Res. SERIES, **8**, 50(2009).

[77] T. Yamada *et al*., Rev. Sci. Instrum. **78**, 123501 (2007).

[78] K. Hasamada *et al*., Plasma Fusion Res. **12**, 1201034 (2017).

[79] Y. Kawachi *et al*., Sci. Rep. **12**, 19799 (2022).

[80] T. Ido *et al*., Plasma Phys. Control. Fusion **48**, S41 (2006).

[81] G. D. Conway *et al*., Plasma Phys. Control. Fusion **46**, 951 (2004).

[82] H. Tanaka, N. Ohno, Y. Tsuji and S. Kajita, Contrib. Plasma Phys. **50**, 256 (2010).

[83] S. Oldenburger, F. Brochard and G. Bonhomme, Phys. Plasmas **18**, 032307 (2011).

[84] S. Ohdachi *et al*., J. Phys.: Conf. Ser. **823**, 012009 (2017).

[85] C. Brandt *et al*., Plasma Phys. Control. Fusion **62**, 035010 (2020).

[86] K. F. Mast *et al*., Rev. Sci. Instrum. **56**, 969 (1985).

[87] D. R. Ferreira *et al*., Fusion Eng. Des. **164**, 112179 (2021).

[88] B. J. Peterson *et al*., Rev. Sci. Instrum. **72**, 923 (2001).

[89] B. J. Peterson *et al*., Fusion Sci. Technol. **58**, 412 (2010).

[90] V. Gonzalez-Fernandez *et al*., Sci. Rep. **10**, 5389 (2020).

[91] A. D. Light, S. Chakraborthy Thakur, and G. R. Tynan Phys. Plasmas **26**, 023502 (2019).

[92] A. Fujisawa *et al*., Plasma Phys. Control. Fusion **58**, 025005 (2016).

[93] K. Yamasaki *et al*., Rev. Sci. Instrum. **91**, 033502 (2020).

[94] Y. Nagashima *et al*., J. Phys. Soc. Jpn. **89**, 039501 (2020).

[95] Y. Nagashima *et al*., J. Phys. Soc. Jpn. **92**, 033501 (2023).

[96] W. Lotz, Z. Phys. **216**, 241 (1968).

[97] M. J. Seaton, Mon. Not. R. Astron. Soc. **119**, 81 (1959).

[98] A. M. Cormack J. Appl. Phys. 35, 2908 (1964).

[99] G. M. Ramachandran and A. V. Lakshminarayanan, Proc. Natl Acad. Sci. **68** 2236 (1971).

[100] A. H. Andersen and A. C. Kak, Ultrasonic Imaging **6**, 81 (1984)

[101] C. Nardone, Plasma Phys. Control. Fusion **34**, 1447 (1992).

[102] S. Ohdachi *et al*., Plasma Sci. Technol. **8**, 45 (2005).

[103] L. A. Shepp and Y. Vardi, IEEE Trans. Med. Imaging **1**, 113 (1982).

[104] Y. Nagayama, J. Appl. Phys. **62**, 2702 (1987).

[105] Y. Nagayama, S. Tsuji, and K. Kawahata Phys. Rev. Lett. **61**, 1839 (1988).

[106] K. Yamasaki *et al*., Rev. Sci. Instrum. **88**, 093507 (2017).

[107] Y. Nishimura *et al*., Plasma Fusion Res. (2024), in press.

[108] K. Yamasaki *et al*., J. Appl. Phys. **126**, 043304 (2019).

[109] T-K. Kobayashi *et al*., Plasma Fusion Res. **16**, 1201082 (2021).

[110] S. Berujon *et al*., Phys. Rev. Lett. **108**, 158102 (2012).

[111] D. Nishimura *et al*., J. Appl. Phys. 129, 093301 (2021).

[112] I. Furno *et al*., Phys. Rev. Lett. **100**, 055004 (2008).

[113] T. P. Goodman *et al*., Phys. Rev. Lett. **106**, 245002 (2011).

[114] Y. Nagayama *et al*., Phys. Plasmas **3**, 1647 (1996).

[115] K. McGuire *et al*., Phys. Rev. Lett. **50**, 891 (1983).

[116] P. B. Snyder *et al*., Nucl. Fusion **47**, 961 (2007).

[117] A. Loarte *et al*., Plasma Phys. Control. Fusion **45**, 1549 (2003).

[118] G. R. McKee *et al*., Nucl. Fusion 53, 113011 (2013).

[119] H. Johnsen, H. Pecseli, and J. Trulsen, Phys. Fluids **30**, 2239 (1987).

[120] O. Grulke *et al*., Phys. Plasmas **8**, 5171 (2001).

[121] T. Carter *et al*., Phys. Plasmas **13**, 010701 (2006).

[122] A. Fujisawa, Plasam Fusion Res. **5**, 046 (2010).

[123] S. Inagaki *et al*., Plasam Fusion Res. **9**, 1201016 (2014).

[124] F. Kin *et al*., Plasam Fusion Res. **14**, 1402114 (2019).

[125] T-K. Kobayashi *et al*., Plasma Phys. Control. Fusion **63**, 032001 (2021).

[126] H. Arakawa *et al*., Plasma Phys. Control. Fusion **51**, 085001 (2009).

[127] H. Arakawa *et al*., Plasma Phys. Control. Fusion **53**, 115009 (2011).

[128] H. Arakawa *et al*., Sci. Rep. **6**, 33371 (2016).

[129] H. Arakawa *et al*., Phys. Plasmas **26**, 052305 (2019).

[130] M. Sasaki *et al*., Phys. Plasmas **22**, 032315 (2015).

[131] C. Hidalgo *et al*., Phys. Rev. Lett. **71**, 3127 (1993).

[132] G. R. Tynan *et al*., Phys. Plasmas **8**, 2691 (2001).

[133] Y. Nagashima *et al*., Rev. Sci. Instrum. **77**, 045110 (2006).

[134] H. Biglari, P. H. Diamond, and P. W. Terry, Phys. Fluids B **2**, 1 (1990).

[135] K. Itoh *et al*., Plasma Phys. Control. Fusion **36**, 123 (1994).

[136] T. S. Harm and K. H. Burrel, Phys. Plasmas **2**, 1648 (1995).

[137] R. R. Weynants *et al*., Nucl. Fusion **32**, 837 (1992).

[138] P. Manz, M. Ramisch, and U. Stroth, Phys. Rev. Lett. **103**, 165004 (2009).

[139] M. Sasaki *et al*., Phys. Plasmas **30**, 082302 (2023).

Appendix

Detailed nonlinear coupling model

Consider the nonlinear coupling process between the background asymmetry and harmonic modes in a little more detail. In Chapter 6, the nonlinear coupling model used to evaluate the coupling coefficients was a simple one that could be expressed in sinusoidal algebra. In this chapter, the formation of non-harmonic modes due to nonlinear coupling between the background asymmetry and harmonic modes is defined as follows,

$$\frac{\partial \tilde{\varepsilon}}{\partial t} = \gamma\tilde{\varepsilon} + \int G\left(r - r', \theta - \theta'\right)\tilde{\varepsilon}^{\mathrm{h}}\left(r', \theta', t\right) r'dr'd\theta'. \tag{A.1}$$

where γ represents the rate of mode growth and decay, and $G(r, \theta)$ is the coupling function of the modes (non-harmonic modes) formed by the effects from the asymmetry of the background structure. The function $\tilde{\varepsilon}$ of the oscillations as shown in Eq. (A.1) is defined as follows.

$$\tilde{\varepsilon}(r, \theta, t) = \sum_m \sum_n \tilde{\varepsilon}_{m,n}(r, t)e^{i(m\theta + n\omega t)}. \tag{A.2}$$

Thus, equation (A.1) can be rewritten as following equation.

$$\sum_m \sum_n \left[\frac{\partial \tilde{\varepsilon}_{m,n}(r; t)}{\partial t} + in\omega\tilde{\varepsilon}_{m,n}(r, t)\right] e^{i(m\theta + n\omega t)} = \sum_m \sum_n \gamma_{m,n}\tilde{\varepsilon}_{m,n}(r; t)e^{i(m\theta + n\omega t)}$$
$$+ \int G\left(r - r', \theta - \theta'\right) \sum_m \tilde{\varepsilon}^{\mathrm{h}}_m(r')e^{i(m\theta + m\omega t)}\, r'dr'd\theta' \tag{A.3}$$

Assuming that the change in $\tilde{\varepsilon}_{m,n}(r, t)$ is slow and that $\gamma_{m,n} \ll in\omega$ holds, equation (A.3) can be defined as follows.

$$\sum_m \sum_n in\omega\tilde{\varepsilon}_{m,n}(r, t)e^{i(m\theta + n\omega t)}$$

$$\approx \int G(r - r', \theta - \theta') \sum_{m} \tilde{\varepsilon}_m^{\mathrm{h}}(r') e^{i(m\theta + m\omega t)} r' dr' d\theta'. \tag{A.4}$$

Assuming that the coupling function $G(r, \theta)$ is a function that depends on the asymmetric component of the background structure and acts locally, it can be defined as follows.

$$G(r - r', \theta - \theta') = \left(\sum_{M} \hat{I}(\Delta\varepsilon_M(r)) e^{iM\theta} \right) \delta(r - r', \theta - \theta'). \tag{A.5}$$

where $\hat{I}$ represents the operator that takes into account the gradient of the background structure. Substituting equation (A.5) into equation (A.4), we can transform it as follows.

$$\sum_{m_{\mathrm{nh}}} \sum_{n} in\omega \tilde{\varepsilon}_{m_{\mathrm{nh}},n}(r) e^{i(m_{\mathrm{nh}}\theta + n\omega t)}$$
$$\approx \sum_{m_{\mathrm{h}}} e^{im_{\mathrm{h}}\omega t} \sum_{M} \hat{I}(\Delta\varepsilon_M(r)) \tilde{\varepsilon}_{m_{\mathrm{h}}}^{\mathrm{h}}(r') e^{i(M + m_{\mathrm{h}})\theta} r. \tag{A.6}$$

Here, m_{nh} and m_{h} represent the azimuthal mode number of the non-harmonic modes and the harmonic modes, respectively. If the coefficient to be compared is $|n| = m_{\mathrm{h}}$ because it has the same frequency component as the harmonic modes, the local relationship between the non-harmonic modes and harmonic modes can be expressed as follows.

$$\begin{aligned} \tilde{\varepsilon}_{m_{\mathrm{nh}},n}(r) &\approx \frac{\hat{I}\left(\Delta\varepsilon_{m_{\mathrm{nh}}-n}(r)\right) \tilde{\varepsilon}_n^{\mathrm{h}}(r)}{\mathrm{in\omega}} \\ &= -i \frac{\hat{I}\left(\Delta\varepsilon_{m_{\mathrm{nh}}-n}(r)\right) \tilde{\varepsilon}_n^{\mathrm{h}}(r)}{n\omega}. \end{aligned} \tag{A.7}$$

Where $\tilde{\varepsilon}_{m_{\mathrm{nh}},n}$ and $\tilde{\varepsilon}_n^{\mathrm{h}}$ are the amplitudes of the non-harmonic modes at $(m, f) = (m_{\mathrm{nh}}, n\omega)$ and the amplitude of the harmonic modes at $(m, f) = (|n|, |n|\omega)$, respectively. On the other hand, the global relationship can be obtained from Eq. (A.7) and expressed as follows.

$$\int \tilde{\varepsilon}_{m_{\mathrm{nh}},n}(r)rdr \approx -i\frac{1}{n\omega}\int \hat{I}\left(\Delta\varepsilon_{m_c\text{-}n}(r)\right)\tilde{\varepsilon}_n^{\mathrm{h}}(r)rdr$$

$$= -i\frac{1}{n\omega}\left(\frac{\int \hat{I}\left(\Delta\varepsilon_{m_{\mathrm{nh}}\text{-}n}(r)\right)\tilde{\varepsilon}_n^{\mathrm{h}}(r)rdr}{\int \hat{I}\left(\Delta\varepsilon_{m_{\mathrm{nh}}\text{-}n}(r)\right)rdr\int \tilde{\varepsilon}_n^{\mathrm{h}}(r)rdr}\right)\int \hat{I}\left(\Delta\varepsilon_{m_{\mathrm{nh}}\text{-}n}(r)\right)rdr\int \tilde{\varepsilon}_n^{\mathrm{h}}(r)rdr$$

$$= -i\frac{C_{m_{\mathrm{nh}},n}}{n\omega}\int \hat{I}\left(\Delta\varepsilon_{m_{\mathrm{nh}}\text{-}n}(r)\right)rdr\int \tilde{\varepsilon}_n^{\mathrm{h}}(r)rdr. \qquad \text{(A.8)}$$

By taking the absolute values of both sides, the coupling coefficient $C_{m_{\mathrm{nh}},n}$ between the background asymmetry and the harmonic modes can be defined as follows.

$$C_{m_{\mathrm{nh}},n} = \frac{\left|\int \tilde{\varepsilon}_{m_{\mathrm{nh}},n}(r)rdr\right|}{\left|\int \hat{I}\left(\Delta\varepsilon_{m_{\mathrm{nh}}\text{-}n}(r)\right)rdr\right|\left|\int \tilde{\varepsilon}_n^{\mathrm{h}}(r)rdr\right|}n\omega. \qquad \text{(A.9)}$$

Here, in estimating the coupling coefficients for the background asymmetry and harmonic modes in this study, $\tilde{\varepsilon}_{m_{\mathrm{nh}},n}(r)$ and $\tilde{\varepsilon}_n^{\mathrm{h}}(r)$ are the amplitudes of each structure calculated using the moment vector elements obtained in equations (5.9) and (5.15) in the previous chapter, respectively. Also, $\hat{I}\left(\Delta\varepsilon_{m_{\mathrm{nh}}\text{-}n}(r)\right)$ is the amplitude of the background structure for simplicity in this study. Since $n\omega$ is multiplied on the right-hand side of equation (A.9) to evaluate the coupling coefficient, it is reasonable to multiply $m'\omega$ in the evaluation of coupling coefficient in Chapter 6.